Microoptical Artificial Compound Eyes

Dissertation

zur Erlangung des akademischen Grades
doctor rerum naturalium (Dr. rer. nat.)

seit 1558

vorgelegt dem Rat der
Physikalisch-Astronomischen Fakultät
der Friedrich-Schiller-Universität Jena

von

Diplomphysiker Jacques Duparré
geboren am 23. März 1977 in Zwickau

Contents

1 Introduction

Natural vision, in particular natural compound eyes, have always fascinated mankind [1]. Compound eyes combine small eye volumes with a large field of view, at the cost of comparatively low spatial resolution. For small invertebrates as for instance flies or moths the compound eyes are the perfectly adapted solution to obtain sufficient visual information about their environment without overloading their brain with the necessary image processing [2]. The compound eye design is highly specialized for the natural living habitat, ambient illumination, required sensing tasks and available processing time, eye size and energy for processing.

However, up to date little effort has been made to technically adopt this principle in optics. Classical imaging always had its archetype in natural single aperture eyes as, for example, human vision is based on. But not always a high resolution image is required. Often the main aim is on a very compact, robust and cheap vision system.

Miniaturized digital cameras and optical sensors are important features for next generation customer products. Key specifications are resolution, sensitivity, power consumption, manufacturing and packaging costs and, maybe most important of all, overall thickness. Digital microcameras which are based on miniaturized classical lens designs used today are rarely smaller than 5x5x5mm^3. The magnification is related to the system length. Recent improvements of CMOS image sensors would allow further miniaturization. Nevertheless, as a result of diffraction effects, a simple miniaturization of known classical imaging optics would drastically reduce the resolution [3] and potentially also the sensitivity. A simple scaling of the imaging system to the desired size does not seem to be the clever way. How then to overcome these limitations of optics? A fascinating approach is to look how nature has successfully solved similar problems in the case of very small creatures [4].

During the last century, the optical performance of natural compound eyes was analyzed exhaustively with respect to resolution and sensitivity [2]. Several technical realizations or concepts of imaging optical sensors based on the principle of image transfer through separated channels were presented in the last decade. A detailed list is provided in Chapter 2, Section 2.2. However, since the major challenge for a technical adoption of natural compound eyes consists in the required fabrication and assembly accuracy, all those attempts have not lead to a breakthrough because classical, macroscopic technologies were exploited to manufacture microscopic structures. Sometimes only schematic macroscopic devices were fabricated. A statement of one of the scientists working on artificial compound eyes in the nineties was: "... Nature has to operate under certain material constraints for its optical designs, and artificial compound eyes will be able to take advantage of a wider assortment of optical materials and elements. ... On the other hand, it is unlikely that artificial compound eyes will be able to have the huge numbers of ommatidia present in their biological counterparts, due to manufacturing and connectivity limitations." [5]. For the early, rather macroscopic artificial compound eyes [6–8], this may be true.

1 Introduction

It is the aim of this thesis to show that these limitations can be overcome by using state of the art microoptics technology. This enables the generation of highly precise and uniform microlens arrays and their accurate alignment to the subsequent optics-, spacing- and optoelectronics structures. The result are thin, simple and monolithic imaging devices with the high accuracy of microoptics photo lithography. Many imaging applications could benefit from this bioinspired microoptics, where classical objectives will never find their way in. Compound eye cameras should for instance fit into tight spaces in automotive engineering, credit cards, stickers, sheets or displays, security and surveillance, medical technology and shall not be recognized as cameras.

In contrast to other attempts, here the imaging optics itself is considered as the key component to achieve this goal. (Opto-) Electronics and information processing will only take a minor part of this work. The main focus of this thesis is therefore on the fundamental analysis of imaging properties of compound eyes, the adaption of the optical design to the capabilities of microoptics technology, the formulation of new design strategies which match to the scaling laws of compound eye imaging systems, and the experimental characterization of realized demonstrators. It will be investigated how far technology can follow nature in the specific case of compound eye vision. In general, artificial compound eye concepts fit perfectly with microoptical fabrication technologies on wafer scale. However, for the current state of the art of technology, they are limited to planar arrangements while the natural archetypes are curved.

The explicit microoptics technology was carried out by cooperating groups of the Fraunhofer Institute Applied Optics and Precision Engineering, the Institute of Applied Physics in Jena, and the Institute of Microtechnology and SUSS MicroOptics SA in Neuchâtel, Switzerland.

Chapter 2 provides an introduction into natural compound eye vision, which is necessary to understand and classify the presented work on artificial compound eyes. The state of the art of microoptical imaging systems which have their archetypes in natural vision is subsequently discussed. Furthermore, an introduction into microoptics principles and scaling laws of imaging systems is given. At this point it can already be understood that microlenses offer good imaging quality because aberrations scale with the lens size. On the other hand, diffraction limitation seems to prevent microoptical imaging systems ever to stand in competition to classical imaging systems with some "megapixel" resolution. Nevertheless, it will be examined in this work whether bioinspired microoptics is able to establish new imaging functionalities and to open up new fields of applications to electronic imaging. A paraxial model based on a 3x3 matrix formalism which allows to describe even the very complex arrangement of microlens array telescopes with tilted optical axes is introduced.

In Chapter 3, the use of anamorphic microlenses for channelwise correction of off-axis aberrations in artificial compound eyes is discussed. This channelwise correction results in arrays of microlenses with varying parameters within an array. The necessary change of parameters (chirp) is derived analytically. The fabrication of anamorphic microlenses by reflow of photo resist on an ellipsoidal base is examined, and the aberration correction is demonstrated by spot

size measurements under oblique incidence using spherical and ellipsoidal microlenses.

In Chapters 4 and 5, two different objectives on the basis of artificial compound eyes are examined. In the apposition optics (Chapter 4), a microlens array is applied with a photo detector array of different pitch in its focal plane. The image reconstruction is based on moiré-magnification. The cluster eye approach (Chapter 5), which is based on a mixture of superposition compound eyes and the vision system of jumping spiders, produces a regular image. Here three microlens arrays of different pitches form arrays of Keplerian microtelescopes with tilted optical axes, including a field lens.

The two artificial compound eye concepts allow a decoupling of magnification and system length. Both types of objectives are analyzed with respect to theoretical limitations of resolution, spatial information capacity, sensitivity and system thickness. Explicit design rules and possibilities of simulation are derived.

For the artificial apposition compound eye objective (Chapter 4), several novel demonstrators are manufactured by photo lithographic processes. This includes a system with opaque walls between adjacent channels and an objective which is directly applied onto a CMOS detector array. Here, the full artificial compound eye visualization chain of the resulting camera including imaging optics, photon reception and close-to-the-receptor signal processing is demonstrated. The different systems are experimentally characterized with respect to resolution, sensitivity and cross talk between adjacent channels. Captured images are presented.

The novel cluster eye objective for imaging a large field of view is examined in Chapter 5. A special paraxial matrix treatment is used to describe the complex arrangement of arrays of microtelescopes. The obtained paraxial parameters are transferred to the parameters of real microlenses in lens arrays of variable parameters (chirped arrays) and are implemented in raytracing software, to further optimize the systems. Microlens arrays of a demonstrator system are fabricated using microoptics technology and are subsequently stacked to the overall microoptical system. The resulting objective is characterized with respect to resolution. Captured images are presented.

Finally, Chapter 6 concludes the results of the presented work and provides a detailed enumeration of future working tasks with respect to design, adaption to applications and technologies, in order to develop bioinspired microoptical vision from the proof of principle to commercial applications.

2 Fundamentals

Natural compound eyes have been subject to scientific research for more than one century. This has resulted in a huge amount of publications. This chapter only covers the essential basics of natural compound eye vision. For further reading, references [1] and [2] are especially recommended. The state of the art of microoptical imaging systems is discussed in the context of their natural vision archetypes. Furthermore, an introduction into the principles of microoptics and scaling laws of imaging systems is provided. Finally, a paraxial model based on a 3x3 matrix formalism is introduced, which allows the description of the complex arrangement of microlens array (MLA) telescopes with tilted optical axes in Chapter 5.

2.1 Natural Vision

There exist two known types of animal eyes [9]: Single aperture eyes and compound eyes. The latter can be further divided into apposition compound eyes and superposition compound eyes (Fig. 2.1). All of theses eye types can use refractive mechanisms for image formation while incorporating graded refractive index optics [10]. In single aperture eyes and superposition compound eyes, reflective mechanisms can be found as well [11, 12].

For small invertebrates having an external skeleton, eyes are very expensive in weight and metabolic energy consumption. If the budget is tight, nature prefers to distribute the image capturing to a matrix of several small eye sensors instead of using a single eye [1, 2]. The resolution of compound eyes is usually poor compared to that of single aperture eyes [13]. But the processing of highly resolved images would overload the brain of small insects anyway. In nature, this lack of resolution is often counterbalanced by a large field of view (FOV) and additional functionality such as polarization sensitivity or fast movement detection. By polarization sensitivity, the sun position can be detected without directly seeing it. Fast movement detection is obtained at the level of signal processing close to the eye because of cross linking of adjacent channel's receptors. The arrangement of optical channels on a spherical shell allows compound eyes to have a large FOV while the total volume consumption remains small. Hence, the main volume of the head is still available for the brain and signal processing. In the following, the different natural eye types are introduced.

2.1.1 Single Aperture Eye

The key advantages of single aperture eyes (Fig. 2.1, left column, top row) are high sensitivity and resolution. The small size of the FOV and the large volume of single aperture eyes constitute drawbacks. Furthermore, as single aperture eyes image only a limited FOV sharply, they must be moved to sample the entire visual surrounding. This is accomplished by means of eye or head movement. In addition, processing the large number of visual information in a highly resolved
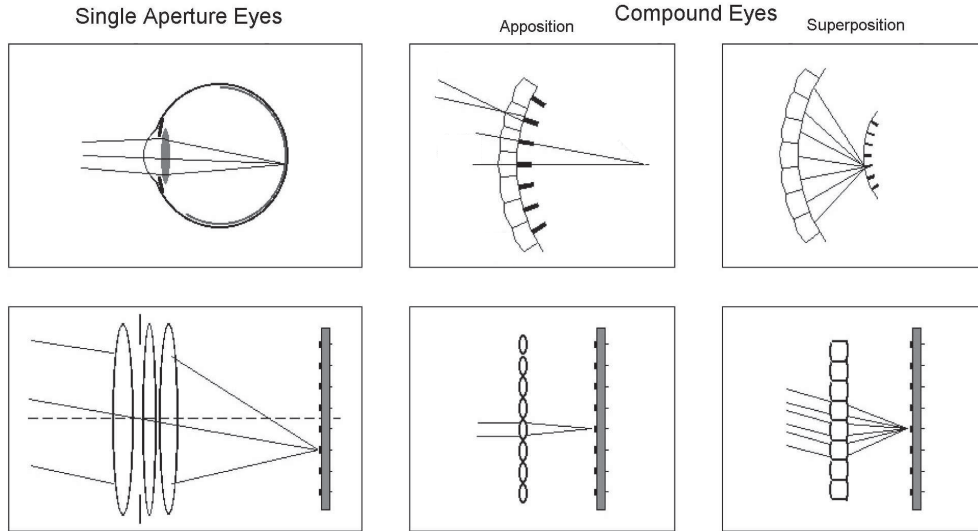
Figure 2.1. Different types of natural eye sensors (top) and their technical counterparts (bottom) [4]. "The division of fields in eyes like our own takes place in the retina after the lens, in compound eyes it takes place before that stage, in the optics, in lens eyes and cameras the fields can not overlap, in the compound eye they can, thus a compound eye can in toto catch more light." [14]

image requires a large brain. Since this is a scientifically well covered topic, this natural vision system is not discussed in more detail in this introduction.

2.1.2 Apposition Compound Eye

A natural apposition compound eye consists of an array of microlenses on a curved surface. Each microlens is associated with a small group of photo receptors in its focal plane. Apposition compound eyes have mainly evolved in diurnal insects such as flies (Fig. 2.2 (a)) [15]. The single microlens-receptor unit forms one optical channel and is commonly referred to as ommatidium. The term "microlens" is convenient and further used for referring to the focusing element. In fact however, the principal focusing element of the ommatidium is the crystalline cone, which has a graded refractive index, with highest index on the optical axis. Only minor contribution to the focusing is provided by the corneal lens [10, 16].

Pigments form opaque walls between adjacent ommatidia to avoid, in case of large angles of incidence (AOI), light which is focused by one microlens to be received by an adjacent channel's receptor. Otherwise ghost images and a reduction of contrast would result.

Natural apposition compound eyes contain several hundreds (water fly) up to tens of thousands (honeybee or Japanese dragon fly) of these ommatidia packed in non-uniform hexagonal arrays.

Interommatidial angle. Each ommatidium's optical axis points into a different direction of the object space (Fig. 2.2 (b)). For simplicity, only one photo receptor is assumed per unit.
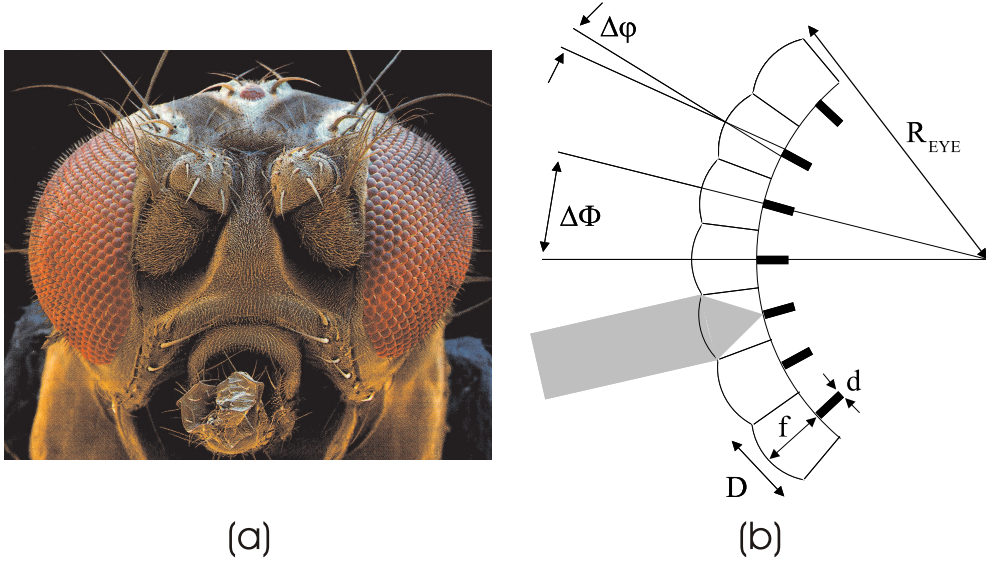
Figure 2.2. Natural apposition compound eye. (a) Head of the fruit fly "Drosophila melanogaster" (Photograph: Focus agency). (b) Operation principle of natural apposition compound eye: Apposition compound eyes are composed of hundreds up to tens of thousands of microlens-receptor units referred to as ommatidia arranged on a curved surface with radius R_{EYE}. Every microlens with diameter and pitch D and focal length f focuses light only from a small solid angle $\Delta\varphi$ of object space onto a small group of photo receptors. For simplicity one receptor with diameter d is assumed per unit. The eye samples the angular object space with the interommatidial angle $\Delta\Phi$. D and R_{EYE} determine the size of $\Delta\Phi$. The ommatidia are optically isolated by intermediate opaque walls for prevention of cross talk. The arrangement of ommatidia on a spherical shell allows natural apposition compound eyes to have a very large FOV while the total volume consumption is small.

The visual surrounding of the insect is sampled with the interommatidial angle

$$\Delta\Phi = D/R_{EYE}. \tag{2.1}$$

A response in the corresponding photo receptor results only if an object point is located on the optical axis of an ommatidium, or close to it. The image formation evolves by the contribution of all ommatidia's signals.

Nyquist angular frequency. A line pattern can be resolved if the ommatidia view alternating bright and dark stripes. The period of the finest pattern which can be resolved is consequently $2\Delta\Phi$ resulting in a sampling- or Nyquist angular frequency [17] of a natural apposition compound eye of $\nu_s = 1/(2\Delta\Phi)$ in case of a square lattice of ommatidia, which is assumed for simplicity. $\nu_s = 1/(\sqrt{3}\Delta\Phi)$ holds for a hexagonal lattice [18].

Angular sensitivity function. The angular distance ϕ of an object point from an ommatidium's optical axis determines the amount of response of the corresponding ommatidium. This

response is reflected in the normalized to unity angular sensitivity function (ASF).

$$\text{ASF}(\phi) = \exp\left[-4\ln 2\left(\frac{\phi}{\Delta\varphi}\right)^2\right]. \tag{2.2}$$

$\Delta\varphi$ is the full width of the function at 50% sensitivity (full width half maximum – FWHM). $\text{ASF}(\phi)$ is a radiant intensity. The angular integration of $\text{ASF}(\phi)$ over the full FOV of the ommatidium delivers the power at the receptor front face [19, 20].

Acceptance angle. The size of the so-called acceptance angle $\Delta\varphi$ defines, according to the Sparrow criterion [21], the minimum distance of two bright point sources which can still be resolved by the optics. $\Delta\varphi$ has a geometrical contribution $\Delta\rho = d/f$ which is determined by the receptor diameter projected into the object space. This is convolved with a contribution given by the diffraction at the microlens aperture [18] for the wavelength λ, resulting in

$$\Delta\varphi = \sqrt{\left(\frac{d}{f}\right)^2 + \left(\frac{\lambda}{D}\right)^2}. \tag{2.3}$$

Here a Gaussian photo receptor response is assumed. λ/D is the FWHM of the Gaussian approximation of the the Airy function describing the blur caused by diffraction [22]. In the angular domain, the diameter of the first dark ring is exactly given by $2.44\lambda/D$.

Modulation transfer function (MTF). The MTF [17] at the retinula cell level is obtained by the Fourier transform of the ASF in Eq. (2.2) [23, 24], normalized to unity at zero angular frequency ν

$$\text{MTF}_{ASF}(\nu) = \exp\left[-\frac{\pi^2}{4\ln 2}(\nu\Delta\varphi)^2\right]. \tag{2.4}$$

The finest resolvable sinusoidal pattern is defined by the optical cut-off $\text{MTF}_{ASF}(\nu_{co}) = 0$ of the lens of a single ommatidium [23]. In the Gaussian approximation of MTF_{ASF}, there is no finite value of ν satisfying this condition. A sufficient approximation of the angular cut-off frequency is given by $\nu_{co} = 1/\Delta\varphi$, which leads to $\text{MTF}_{ASF}(\nu_{co}) \simeq 0.028$ [19]. In the case of diffraction limitation, this consequently becomes $\nu_{co} = D/\lambda$ [14, 18]. Compound eyes are intrinsically low resolution structures because of the small diameter of the individual facets [25].

The size of the acceptance angle in relation to $\Delta\Phi$ determines the modulation for angular frequencies up to the eye's Nyquist frequency ν_s. $\Delta\varphi$ is a measure of the overlap or separation of the ommatidia's FOVs. As the general design rule, ν_s and ν_{co} would be expected to match roughly. Then the receptor mosaic is just fine enough to adequately sample the highest spatial frequency that the optics provide. There is no further information to be gained if the receptor mosaic is finer than given by ν_{co}. In practice, ν_s is found to be a little smaller than ν_{co} because at the optical cut-off the contrast of the image vanishes but the photo receptors require some contrast to work with.

2.1. Natural Vision

Eye parameter. The eye parameter $P = D\Delta\Phi$ is a common quality criterion in animal physiology. Its lower limit can be derived if the influence of diffraction λ/D in Eq. (2.3) is assumed to be much larger than the geometrical contribution $\Delta\rho = d/f$:

$$\nu_{co} \geq \nu_s, \quad \text{or} \quad 1/\Delta\varphi \geq 1/(2\Delta\Phi), \quad \text{or} \quad D/\lambda \geq 1/(2\Delta\Phi), \quad \text{or} \quad P = D\Delta\Phi \geq \lambda/2. \quad (2.5)$$

D and $\Delta\Phi$ are parameters that can be determined directly in animal physiology. The size of P with respect to $\lambda/2$ reveals how close to the diffraction limit a compound eye works. Using Eq. (2.3), information about the size of $\Delta\rho$ can be obtained. This reveals the loss of resolution which the insect pays for an increase of sensitivity. As a consequence, P allows the determination of an arthropod's illumination habitat. Insects operating in brilliant sun light have almost diffraction limited eyes. E.g. the Australian sand wasp "Bembix" has $P = 0.32\mu$m at $\lambda = 0.5\mu$m [26]. Nocturnal animals on the other hand, as for instance the king crab "Limulus" ($P \approx 31\mu$m), show a tendency towards high light gathering power [25]. Here, diffraction limited resolution is no issue.

The functionality of the eye in the natural living habitat is of highest importance. This is however not guaranteed by a fine resolution if not enough photons are entering the eye. The functionality is mainly determined by capturing a sufficient amount of photons to distinguish a certain pattern from noise [13] – by sensitivity.

Sensitivity. The sensitivity of an imaging system to an extended source of a standard luminance is given by the intensity in the image plane of the lens [27–29] multiplied by the receptor area and the absorption K of the receptor

$$S = \frac{\pi}{4(F/\#)^2} \frac{\pi}{4} d^2 K = \left(\frac{\pi}{4}\right)^2 \left(\frac{D}{f}\right)^2 d^2 (1 - \exp^{-kl}). \quad (2.6)$$

Here, k stands for the natural extinction coefficient of the photo pigment in the receptor of the length l. $F/\#$ denotes the F- or stop number of an optical system and is defined by the focal length f over the system aperture diameter D [17]. Evident waveguide effects within the receptors can be neglected in a first order examination. Unity transmission is assumed. By substituting the geometrical part of the acceptance angle $\Delta\rho = d/f$, the trade-off between sensitivity and resolution becomes obvious

$$S = \left(\frac{\pi}{4}\right)^2 D^2 \Delta\rho^2 (1 - \exp^{-kl}). \quad (2.7)$$

If sufficient light power is available $\Delta\rho$, and consequently also P, can be small. This allows a resolution close to the diffraction limit. However, $\Delta\rho$ and thus P are increased the more, the lower the light level of the natural living habitat is, or the faster the insect moves. Higher sensitivity enables the same overall number of captured photons for shorter image capturing times or lower ambient illumination. Sensitivity is the reason for compound eyes possessing a similar $F/\#$ compared to that of single aperture eyes [30]. In the case of superposition compound eyes of nocturnal arthropods, $F/\#$ can even be much smaller.

The optimum compromise between resolution and sensitivity in the case of sufficient ambient illumination is the Airy disk diameter matching the receptor diameter [31].

Scaling of natural compound eyes. How to increase the resolution of a compound eye? Substituting $\Delta\Phi = D/R_{EYE}$ in the right part of Eq. (2.5) yields

$$R_{EYE}\Delta\Phi^2 \geq \lambda/2, \tag{2.8}$$

and with furthermore substituting $\nu_s = 1/(2\Delta\Phi)$, it follows

$$R_{EYE} \geq 2\lambda\nu_s^2. \tag{2.9}$$

The eye radius is proportional to the square of the required resolution. In contrast, in single aperture eyes this scaling is linear. The problem arises because, in compound eyes, the ommatidia must increase in both number and size in order to increase resolution [32]. The eyes become too large or reveal, for the same size, a much lower resolution than single aperture eyes (Fig. 2.3).
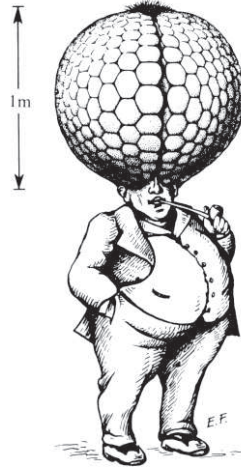
Figure 2.3. "A man would need a compound eye of at least 1m diameter to get the same angular resolution as with his lens eye." [33].

Special properties of compound eyes. This is the reason why many invertebrates developed compound eyes which have areas with a locally higher resolution, "acute zones", than elsewhere in the eye. These acute zones point into the direction of highest interest, similar to the fovea in the eyes of mammals [25, 26].

Because the applied microlenses have an extremely short focal length, the ommatidia provide an incredibly large focal depth. The image plane of the microlenses is always located in their focal plane, independent of the object distance (Eq. (2.19)). Hence, the angular resolution is constant over a large range of object distances if the acceptance angle is well matched to the angular sampling by the ommatidia. The spatial resolution scales linearly with the object distance [34].

Every channel works on-axis for its direction of view as a further effect of the arrangement of ommatidia on a spherical base and the separated image point generation. One channel does not have to transfer an overall large FOV, as a conventional single aperture eye has to. This results on the one hand in the lack of off-axis aberrations which lead to a strong degradation of resolution with increasing image height. On the other hand, compound eyes do not suffer from the $\cos^4$-law [29,35] which is responsible for the decrease of relative illumination with increasing image height. Compound eyes are therefore the optimum optical arrangement for large FOV vision. The large FOV of each compound eye furthermore results in a huge binocular field providing stereoscopic vision to which more than 70% of ommatidia contribute [36].

For point sources, a "hyperacuity" – a resolution beyond the diffraction limit – can be achieved with natural apposition compound eyes [5, 20]. The difference of the response of adjacent ommatidia to a point source within their overlapping ASFs is exploited to determine the relative position of the point source. Differences in signals can be evaluated very accurately.

Apposition compound eyes can furthermore gain superposition character by neural pooling of the different receptors in adjacent ommatidia [28]. This can be seen as an intermediate compound eye type, between apposition and superposition compound eye. This principle can be observed in a large variety of flies. Those compound eyes are called "neural superposition eyes" and provide different applications. By pooling receptors of adjacent ommatidia, which have different amounts of offset from the corresponding ommatidium's optical axis, an increased sensitivity is achieved. The ommatidia effectively look into the same direction. This improvement of sensitivity is accomplished without loss of resolution which would occur with a simple increase of receptor size. Furthermore, flies use this receptor pooling for very sensitive, hyperacuite movement detection.

The small axial distance between the microlens and the receptor layer in apposition compound eyes in general makes them the perfect archetype for extremely thin digital optical sensors. A thin artificial apposition compound eye objective will be discussed in Chapter 4.

2.1.3 Superposition Compound Eye

The natural superposition compound eye has primarily evolved in nocturnal insects and deep water crustaceans (Fig. 2.4). The light from multiple facets combines on the surface of the photo receptor layer to form a single erect image of the object [9]. For the refractive type, this optical performance is not the result of a single MLA layer but of an array of microtelescopes. These microtelescopes also incorporate graded index lenses [37, 38]. Compared to natural apposition compound eyes, natural superposition compound eyes are much more light sensitive. Eyes with small $F/\#$, even smaller than one, have been observed. Aberrations – similar to spherical aberrations, but caused by the combination of light combined from many facets – lead to a resolution far from the diffraction limit [39, 40]. Some insects use a combination of both types of compound eyes. Variable pigments switch between apposition (daylight) and superposition (night) or change the number of recruited facets making up the superposition image [41].
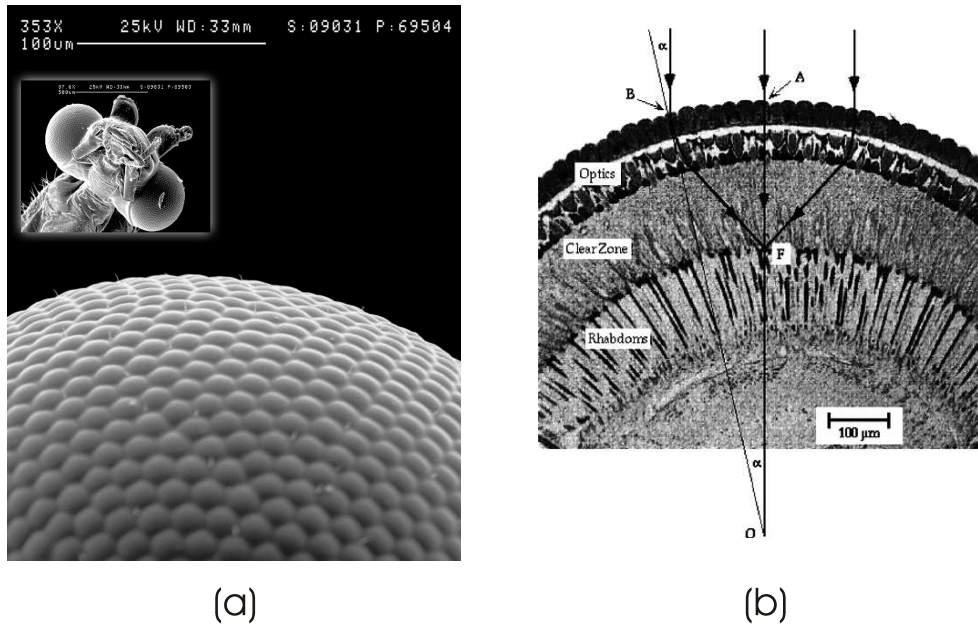
Figure 2.4. Natural superposition compound eye. (a) Scanning electron microscope image of head and eye section of the moth "Ephestia Kuehniella". (b) Cross section of natural superposition compound eye of moth "Phalaenoides Tristifica" [41].

Diffraction and raytracing models were used to determine the amount of aberrations of a natural superposition compound eye necessary to reproduce the experimentally obtained data of resolution [41, 42].

2.1.4 Vision System of the Jumping Spider

In contrast to other insects, jumping spiders have opted for single aperture eyes. But they use eight of them. Jumping spiders possess two high resolution eyes, two wide angle eyes and four additional side eyes (Fig. 2.5). The two antero median eyes provide a magnified image at a high resolution for a rather small visual field [43]. The antero median eyes have a Galilean telescope like optical arrangement [44] leading to a telephoto feature. Jumping spiders use these eyes for detailed inspection of objects of interest. Furthermore, these eyes have a movable retina. This retina can be moved vertically, laterally and rotationally. The spider can track a prey without moving itself. The two antero lateral eyes provide a large visual field at a reduced resolution. The small side eyes cover the large field left and right of the spider.

Jumping spiders do not have compound eyes because their resolution would be too poor to identify targets worth to jump to. To be equipped with high resolution single aperture eyes, such as vertebrates, spiders are too small.

This natural design concept, to distribute the image capturing task to an array of different single aperture eyes, is the most promising approach for very small imaging systems and microcameras [4] and will be discussed in Chapter 5.
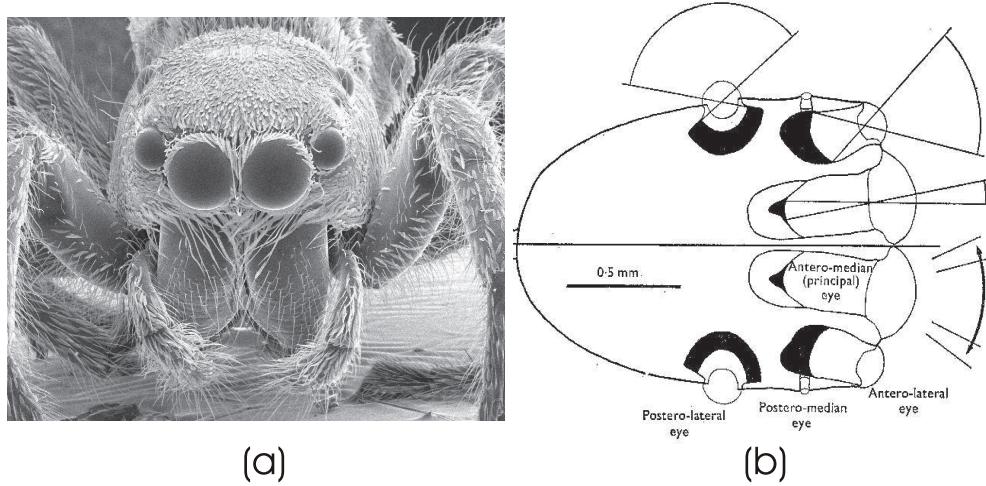
Figure 2.5. Vision system of the jumping spider "Araneae: Salticidae". (a) Scanning electron microscope image (Photograph: Aaron Bell). (b) Schematic cross section of head. Different eyes have different FOVs, directions of view and resolutions. The direction of view of the principal eyes can be changed by moving the retina (Drawing: Wayne & David Maddison).

2.2 State of the Art of Man-Made Vision Systems

There is a high attraction in trying to adopt natural photonic principles in unorthodox technical solutions [45]. This also holds for imaging systems. Distributing the image capturing task to an array of microlenses instead of using a single objective, will provide a large number of functionalities for technical imaging applications. This can be expected from the analysis of natural compound eyes [46]. Miniaturization and simplification are primary demands. In the following, the state of the art of man-made imaging systems based on the above discussed natural vision principles is introduced.

Single aperture eye – classical objective. Single aperture eyes served as archetypes for the classical single aperture objectives (Fig. 2.1, left column, lower row) [17, 47]. The properties of those classical optics have by now become well understood [29, 35, 48–55].

There is a fundamental relationship between the FOV of an imaging system and the corresponding image size (Fig. 2.6 (a)) which, in digital imaging, must be matched to the digital sensor array size. This size is given by the product of the pixel size and pixel number. The required magnification is defined by the focal length of the objective:

$$f = \frac{a_D}{2 \tan(\alpha)}, \qquad (2.10)$$

where a_D denotes the size of the detector diagonal and α the size of half the diagonal FOV [17]. The focal length of the objective roughly determines the system length for imaging systems with a telephoto ratio close to unity and under the assumption that the image space is mainly filled by air. This relationship fundamentally limits the possibilities of miniaturization of classical imaging systems: The pixel size miniaturization is limited not only as a result of limited

manufacturing resolution of the detector arrays. Especially a required high sensitivity and diffraction effects determine minimum pixel sizes (Section 2.3). On the other hand, a large number of pixels is required in order to achieve high image resolution. This leads to large sensor array areas while the FOV is always determined by the imaging application. As a consequence, imaging systems with a thickness below the millimeter magnitude based on the single aperture eye principle do not seem to be practical. Furthermore, large lens sags of the order of magnitude of millimeters are required. This prohibits the use of well established microoptical fabrication technologies.
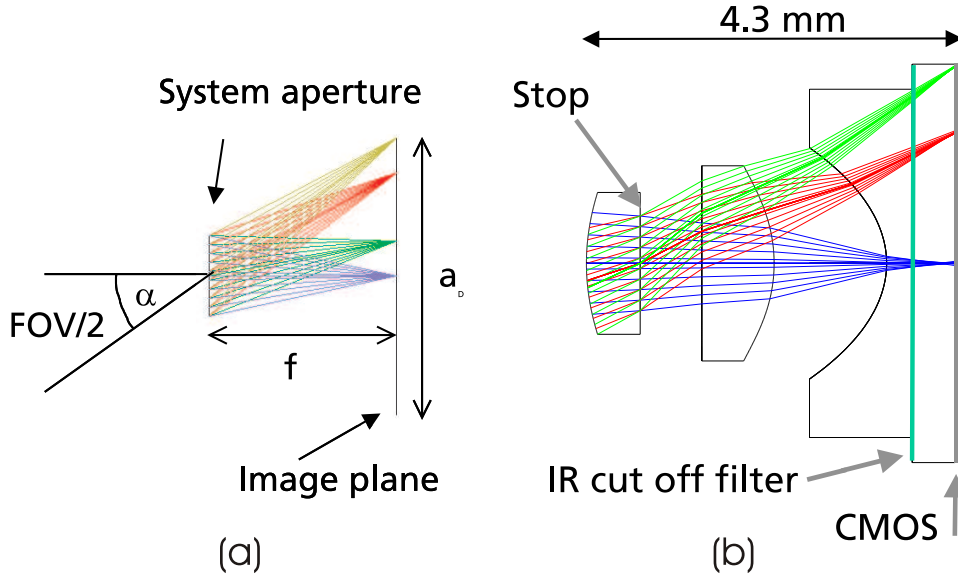
Figure 2.6. Layout of a single aperture objective. (a) The system length of a classical objective is mainly determined by its focal length and hence the desired magnification. (b) Compact triplet incorporating three polymer microlenses and a fused silica plate holding a dielectric IR cut-off filter on the front side. On the substrates backside a thinned CMOS sensor array is located.

Exemplarily, a compact objective (Fig. 2.6 (b)) for a VGA sensor with 640x480 pixels and pixel size 5.6μm for application in mobile phone cameras is presented, which was designed (patent pending [56]) and experimentally demonstrated by ourselves [57]. This objective was specified by the following parameters:

- Length: 4.3mm

- Image circle diameter a_D: 4.5mm

- FOV half angle: 35°

- $F/\#$: 2.8

- MTF: > 30% at 45LP/mm

- Distortion: -0.25% < Γ < 0.36%

LP denotes line pair [17]. The optics layers are fabricated by hot embossing, for instance of PMMA. As a result of the high required lens sags, tools are fabricated by single point precision diamond turning of lens pins which are subsequently assembled to arrays. The different microlens layers are assembled on wafer scale to the objective (patent pending [56]). Afterwards, the array of objectives is assembled to the array of sensors, also on wafer scale. Using alignment marks for all the wafer scale assemblies of the cameras, accurate alignment for all modules is achieved at once. Costs are reduced. Finally the modules are separated by wafer dicing.

Even though this objective shows an innovative fabrication method it on the other hand demonstrates the limitation of system miniaturization of classical single channel objectives.

Apposition compound eye – autonomous robots, optical sensors for defense and surveillance, flat bed scanner, integral imaging, compact cameras. Various technical approaches for compact vision systems adopted the principle of small natural apposition compound eyes using planar MLAs (compare with lower row of second column in Fig. 2.1).

A general examination of the properties of natural apposition compound eyes and of the possibilities using artificial derivates of those was given in [5].

A graded index MLA of the planar type [58, 59] was applied as an image multiplexer [60]. Using MLA processors and optical array logic was proposed for digital optical computing [61–64]. Optical correlators also apply MLAs [65].

Having an MLA and a photo detector array of equal pitch, a 1:1 imaging is achieved. This results in two-dimensional large area image sensors which work as flat bed scanners [66, 67]. Contact type 1:1 image sensors with [68] and without microlenses [69] for instance for fingerprint reading have been proposed. These image sensors mainly contain optically isolated cylindrical channels with corresponding photo detectors.

Graded index MLAs of the rod type in front of pinhole arrays and photo diode arrays built up an artificial apposition compound eye [7]. Here a bulk diverging lens was used to provide the overall FOV. The overall image reconstruction is explained by the moiré-magnification. A detector geometry with large pitch and low fill factor (ratio of optically sensitive area to unit cell area) has to be applied in order to achieve a high resolution with the moiré image reconstruction. Different arrangements of graded index microlenses and pinholes in the cells of the array allow scale-invariant processing. A difference in pitch leads to a factor of magnification which can also be interpreted as enlargement of the FOV [8]. In this approach, the number of image points is in general equal to the number of ommatidia. This results in a drawback of the systems described in the literature because here the number of ommatidia is very small.

The same applies to other attempts where for instance MEMS (Micro-Electro-Mechanical-Systems) technology is used. A scanning retina for a change of direction of view was realized [70–72]. For applications in robotics and surveillance not even lenses were applied [73] – the system acting like an array of pinhole cameras. Here always comparatively low attention to the quality of the optical imaging system itself was paid with respect to the high effort in the electro mechanics resulting in a poor resolution. The natural archetype of this compound eye

without lenses, using only shadowing for image formation, can for instance be found in flat- or tube worms [9]. Here, single photo receptors lie at the bottom of pigmented tubes.

An autonomous navigating robot was developed using an array of elementary motion detectors based on a macroscopic artificial apposition compound eye objective (APCO) in a radial arrangement [6]. The detection of bright sources and its tracking was achieved by fuzzy control algorithms in combination with a macroscopic APCO [74]. Macroscopic ommatidia with conical body and in a curved arrangement are also suggested to form an APCO [75]. APCOs found application in target detection and tracking for defense and airborne applications [76, 77]. A fiber bundle surveillance sensor for defense applications [78] has the light receiving fiber ends arranged on a curved basis. The corresponding output fiber ends are attached to photo detectors.

For infrared vision, MLA-detector array arrangements without a pitch difference are proposed for fill factor enhancement using binary microlenses [79] or directly as imaging system using a pitch difference between refractive MLAs and the photo detector array [80, 81].

A combination of MLAs with associated groups of photo detectors, all groups having a different amount of shift with respect to the microlenses was also proposed as imaging device [82] with binary MLAs [83] and in the integration with liquid crystal displays [84, 85].

Furthermore an MLA with microlens segments which are decentered with respect to their channel origin as a function of the channel's radial position within the camera and photo detectors, which are centered within the channels, are proposed [86, 87]. For each microlens segment (optional also with diffractive components attached to a convex surface), the decentration with respect to the photo detector results in a difference in the corresponding channel's viewing direction. Biconvex aspherical microlenses are proposed for the MLA structures [88] to reduce aberrations. Color imaging is made possible be applying three photo detectors within each channel, with different color filters attached in front of each.

Dispersive microlenses chirped with respect to direction of view of the corresponding channel are proposed for color imaging where the diffraction at a microlens splits the wavelengths to be detected by separated equivalent detectors [89].

In the "TOMBO" system [90–92], only a small number of channels is used, but each cell of the system has a matrix of associated photo receptors which pick up all the information of the micro-images. The microlenses (different types were tested: graded index, refractive, binary) are centered with the matrix of photo detectors capturing the micro-images. The difference in the micro-images is the result of the different radial positions of the corresponding channel within the array (slightly different offset). For close objects, the information content of the overall image calculated from all the micro-images is much larger than that of the single micro-images. The information capacity is related to the aperture of the overall array rather than to that of a single microlens. As one choice, the back projection algorithm is used to retrieve the overall image from the many micro-images. The computed image reveals a much higher resolution than only the number of cells. However, there is the burden of an extraordinary

complex image processing [93]. Even color imaging was made possible [94] through applying color filters on the detector pixels in a Bayer pattern within each channel or by changing color filters from channel to channel. Nevertheless, up to date commercial applications of this principle did not come up. This is probably because this approach is only applicable for object distances in the order of magnitude of the lateral array extension. For larger objects distances, the difference in the offset of the micro-images with respect to the channel origin is negligible and the complex image processing does not lead to images with higher resolution than that of the single micro-images.

Three dimensional imaging – also known as integral photography [95–101] – and displaying [102–104] can also be seen to have its archetype in natural apposition compound eyes because they are related to MLA imaging. Here the offset of all the micro-images with respect to the microlens origin is used to extract a depth information. This is however a large and completely different topic and will not be further discussed at this point.

Crossed cylindrical MLAs used in combination with a photo detector array build up an apposition compound eye imaging sensor [105, 106], two of those devices are used as objectives for stereoscopic vision.

The combination MLA-photo detector array is also known as solid state image sensor- or pickup device [107, 108]. It is used in the image plane of a bulk objective instead of a simple photo detector array to increase the fill factor. This device is also called "focal plane array". Diffractive microlenses, with each photo detector centered with its associated microlens have been proposed [109]. In the case of non-telecentric bulk objectives, a pitch difference between MLA and detector array can be applied. This results in tilted optical axes, where the tilt is a function of the radial coordinate of the considered image pixel. This pitch difference avoids the foci of the microlenses to move from the detector pixels with increasing field angle. A radial variation of illumination in the image is prevented [110–112]. Curved MLAs [113] also have been proposed for this purpose, even in combination with curved sensor arrays [114].

Most of the described technological approaches of APCOs for compact vision systems suffer from assembly misalignment errors of the individually fabricated components. This prevented the realization of functional thin cameras with a large number of pixels. Macroscopic technologies were tried to be used to realize microscopic devices.

As a consequence of the small required lens sags artificial compound eyes are well suited for microoptical fabrication technologies. These allow wafer level manufacturing of compound eye objectives with a large number of channels. Utilizing photo lithographic processes results a highly precise lateral accuracy of the compact imaging systems. Fabrication- and assembly technologies on wafer scale lead to cheap and compact imaging devices because of the parallel manufacturing of many systems at once.

A compact imaging system in a planar layout based on the APCO [82, 88] accounting for these issues is the first imaging principle pursued in this work. It is described in Chapter 4.

Superposition compound eye − Gabor superlens, copying machines, X-ray optics. The natural superposition compound eye and its technical derivate are represented in the right column in Fig. 2.1.

An ultra wide FOV imaging system based on refractive superposition compound eyes was analyzed by raytracing simulation [115].

Multiple mirror telescopes are applied in astronomy [116, 117] to enhance the collecting capacity and the resolving power [118, 119].

Artificial reflective superposition compound eyes based on crayfish eyes [12, 120–124] found applications in X-ray optics [125] because there are no refractive materials available in this wavelength range.

The planar technical equivalent of the refractive natural superposition compound eye is the Gabor superlens [126]. A large variety of imaging applications and manufacturing methods were proposed for this lens [127–132]. It could also be used as a panoramic imager when arranged on curved surfaces [133].

A Gabor superlens is formed by two MLAs of different pitches, having infinite conjugates (Fig. 2.7). The two confocal MLAs build up an array of beam steering miniature telescopes. The pitch difference of the two MLAs introduces a continuous displacement of the microlenses in the second array, bending all bundles towards a common focus [134]. Let p_1, f_1 and p_2, f_2
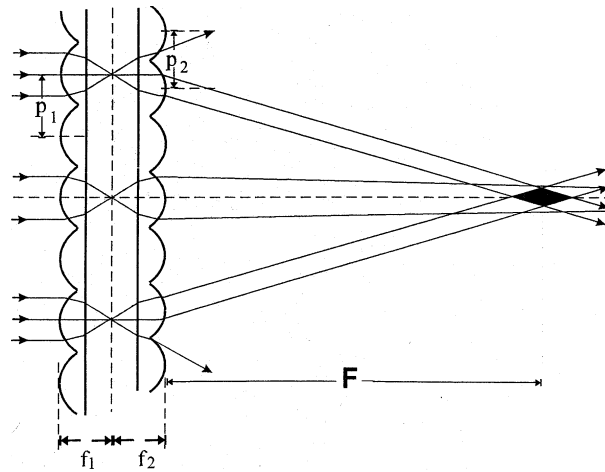
Figure 2.7. Gabor superlens [134].

be the pitches and focal lengths of the first and the second MLA, respectively. For large object and image distances $s \gg f_1$ and $s' \gg f_1$ the imaging equation becomes especially simple [135]

$$\frac{1}{F} = \frac{1}{s'} + \frac{f_1}{f_2}\frac{1}{s}.$$
(2.11)

F is the back focal length of the Gabor superlens.

$$F = f_2 \frac{p_1}{p_1 - p_2}.$$
(2.12)

The Gabor superlens comprises several interesting imaging properties, such as generating an erect image. From Eq. (2.11) the lateral and axial magnification m and $\hat{m}$, respectively, can

be calculated

$$m = 1 - \frac{s'}{F} \quad \text{and} \quad \hat{m} = \frac{f_1}{f_2} m^2. \tag{2.13}$$

The relative shift of the MLAs repeats after $p_1/(p_1 - p_2)$. Each structure larger than that always represents an array of Gabor superlenses which have no sharp aperture but overlap, with the efficiency of each Gabor superlens decreasing towards the edge due to the increase of spurious light. The Gabor superlens will constitute the basis of the mathematical treatment of the cluster eye in Chapter 5.

The closest technical application of the refractive natural superposition compound eye can probably be found in highly symmetric one-to-one imaging systems as for instance in photo copying machines using graded index MLAs [136–139]. In photo copying machines, numerous channels of the overall array contribute to the formation of one image point in order to achieve a high light gathering power [140]. Moreover, concepts of imaging systems using graded index MLAs were proposed which incorporate a certain degree of magnification or demagnification [141–144].

Vision system of the jumping spider – autonomous robots, compact large-area projection, compact cameras and relay optics. The parallel transfer of different parts of an overall FOV by isolated optical channels has already become the basis of many technical imaging principles.

The microlens photo lithography [145–149] applies a highly symmetric one-to-one telescope imaging system. A photo lithographic mask is transferred into photo resist with homogeneous image quality over eight inch wafer diameter with only millimeter working distance and a large focal depth. For the microlens photo lithography, an overlap of images transferred by adjacent channels is not desired because the different optical path lengths, when imaging a source point through different channels, leads to undesired interferences. Furthermore, non-symmetric aberrations are suppressed because of the highly symmetric arrangement. Each channel's object and image size is the same and is of the size of the channel pitch. However, this will not be possible for more camera like imaging systems, where object and image size are different in the order of magnitudes.

A close-up imaging of documents, displays and intermediate images ("relay optics") with refractive microlens- [150] or telescope arrays having a unity magnification [66, 67, 151–154], variable magnification using Alvarez lenses [155] or small demagnification [156, 157] was proposed, theoretically analyzed or experimentally demonstrated.

A so called stacked array magnifier using refractive and non-refractive MLAs [158, 159] for forming a magnified, demagnified or unit image was proposed. Microtelescope arrays were also analyzed in combination with macroscopic lens arrays [98, 99]. Stacked MLAs are furthermore used for optical or information processing [160, 161] and in many other kinds of microoptical systems [162].

A compact digital imaging system with segmented fields of view has been proposed in Refs. [163, 164]. Here, an array of segments of microlenses which are decentered with respect

to the channel origin is applied. The decentration is a function of the channel's radial position within the camera. Each microlens is associated with a matrix of photo detectors which pick up the partial-image under the direction of view. The microlens decentration with respect to the photo detector group results in a difference in each channel's viewing direction. Each channel images a small portion of the overall FOV. The partial-images are electronically rotated by 180° and attached to retrieve one overall image corresponding to the system's FOV. Diffractive components are optionally attached to the convex surfaces. In this system, however, each channel has only a small FOV. The imaging system's magnification must be large because the partial-images must have at least a sufficient size, at a small FOV. The partial-image size is given by detector size and number. The magnification is still determined by the focal length of the microlenses. The focal length and thus the imaging system's length is consequently similar to that of classical single channel imaging systems. Furthermore, for large focal lengths the necessary microlens decentrations must be large in order to allow an annexation of all the channel's FOVs and to avoid their overlap. This results in steep microlens structures. The capability of system miniaturization and simplification using this approach is hence drastically limited. The only advantage is seen in the possibility of correction of field aberrations for the channel's main viewing directions. By adding a field MLA and a relaying MLA, all with different pitches, results an imaging microtelescope array with tilted optical axes [165–167]. This is similar to Anderson's concept [156].

The parallel imaging of different parts of a distant object by isolated optical telescope channels builds the basis of the second concept of a compact digital camera [156, 159, 165, 167] pursued in this thesis. The proposed system is a superposition compound eye as a result of the arrangement of the refracting surfaces. On the other hand, the system is to some degree also an APCO because of the implementation of a field aperture array. It will be called cluster eye (CLEY) and this will be dealt with in Chapter 5.

2.3 Scaling Laws of Imaging Systems

In the previous sections, resolution or information capacity, sensitivity and size were introduced as primary parameters of imaging systems. In the following, the interaction of these quantities is analyzed in the very detail since miniaturized imaging systems are of interest in this thesis. Small imaging systems will be shown to have completely different pros and cons than large ones.

2.3.1 Resolution and Space Bandwidth Product

First order parameters. Imaging lenses and objectives are characterized within first order optical theory by their focal length f and aperture D. The so called F- or stop number

$$F/\# = f/D \qquad (2.14)$$

and the numerical aperture (NA) in air

$$\text{NA} = \sin\left(\arctan(1/(2F/\#))\right) = \sin\left(\arctan(D/(2f))\right) \tag{2.15}$$

can be derived from that [48]. For large $F/\#$, this can be simplified to $\text{NA} = (2\,F/\#)^{-1} = D/(2f)$.

Diffraction limitation. For an incident plane wave the focus distribution caused by diffraction effects at the circular lens aperture is represented by the lateral and axial dimensions of the point spread function (PSF) d_F and l_F, respectively. d_F and l_F are given by the diameter of the Airy disk in the spatial domain in the lenses focal plane:

$$d_F = 2.44\,\lambda\,F/\# \simeq 1.22\lambda/\text{NA} \tag{2.16}$$

and the length to the extension of the blur circle to its double diameter:

$$l_F = \pm 2\lambda(F/\#)^2, \tag{2.17}$$

respectively [23]. The PSF deviates the more from the Airy function the stronger the aberrations in the optical system are. The PSF usually also shows a dependence on the field angle.

Spherical aberration. The optical path difference (OPD) from the perfect sphere which occurs when focusing a plane wave by a plano convex lens with the refractive index n into air because of 3rd order spherical aberrations can be derived as [54]

$$\text{OPD}_{spherical}(\eta) = \frac{n^2\,D}{128(n-1)^2(F/\#)^3}\,\eta^4 \quad \text{with} \quad 0 < \eta < 1, \tag{2.18}$$

where η is the relative pupil coordinate. Here the plane side of the lens is oriented in the direction of the incident plane wave. According to Eq. (2.18) the spherical aberrations increase to the third power with decreasing $F/\#$ and scale linearly with D. If the curved side faces the incident plane wave the refraction is split up on two surfaces. This results in drastically reduced spherical aberrations [168].

The OPD always has to be considered with respect to λ, which is constant, to derive its effect on the PSF. It can thus be expected that spherical microlenses with NA up to 0.2 – in contrast to macroscopic lenses – show a diffraction limited performance. The full aberration polynomial can be found in [54]. The polynomial demonstrates that also aberrations which are mainly a function of the field angle have minor influence for small lens diameters.

Focal depths. The position of the image plane of a microlens converges to its focal plane the more, the smaller the focal length is compared to the object distance

$$\frac{1}{f} = \frac{1}{s} + \frac{1}{s'} \quad \Rightarrow \quad s' = \frac{fs}{s-f} \quad \overset{s \gg f}{\rightarrow} \quad s' = f. \tag{2.19}$$

A microlens has consequently a large geometrical focal depth.

Information capacity. The amount of information that can be transferred by a lens changes when scaling the focal length with constant $F/\#$. $F/\#$ shall be fixed in order to maintain the sensitivity according to Eq. (2.28). For other types of scaling see e.g. [169]. From Eq. (2.16) it follows

$$F/\#_1 = F/\#_2 \overset{Eq.(2.16)}{\rightarrow} d_{F_1} = d_{F_2} \overset{f_1 \gg f_2}{\rightarrow} \Delta\varphi_1 \ll \Delta\varphi_2. \tag{2.20}$$

The spatial size of the diffraction limited PSF, d_F, in the lenses focal plane is invariant. The angular projection of d_F into object space, however, increases with further miniaturization (Fig. 2.8 (a), (b)). Scaling with constant $F/\#$ also means the maintenance of FOV. Fewer ASFs fit in the lenses' FOV, and the amount of transferred information is decreased.

The same relation is now discussed in the context of the space bandwidth product [3,4,169]. This product is defined as the ratio of the area of the lenses image field and the area of one image pixel (considered to be a square). The space bandwidth product is representing the number of image pixels χ_{P/A_I} which can be transferred by an optical system. In other words, it is the spatial information capacity of the lens. Let the imaging lenses or objectives provide a square image field being the inner square of the lens circle with diameter D. Then the image area is $A_I = D^2/2$. The minimum distance of two light sources which can be resolved by the optical system after the Rayleigh criterion [23] is $d_F/2$. Following the Nyquist criterion [17], two image pixels are required to correctly detect the bright/dark distribution of one source point. The minimum distance of image pixels is $d_F/4$. The spatial information capacity of a lens consequently becomes

$$\chi_{P/A_I} = \frac{A}{d_F^2/4^2} = \frac{8}{2.44^2} \frac{D^2}{\lambda^2 (F/\#)^2}. \tag{2.21}$$

Miniaturized imaging systems only suffer from low resolution as a result of diffraction effects at the lens apertures, because the size of the image field decreases with D^2 and the diffraction limited PSF remains constant. Small lenses can transfer fine details such as large lenses do, but not a large number of details (Fig. 2.8 (c), (d)). Aberrations have minor effects, they decrease linearly with D. This can be seen, besides compactness, as one of the major advantages of microoptics.

Since the space bandwidth product scales with the lens area it makes sense to use a large number of microlens channels in parallel [3, 147, 169]. Each channel transports the amount of information according to its own space bandwidth product. The adjacent channels separately transport the adjacent image pixels (Fig. 2.8 (e)). Consequently, the overall number of transported information is much higher than that of the single channel, if it is ensured that each channel actually views a different part of the information. The axial compactness is still determined by the properties (focal length) of the single microlens.

This is for instance the case in 1:1 imaging systems such as microlens photo lithography or copying machines, where the object size equals the lens size. For large FOVs – for imaging far distant objects – it applies for imaging systems with segmented fields of view and separated viewing directions like in natural compound eyes with the arrangement of ommatidia on a
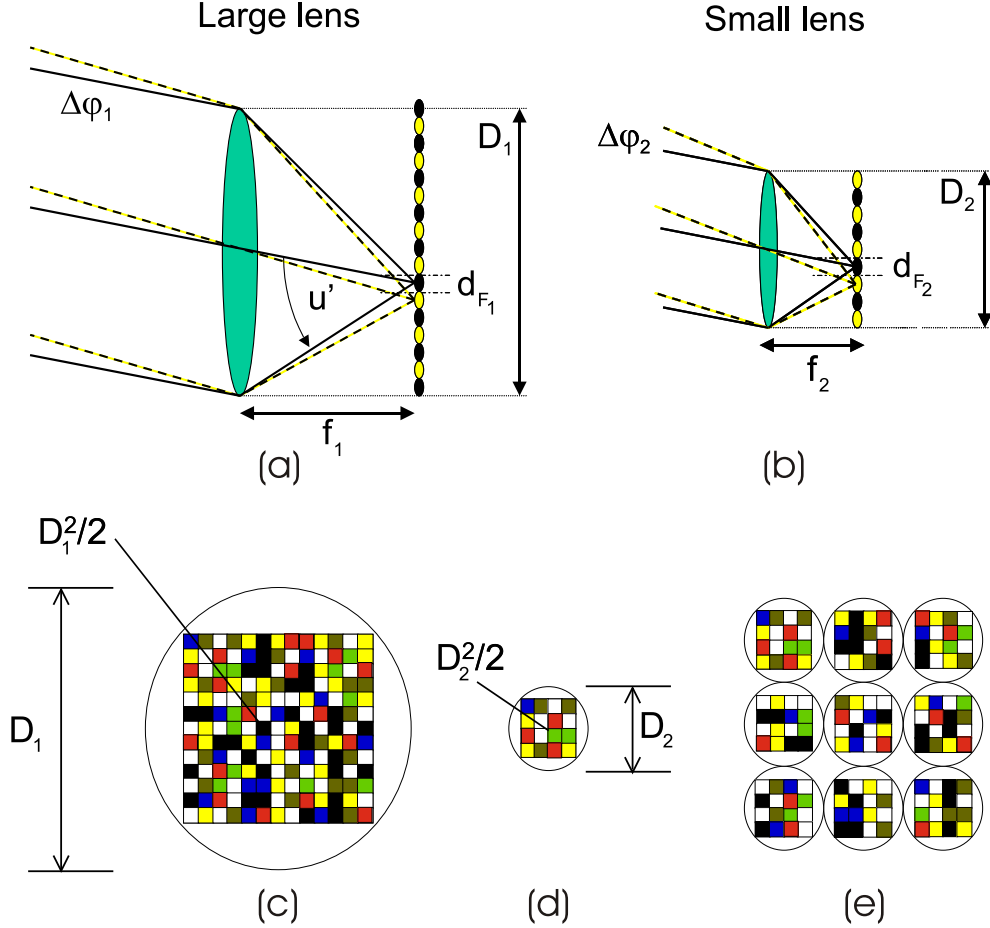
Figure 2.8. Scaling of lenses with constant $F/\#$ [4]. (a) Large lens. The size of one image point is given by Eq. (2.16). As a result of the large focal length f_1 the angular projection of the Airy disk in the object space $\Delta\varphi_1$ is very small. The lens system has a high angular resolution. (b) Small lens. The size of the Airy disk is the same as in (a). However, due to the short focal length f_2, here the angular projection of the Airy disk in the object space $\Delta\varphi_2$ is very large. The lens system has a low angular resolution. (c) The number of information in the image plane of a large lens is very large, because of the small Airy disk and large focal length resulting in a large image field. (d) Even if the size of the image points is the same, the spatial information capacity of the small lens is low because of the small image field. Only few image points can be separated. (e) By applying an array of microlenses (d), which separately transfer the information in parallel, the same information capacity as with the bulk lens in (c) can be achieved.

curved basis. For technical derivates on planar substrates, a larger collective space bandwidth product than that of the single channel can be achieved by decentered telescopes, which represents the basis of the cluster eye described in Chapter 5. Adding a channel-dependent beam deflection to the microlenses of a single MLA layer results in the same effect. Inhomogeneous MLAs are required as will be proposed later in Chapter 4. If each channel views exactly the same information, the MLAs information capacity equals that of the single channel. Then, in terms of information capacity, no improvement is achieved by using an array instead of a

single microlens. However, as will be shown in the main part of Chapter 4, advantages in terms of compactness, integration with the optoelectronics, simplicity of information processing and, maybe most important, ability of using a coarse photo sensitive pixel structure, also can be exploited for this condition.

Conclusion. In microoptics, aberrations are not as critical as in bulk optics. For small scale lens systems, the diffraction limit itself is the important criteria describing resolution and image finesse. This limitation can be avoided by using MLAs and parallel information transfer instead of single microlenses.

2.3.2 Sensitivity

Besides resolution, the sensitivity – the light gathering capability – is another important property of imaging systems. Sensitivity might even have the higher priority in the case of weak ambient illumination. If there are not enough photons captured to excel photon noise, even the best resolution does not gain information. Natural vision systems proof this trade-off [28].

How does the sensitivity of an imaging system change when scaling the size? This depends on several different factors: Is the object-scene composed of separated point sources or built up by illuminated extended objects? Shall – besides diffraction limitation – the geometrical angular resolution be obtained during scaling? Or shall the size of the photo sensitive pixels be kept constant? All these different cases are discussed in the following.

Point source. The solid angle Ω subtended by a curve surrounding the area A_c on a spherical surface with radius c centered on a light emitting point in space is defined as [35]

$$\Omega = \frac{A_c}{c^2}. \tag{2.22}$$

For a circular curve with diameter D, for instance a lens aperture, it follows

$$\Omega = \pi \frac{D^2}{4c^2}. \tag{2.23}$$

Let the source point have a flux P_S which is emitted into the full solid angle 4π. Then the flux of electromagnetic radiation P_D received by the surface with diameter D at the distance c and focused in the image plane as P_I is

$$P_I = P_D \tau = \tau P_S \frac{\Omega}{4\pi} = \tau P_S \frac{D^2}{(4c)^2}, \tag{2.24}$$

where τ is the transmission of the optical system. This equation is well known from the photometric distance law. For a given object distance, the ratio of flux in the image plane and the object plane – let this be called efficiency of the optical system – is only a function of the contributing lens area. This is especially critical for the imaging of point sources, because the flux in the image plane can not be increased for a given D/c, no matter how the magnification of the optical system is set. A microlens can not image a far distant point source while delivering a detectable amount of flux.

Extended source. This behavior is completely different for the imaging of extended objects. Let us assume an extended object of area A_O and radiance L_O. If the object-scene is a perfect Lambertian radiator, L_O is constant over the hemispherical solid angle, and it follows that $I_O = \pi L_O$, with I_O being the irradiance in the object surface [27]. Furthermore, $c \gg D$ is assumed. Then $D/(2c) = \tan u \approx \sin u$ is obtained, where u is the half angle of the considered object side solid cone. Consequently, by using Eq. (2.23),

$$P_D = A_O I_O \sin^2 u \tag{2.25}$$

can be derived. The flux in the lens aperture is proportional to the square of the object side solid cone. This flux is directed to the image of size A_I in the image plane of the lens, multiplied by τ. The irradiance in the image plane is consequently

$$I_I = P_D \tau / A_I = \tau \frac{A_O}{A_I} I_O \sin^2 u = \tau I_O \frac{\sin^2 u}{m^2}, \tag{2.26}$$

with $m = \sqrt{A_I/A_O}$ being the transverse magnification of the imaging system. Finally, by substituting Abbes sine condition $\sin u / \sin u' = m$ (u' is the image side solid cone half angle) we obtain

$$I_I = \tau I_O \sin^2 u' = \tau I_O \, \text{NA}^2 = \tau I_O \frac{1}{4(F/\#)^2}. \tag{2.27}$$

The irradiance in the image plane of an objective for a distant, extended object is proportional to the square of image side solid cone. The image irradiance is determined only by the system's $F/\#$ [27, 29, 170]. A microlens can image a far distant, extended object with exactly the same sensitivity as a bulk lens for the same receptor size. In order to calculate the total flux P_I which a receptor receives, the area of a single photo sensitive (square) pixel d^2 has to be taken into account:

$$P_I = \tau I_O \frac{d^2}{4(F/\#)^2}. \tag{2.28}$$

Two objectives with the same $F/\#$ and pixel size d, for the same scene, will consequently produce the same signal, no matter what difference in size they have.

Figures 2.8 (a) and (b) display the two cases. For this discussion, the photo sensitive pixel size is set $d = d_{F_1} = d_{F_2}$. Because of the much shorter focal length f_2 with respect to f_1, the angular projection of a pixel in the object space $\Delta\varphi_2$ is much larger for the miniaturized lens than for the bulk lens (where f_1 results in $\Delta\varphi_1$). The pixels' FOVs overlap much stronger in object space for the small lens, allowing a larger area of the illuminated object to contribute to one image pixel. This compensates for the reduced lens aperture D_2. The flux in the photo sensitive pixels is the same for small and large lenses. The resolution is however decreased. If the geometrical resolution shall be maintained, the pixel size must decrease. This results in a reduced flux on a pixel, because the $F/\#$ and thus the irradiance in the image plane are constant.

Only by decreasing $F/\#$, the sensitivity and resolution can be maintained at the same time during miniaturization. But following Eq. (2.18), e.g. spherical aberrations will increase.

Natural field darkening. Equation (2.27) applies to the calculation of the irradiance I_I for imaging a small object on the system's optical axis. For oblique imaging under the field angle ω, a reduced irradiance $I_I(\omega)$ results in the objective's image plane [27]

$$I_I(\omega) = I_I \cos^4 \omega. \tag{2.29}$$

This "natural" field darkening effect – the loss of image irradiance at the edge of the image plane – is also known as the $\cos^4$-law of illumination. It is caused by the increase of object distance which is entering to the square power following Eq. (2.24) ($\Rightarrow \cos^2 \omega$), by decrease of the projected lens aperture ($\Rightarrow \cos \omega$) and by the increased receiving surface ($\Rightarrow \cos \omega$). Vignetting – the angle dependent blocking of rays through the entrance pupil by lens apertures – causes a further reduction of $I_I(\omega)$ with increasing ω.

Conclusion. Scaling down an imaging system with constant $F/\#$ results in a constant flux on the photo sensitive pixels. But this is reducing resolution. A broader part of the object contributes to one image pixel. The size of the photo sensitive pixels must be decreased in order to maintain resolution during scaling. Then, for constant $F/\#$, constant irradiance in the image plane means smaller flux. Only by additionally decreasing of $F/\#$ when miniaturizing an imaging system, resolution and flux can be maintained.

2.4 3x3 Matrices for Paraxial Representation of MLAs

A paraxial model is introduced which allows the design of the cluster eye in Chapter 5.

2x2 matrices are well known for the paraxial description of many optical systems [171–173]. An input vector including the paraxial input ray height h_{in} and the paraxial input ray angle α_{in} is transformed to an output vector including the paraxial output ray height h_{out} and the paraxial output ray angle α_{out} using

$$\begin{pmatrix} h_{out} \\ \alpha_{out} \end{pmatrix} = \tilde{M} \cdot \begin{pmatrix} h_{in} \\ \alpha_{in} \end{pmatrix}. \tag{2.30}$$

$\tilde{M}$ is the paraxial transfer matrix of the optical system. For the propagation of a distance Δz, $\tilde{M}$ would appear in the form of Eq. (2.31), and for refraction by a lens with focal length f in the form of Eq. (2.32).

$$\tilde{M}_{prop(\Delta z)} = \begin{pmatrix} 1 & \Delta z \\ 0 & 1 \end{pmatrix}, \tag{2.31}$$

$$\tilde{M}_{refr(f)} = \begin{pmatrix} 1 & 0 \\ -1/f & 1 \end{pmatrix}. \tag{2.32}$$

The combination of different elements on the optical axis (e.g. lenses, free space...) is calculated by multiplying the corresponding matrices in the right order. The resulting 2x2 matrix corresponds to the overall optical system's transmission function.

For a finite object distance, the matrix elements or ratios of them are in fact significant for instance as an image forming condition or for the magnification [171,174]. The matrix elements can even be used for free space propagation under consideration of diffraction effects [175].

Arrays of optical elements can be treated as a special case of misaligned optical elements. One way to paraxially describe misaligned optical elements consists in the 2x2 misalignment matrix [173,176]. Here the misalignments enter the calculations via a vector which contains the tilt and decentration. The ray transfer matrix becomes a 4x4 matrix which implicitly contains spatial shifts and deflections of the ray which arise from misalignments.

Another possibility is just to add simple vectors which introduce a coordinate shift and tilt at the right position in the 2x2 matrix formalism. However, the overall optical system can not any longer be described by a multiplication of 2x2 matrices of the axially sequenced components. The 2x1 vectors of ray height and tilt have to be summed up step by step, from surface to surface.

A much more convenient way is the 3x3 matrix formalism which explicitly contains the misalignments in $\tilde{M}$ [172,177]. Here a third component which is always unity is added to the ray vector, and a 3x3 matrix in the form of

$$
\begin{pmatrix} h_{out} \\ \alpha_{out} \\ 1 \end{pmatrix} = \begin{pmatrix} M_{11} & M_{12} & \Delta x \\ M_{21} & M_{22} & \Delta\beta \\ 0 & 0 & 1 \end{pmatrix} \cdot \begin{pmatrix} h_{in} \\ \alpha_{in} \\ 1 \end{pmatrix}
\tag{2.33}
$$

is used. The matrix elements M_{11}, M_{12}, M_{21} and M_{22} are those of the well known on-axis 2x2 matrix formalism while the matrix elements Δx and $\Delta\beta$ represent a decentration or tilt, respectively.

This formalism is used exemplarily to trace a paraxial ray through an off-axis thin lens. First, the ray is transformed to the local coordinate system of the laterally shifted lens (lateral shift σ). Then, the ray is traced through the lens, and finally it is transformed back to the global coordinate system. The complete matrix of the off-axis thin lens is then given by

$$
\begin{pmatrix} 1 & 0 & 0 \\ -1/f & 1 & \sigma/f \\ 0 & 0 & 1 \end{pmatrix} = \begin{pmatrix} 1 & 0 & \sigma \\ 0 & 1 & 0 \\ 0 & 0 & 1 \end{pmatrix} \cdot \begin{pmatrix} 1 & 0 & 0 \\ -1/f & 1 & 0 \\ 0 & 0 & 1 \end{pmatrix} \cdot \begin{pmatrix} 1 & 0 & -\sigma \\ 0 & 1 & 0 \\ 0 & 0 & 1 \end{pmatrix}.
\tag{2.34}
$$

From Eq. (2.34), it can be derived that a laterally shifted lens adds a tilt σ/f to the paraxial ray. Because it will be required in Chapter 5, Eq. (2.35) for completeness shows the 3x3 matrix for paraxial propagation of the distance Δz in a medium with refractive index n

$$
\begin{pmatrix} 1 & \Delta z/n & 0 \\ 0 & 1 & 0 \\ 0 & 0 & 1 \end{pmatrix}.
\tag{2.35}
$$

Using this formalism, in Chapter 5 the paraxial optical system matrices of complex arrangements of MLAs as for instance in a Gabor superlens will be calculated.

Conclusion of the fundamentals.   It has been shown that the type of eye evolved by a creature is, besides the size of the animal, a function of its natural living habitat [9] and thus a question of available illumination, required resolution and time for image acquisition. Table 2.1 displays an exemplary overview of parameters of the major natural imaging principles. It is not surprising

Table 2.1. Optical parameters of a selection of refractive animal eyes calculated and composed from geometrical parameters found in the various literature [1, 28, 34]. Eye radius R_{EYE} of the bee assumed to be 1.5mm. For the moth eye, the effective aperture diameter resulting from the contribution of a large number of channels is given. The diameter of the microlenses is 20μm. For man, moth and jumping spider, the interreceptor angle is used for the calculation of the eye parameter since there is no interommatidial angle.

Parameter	Man	Bee	Moth	Jumping Spider
Comment	At fovea	Worker bee	Type: Ephestia	Type: Phidippus
Eye type	single	apposition	superposition	principal
Light habitat	diurnal	diurnal	nocturnal	diurnal
Lens diameter (mm)	7	0.025	0.4	0.36
Focal length (mm)	23	0.06	0.17	0.77
Receptor diameter (μm)	2	1.5	8	2
$F/\#$	3.3	2.4	0.4	2.1
Sensitivity (μm$^2 = 10^{-12}$W/(W/m^2))	0.23	0.24	218	0.5
Acceptance angle (°)	0.007	1.9	<13	0.17
Interreceptor angle d/f (°)	0.005	-	3	0.15
Interommatidial angle (°)	-	0.95	-	-
Resolution (LP/°)	100	0.52	>0.08	3-6
Eye parameter (μm)	0.61	0.41	20.9	0.94

that compound eyes can exhibit sensitivities similar to those of single aperture eyes. Further it was demonstrated in this chapter that sensitivity is independent of eye-size. However, as Tab. 2.1 also reveals, the resolution of small (compound) eyes is lower by order of magnitudes than that of macroscopic single aperture eyes. The main advantages of compound eyes are the small required volume and the large FOV. For high resolution vision, compound eyes are not well suited since they would need to be even larger than the equivalent single aperture eye with the same resolution. The introduced principles of natural compound eyes and the scaling laws of imaging systems build the basis of the development of the artificial apposition compound eye objective in Chapter 4 and of the cluster eye in Chapter 5.

3 Anamorphic Microlenses for Aberration Correction under Oblique Incidence

In the following, design considerations for anamorphic microlenses for the correction of astigmatism and field curvature based on Gullstrand's equations [178, 179] are presented. Furthermore, the suitability of ellipsoidal microlenses fabricated by a reflow process for this purpose is shown. The definition of the lens shape by its rim is demonstrated. The improvement of image quality under oblique incidence by using ellipsoidal microlenses designed for the specific viewing direction is verified by simulation and experiment.

As the result of their curvature, compound eyes possess a very large FOV. Each optical channel, however, focuses light only onto a photo receptor if the light comes from object points situated on the channel's optical axis. Since each channel is used under normal incidence, off-axis aberrations such as astigmatism, field curvature, coma and distortion as well as field darkening do not occur. All such effects would otherwise decrease the angular resolution and the sensitivity with increasing FOV.

Artificial compound eyes, as will be discussed in Chapters 4 and 5 are limited to planar substrates since today's microelectronics fabrication technology is restricted to planar artificial receptor arrays such as CMOS or CCD sensors. The same holds for standard microoptics technologies [169, 180–183]. Consequently, the optical channels can not be arranged in on-axis configurations, which is inherently connected with the appearance of off-axis aberrations when using spherical microlenses. In classical macroscopic optical systems, where one optical channel transfers the overall FOV, a large number of optical elements has to be used in order to minimize off-axis aberrations. This leads to complex, bulk, and expensive optical systems.

In contrast, for artificial compound eyes, each channel is assigned only to one major viewing direction within the overall FOV. Consequently, an individual correction of the channels for aberrations is feasible [184, 185].

As the result of the small NA of the microlenses of the objective, astigmatism and field curvature are by far dominant as compared to coma. Therefore, efficient channelwise focusing of the beam under oblique incidence is possible by using differently shaped and oriented anamorphic microlenses for each channel [186]. The radii of curvature of the microlenses in perpendicular directions have to be different in a certain manner in order to compensate for astigmatism. Furthermore, both radii are chosen in such a way that the focal plane of all channels with their different AOI is fixed at the position of the paraxial image plane. This leads to a planarized image in the detector surface.

A torus segment having two radii of curvature in perpendicular directions is the most appropriate surface type for such an anamorphic lens.

The fabrication of MLAs by melting of photo resist is a well established technology yielding very smooth and well determined spherical surfaces [187–192]. This process also found applica-

tion in the fabrication of imaging systems [147]. Here the surface shape is the result of surface tension effects and depends on the volume of the resist cylinder and the shape of the rim of the microlens (Subsequent reactive ion etching steps enable to manufacture aspherical MLAs.). Consequently stringent limitations to viable geometries apply. A suitable approximation of the desired torus segment is an ellipsoidal microlens which can be easily formed by melting a photo resist cylinder on an ellipsoidal base [148, 193–195]. Alternatively, pedestals underneath the resist cylinders defining the rim of the microlens allow one more degree of freedom. Here, the resist volume is no longer fixed by the desired rim of the microlens and the resist cylinder height [196].

3.1 Gullstrand's Equations of the Oblique Focal Length

When using (low-NA) spherical lenses under oblique incidence, third order aberration of astigmatism and field curvature will occur (Fig. 3.1). Rays propagating in the tangential plane of the lens will experience higher optical power compared to rays which propagate in the sagittal plane. Consequently, different focal planes for tangential and sagittal rays exist, where the spots are blurred to lines. The difference in optical powers and, therefore, in axial position of the focal planes for the tangential and sagittal rays increases with increasing chief ray angle. The circle of least confusion, representing the minimum spot size between the tangential and sagittal focal lines, is moving on a spherical surface (Petzval sphere) with changing AOI. This effect is called field curvature and results in strongly defocused bundles in the Gaussian image plane.

For calculating the tangential and sagittal back focal lengths s_t' and s_s' of a spherical surface, the Gullstrand's equations [178, 179] are employed. Herein Δ denotes Picht's operator being the difference between object and image space variables. In this notation Snell's law is written in the form

$$\Delta(n \sin \epsilon) = (n \sin \epsilon) - (n' \sin \epsilon') = 0. \tag{3.1}$$

ϵ and ϵ' are the chief ray angles in object and image space, respectively, measured with respect to the optical axis. n and n' are the corresponding refractive indices on the two sides of the refracting surface. The Gullstrand's equations (3.2, 3.3) describe astigmatism and field curvature as a function of the chief ray angle and apply to small ray bundles passing trough a spherical surface with a radius of curvature R

$$\Delta\left(\frac{n}{s_t'} \cos^2 \epsilon\right) = \frac{1}{R} \Delta(n \cos \epsilon), \tag{3.2}$$

$$\Delta\left(\frac{n}{s_s'}\right) = \frac{1}{R} \Delta(n \cos \epsilon). \tag{3.3}$$

For large object distances with respect to the paraxial focal length s_0', the influence of object distance on s_0' is negligible and the equations simplify. Since s_t' and s_s' are measured along the direction of the chief ray, their projection onto the optical axis has to be taken into account to
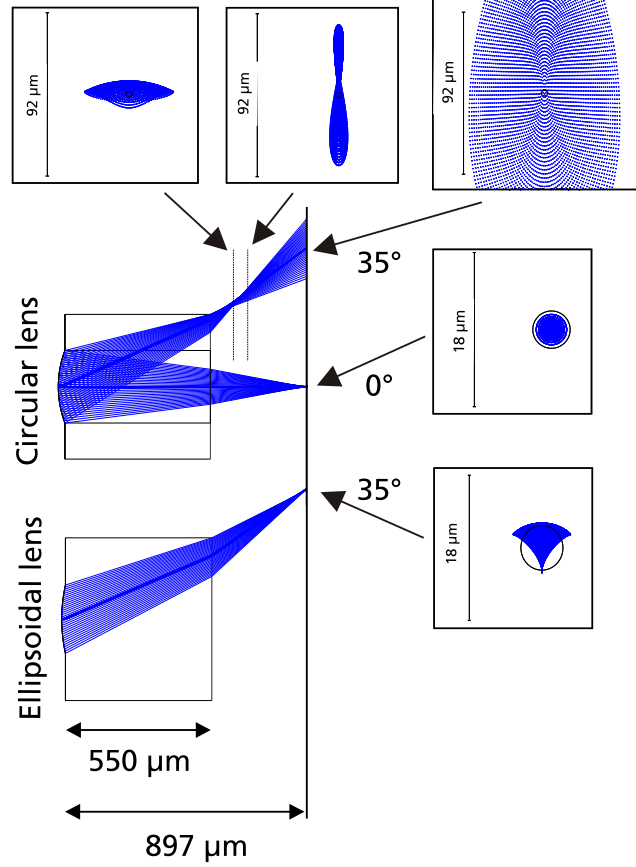
Figure 3.1. Circular microlens and ellipsoidal microlens under perpendicular and oblique incidence and related spot diagrams. A circular microlens with $R = 339\mu$m and $D = 242.8\mu$m in fused silica ($n' = 1.46$ at $\lambda = 550$nm) under perpendicular incidence produces a diffraction limited focus. However, if illuminated under oblique incidence, astigmatism and especially field curvature lead to very large spots in the Gaussian image plane. The tangential and sagittal image planes are separated from the Gaussian image plane (here -165μm and -262μm, respectively) and the foci are blurred to lines. Using an anamorphic microlens with adapted tangential and sagittal radii of curvature ($R_t = 579\mu$m, $R_s = 451\mu$m) for this special AOI a diffraction limited spot size is achieved.

find the position of the corresponding image planes and their distances to the Gaussian image plane. The distance to the Gaussian image plane is determined by s'_0 in the paraxial case.

Astigmatism is eliminated for one AOI if the back focal lengths for tangential and sagittal rays coincide for this angle. By furthermore requiring

$$s'_t = s'_s = \frac{s'_0}{\cos \epsilon'},\tag{3.4}$$

the tangential and sagittal image planes are fixed at the position of the Gaussian image plane. For the compound eye imaging systems, planarized images result (Fig. 3.1).

Inserting the Gullstrand's equations (3.2, 3.3) into Eq. (3.4) the tangential and sagittal radii of curvature of the lens for correction of astigmatism and field curvature are calculated as

a function of the chief ray angle to

$$R_t(\epsilon) = s_0' \left(\frac{n' \cos \epsilon' - n \cos \epsilon}{n' \cos^3 \epsilon'} \right) \tag{3.5}$$

$$R_s(\epsilon) = s_0' \left(1 - \frac{n \cos \epsilon}{n' \cos \epsilon'} \right). \tag{3.6}$$

Here infinite distant objects are assumed.

In Fig. 3.2 plots of the calculated optimum tangential and sagittal radii of curvature as a function of the chief ray angle are given for a spherical surface with a paraxial focal length of 2.1mm focusing from air into fused silica. For validation of these results, a surface with two different radii of curvature in tangential and sagittal direction (Biconic surface model) was optimized for minimum spot radius for the same AOI in the raytracing software ZEMAX$^{\text{TM}}$. The obtained radii are marked as points in Fig. 3.2. Only for large chief ray angles devia-
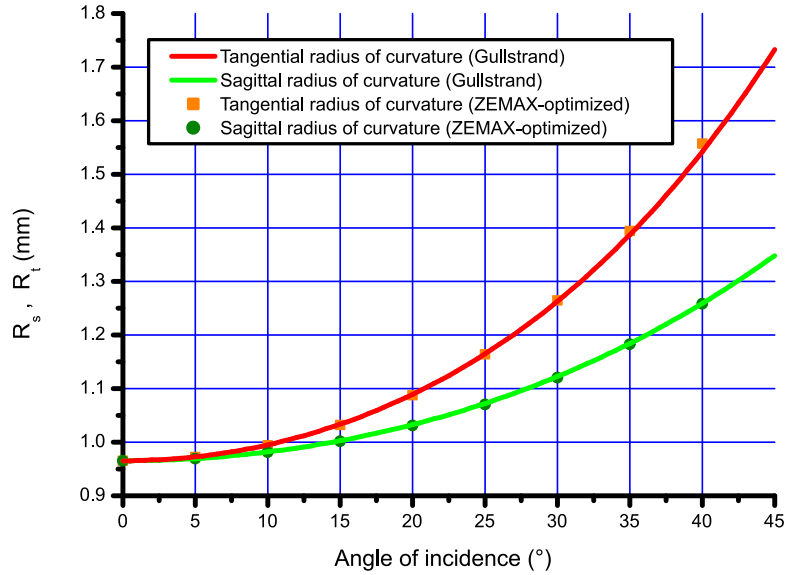

Figure 3.2. Optimum tangential and sagittal radii of curvature under oblique incidence calculated by Gullstrand's equations (lines) and using raytracing optimization (points); paraxial focal length is 2.1mm, NA is 0.187.

tions between optimized and analytic values can be observed. The analytical model based on Gullstrand's equations is consequently verified by the simulation.

3.2 Ellipsoidal Microlenses by Melting of Photo Resist

Because of its superior capability of producing high quality microlenses [197, 198] at moderate expense, melting of photo resist is the most appropriate fabrication technology for the proposed anamorphic microlenses [148, 187, 188, 194, 195]. Ellipsoidal microlenses are shown in Appendix A to be an attractive type of anamorphic microlenses. They reveal two separate paraxial radii of curvature and the ability of being produced by melting technology if the rim of the resist cylinder has an ellipsoidal shape [193].

For the generation of the ellipsoidal microlenses by exposure through photo lithographic masks and subsequent reflow, the connection of the tangential and the sagittal radii of curvature, resist cylinder height and the geometry of the ellipsoidal base is of fundamental knowledge. From simple geometrical considerations on a circle follows

$$R = \frac{h_L}{2} + \frac{r^2}{2h_L}. \tag{3.7}$$

Here, r is the radius of the circular lens and h_L the lens height. As shown in Appendix A, h_L is constant within the used parameter space and with a sufficient accuracy, for a given resist cylinder height before melting, independently of the size of the microlens-base. The relationship between the major radii of curvature of the ellipsoidal microlens R_t and R_s and the major and the minor half-axes of the ellipsoidal lens-base a_t and a_s becomes especially simple [193]

$$\frac{R}{r^2} = \frac{R_t}{a_t^2} = \frac{R_s}{a_s^2}. \tag{3.8}$$

Herein h_L is assumed to be small with respect to a_t and a_s. The major radii of curvature of the anamorphic microlens, fabricated by the reflow process, can, within a sufficient accuracy, simply be tuned by the size of the ellipsoidal lens-base and consequently by the photo lithographic mask dimensions using Eq. (3.8).

3.3 Spot Size Determination Under Oblique Incidence

For implementation into an artificial compound eye microoptical sensor, ellipsoidal microlenses have been optimized and fabricated for an AOI of 35° [199]. A spherical microlens with the same paraxial focal length of 750.8μm was fabricated for comparison. Measurements of the spots when illuminating the microlenses under different AOI were carried out using a setup as drawn in Fig. 3.3. Figures 3.4 (a) and (b) illustrate the influence of astigmatism and field curvature as the result of oblique incidence on a spherical surface. Blurred spots which are connected to poor optical performance result. Good aberration correction using an adapted ellipsoidal microlens is demonstrated in Fig. 3.4 (c) and (d). Diffraction limited spot sizes are achieved. For comparison, the experimentally obtained foci in the tangential, sagittal and plane of least confusion of the circular microlens under oblique incidence are presented in Fig. 3.5. The focus of the used ellipsoidal microlens under perpendicular incidence is shown as well. Strong astigmatism can be observed. Even the circles of least confusion have a considerably increased spot size compared to the optimized case in Fig. 3.4.

The explicit influence of the focus size on the image quality is demonstrated in Fig. 3.6. Here the resolution test target USAF 1951 [17] is imaged under perpendicular and strongly oblique incidence. The circular and ellipsoidal microlenses are fabricated by the same resist height. While the circular microlens provides a sharp image of the test pattern under perpendicular incidence, the ellipsoidal microlens does the same for an AOI of 30°.
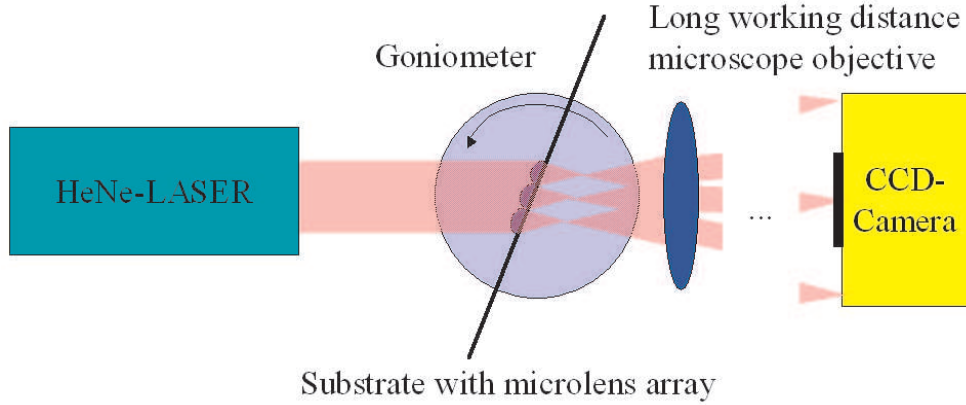
Figure 3.3. Experimental setup for focus evaluation under oblique incidence. Rotation axis is aligned with vertex of microlens under test. Resolution of the measurement was determined by imaging Ronchi rulings to 0.18μm/pixel on the CCD.
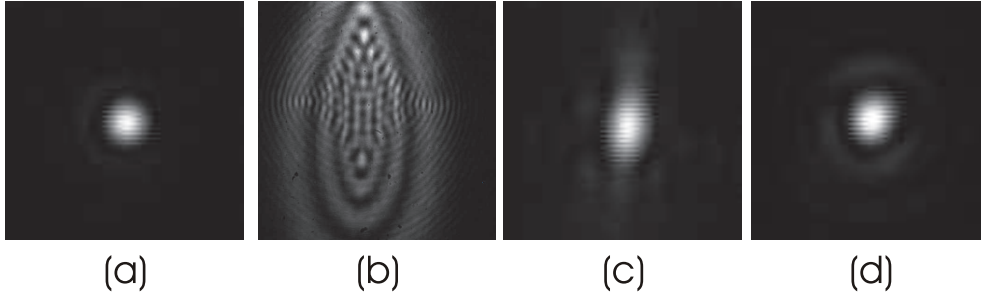

Figure 3.4. Experimentally obtained spots. (a) Circular microlens under $0°$ (design angle), window width is 18μm, $1/e^2$-width is 4.3μm. (b) Circular microlens under $35°$, window width is 92μm. The image plane is the same as in (a). (c) Ellipsoidal microlens under $35°$ (design angle), window width is 18μm, ratio of peak intensity compared to (a) is 0.73. The image plane is the same as in (a). (d) Ellipsoidal microlens under $32°$ (best angle), window width is 18μm, ratio of peak intensity compared to (a) is 1.04. The image plane is moved 80μm away from microlens compared to (a). Ellipsoidal microlens was optimized for $35°$ AOI. Design: $R_t = 485.7\mu$m, $R_s = 609.6\mu$m, $a_t = 138.9\mu$m, $a_s = 155.6\mu$m. Measured after reactive ion etching (RIE): $R_t = 451\mu$m, $R_s = 579\mu$m, deviation from sphere: 84nm (RMS – root mean square). Circular microlens parameters: Design: $R = 375.2\mu$m, $2r = 242.8\mu$m. Measured: $R = 339\mu$m, deviation from sphere: 30nm (RMS).

Conclusion. The use of ellipsoidal microlenses fabricated by reflow of photo resist has been shown to be an efficient method for channelwise correction of astigmatism and field curvature. This method will be exploited to provide a homogeneous resolution over a large FOV for artificial compound eye imaging applications later in this thesis. The effect of the $\cos^4$-law, discussed in Section 2.3, is mitigated because the microlens aperture is increased in the direction of increasing AOI. The projected aperture can be kept constantly circular.

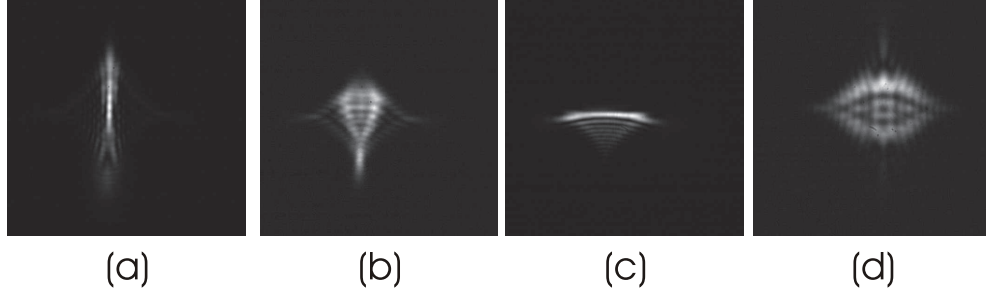**Figure 3.5.** Experimentally obtained spots. Window width is 92μm for all images: (a) Circular microlens under 35°, 170μm axial distance from paraxial focus towards the microlens = tangential image plane. (b) Circular microlens under 35°, 240μm axial distance from paraxial focus towards the microlens = circle of least confusion. (c) Circular microlens under 35°, 300μm axial distance from paraxial focus towards the microlens = sagittal image plane. (d) Ellipsoidal microlens under 0°, 380μm axial distance from paraxial focus of the microlens = circle of least confusion.
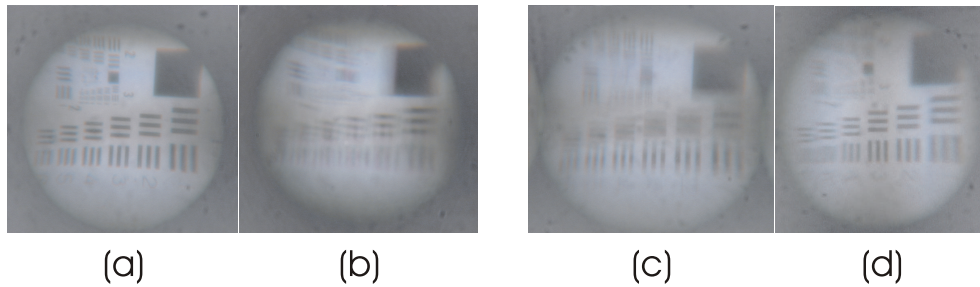

Figure 3.6. USAF 1951 bar test pattern imaged by circular ($r = 125\mu$m) and ellipsoidal ($a_t = 134.5\mu$m, $a_s = 144.5\mu$m) microlenses under perpendicular and oblique incidence. (a) Circular microlens, 0°. (b) Circular microlens, 30°. (c) Ellipsoidal microlens, 0°. (d) Ellipsoidal microlens, 30°.

4 Artificial Apposition Compound Eye Objective (APCO)

In this chapter, novel APCOs with thicknesses far below 0.5mm are presented, exploring microoptical design principles and fabrication technologies (patent approved [200] and patent pending [201]). The operational principle is revealed in Section 4.1, followed by a provision of general design issues and by scaling laws of artificial apposition compound eye imaging systems in Section 4.2. The theoretical limitations of resolution and sensitivity are demonstrated. In Section 4.3 the fabrication of different types of APCOs is covered. They are characterized with respect to optical parameters such as FOV, sensitivity and resolution in Section 4.4.

A monolithic APCO without opaque walls between the channels (Fig. 4.1 (a)) is fabricated by microoptics technology [199, 202, 203]. The APCO is adopted and attached to a CMOS sensor array which is capable of on-chip analog image processing [204]. This results in a thin camera system [205–207]. Captured images are presented. Opaque walls are introduced between
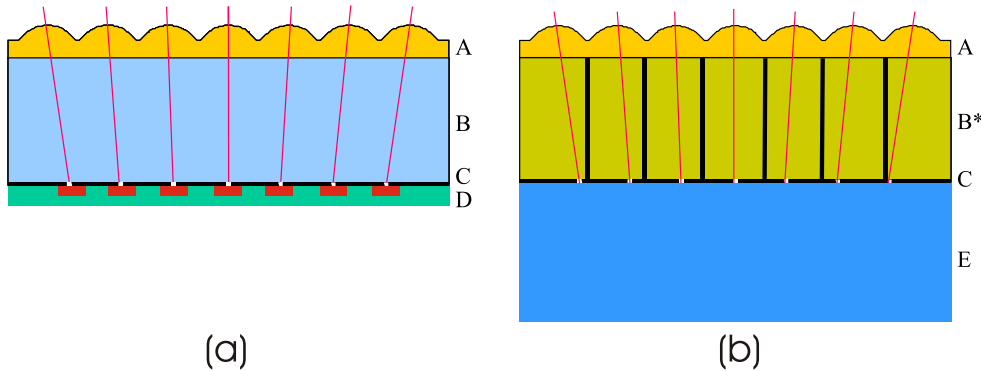

Figure 4.1. Schematic side view of the two realized artificial apposition compound eye imaging systems. (a) Objective without opaque walls between channels attached to CMOS sensor array. A: Replicated MLA, B: Thin glass substrate, C: Metal layer with pinhole array, D: CMOS sensor array. (b) Objective with opaque walls between channels for prevention of cross talk. A: Replicated MLA, B*: High aspect ratio photo polymer with included opaque walls, C: Metal layer with pinhole array, E: Thick supporting substrate.

channels (Fig. 4.1 (b)) to avoid ghost images resulting from cross talk. Technological aspects are discussed, and the effect of opaque walls on cross talk and extension of the FOV is analyzed experimentally [207].

4.1 Principle – MLA with Assigned Array of Photo Receptors

Artificial receptor arrays such as CCD- or CMOS sensors are fabricated on planar wafers. Thus, a thin monolithic objective based on the APCO concept has to be a planar structure as well.

The proposed imaging optical sensor consists of an MLA positioned on a substrate, preferably with optical isolation of the channels, and an optoelectronic detector array of different

pitch in the microlenses' focal plane. The pitch difference enables different viewing directions of each optical channel. Each channel's optical axis points into a different direction of object space with the optical axes of the channels directed outwards (Fig. 4.2) if the pitch of the receptor array is smaller than that of the MLA. Consequently, an upright image results. If the pitch of the MLA is smaller than that of the receptor array, there follows an inverted image. A pinhole array can be used to narrow the photo sensitive area of the detector pixels if they are not small enough for the required resolution.

A planar APCO as shown in Fig. 4.2 is described by the same optical parameters as its curved natural archetype. Behind each microlens a small image of the object is generated. As the result of the pitch difference between MLA and pinhole array, $\Delta p = p_L - p_P$, a moiré-magnified image [208] is obtained when the pinholes with different amounts of offsets with respect to the microlenses sample the micro-images [209]. Each channel corresponds to one field angle in object space. The angular distance $\Delta\Phi$ between the ommatidia's visual axes determines the sensor's Nyquist frequency [17] and is called interommatidial angle. The acceptance angle of an ommatidium $\Delta\varphi$ is given by the ratio d/f and diffraction effects of the microlens apertures defined by λ/D. $\Delta\varphi$ determines the modulation for a given object spatial frequency (assuming $2\Delta\Phi \gg \Delta\varphi$) or even determines the resolution cut-off (if $2\Delta\Phi \leq \Delta\varphi$) (following the Sparrow criterion [5]). The acceptance angle $\Delta\varphi$ determines the trade-off between sensitivity and resolution. It has to be small in order to have a high resolution and large in order to achieve a high sensitivity. As in the natural equivalent, opaque walls are introduced
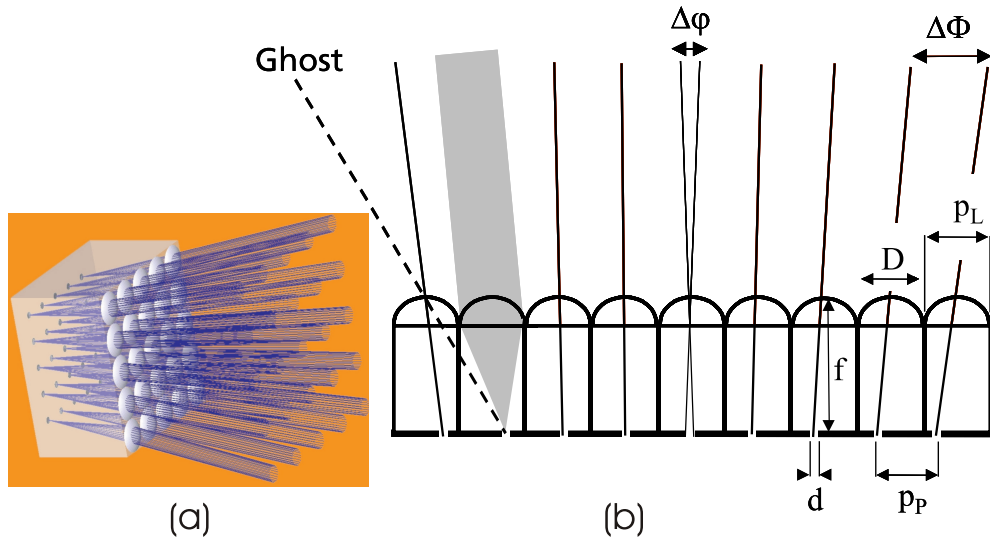

Figure 4.2. Schematic diagram of a planar APCO. (a) 3D model of the APCO showing the focusing MLA, the pinhole array in its focal plane and the tilted optical axes of ommatidia because of a pitch difference between microlens- and pinhole array, enabling the FOV of the imaging system. (b) The thin monolithic device is composed of an array of microlenses with diameter D, focal length f and pitch p_L on the front side of a spacing structure and a pinhole array with pinhole diameters d and pitch p_P in the microlenses' focal plane on the spacing structure's backside.

between ommatidia preventing cross talk of adjacent channels for object points outside the FOV and resulting ghost images (oblique ray in Fig. 4.2 (b) demonstrates the ghost effect).

The overall image size of the APCO is determined by the channel size multiplied with the channel number and thus completely independent of the system length. This arrangement delivers an image with a much larger magnification than that of a single microlens. But it has a much shorter system length than a classical objective with the same magnification. The equivalent focal length of the APCO (which is defined by the ratio of lateral sensor extension and FOV), determining the magnification is thus much larger than the overall objective length. This results in a huge telephoto ratio (ratio of focal length to system length) of > 100 which in conventional telephoto objectives is approximately 2-3 only.

A further advantage of the APCO is the large focal depth. As a result of the extremely short focal length of the microlenses an object is focused independently of the object distance. There is no need for an active focus adjustment with respect to object distance.

The low fill factor and large pitch of pinholes in the image plane makes the APCO suitable for optoelectronic sensor arrays which also have low fill factor. A combination with conventional densely packed optoelectronic CCD- or CMOS sensor arrays is not reasonable because only few pixels would be actually exploited.

The simple model of angular FOV only applies to the case of large object distances compared to the lateral extension of the APCO. But this is the case for standard "objective" applications examined at this point.

4.2 Design and Simulation of APCO

In the following, design considerations for an ultra-thin monolithic vision system based on artificial compound eyes are presented. There are two main possibilities of characterization. The first is the examination of the complete array of channels. Here, the interaction of channels, to provide one overall moiré-magnified image can be observed. But there is only a limited number of analysis tools available. However, the image forming capability of the APCO can be proved this way. Much more information about the APCO can be obtained by analyzing the performance of the single ommatidium. Many valuable tools for the optical design and analysis are available. The extrapolation from a single ommatidium to an array of channels forming the final APCO has to be harmonized with the single channel parameters, but is otherwise comparatively simple. A comprehensive discussion of multi-channel and single-channel simulation methods of the APCO is provided in Appendix B. In the following, only the most important method – the determination of the angular sensitivity function (ASF) – is introduced.

4.2.1 Angular Sensitivity Function

The ASF is the most appropriate method to characterize the performance of a single ommatidium. It predicts which solid angle in object space is treated by the optical system as one image

point. The amount of flux, radiated from an object point which is actually received by a photo receptor, is plotted as a function of angular distance of the object point from the optical axis of the considered ommatidium. The exact representation is the convolution of the microlens PSF with the pinhole, projected into object space by the focal length of the microlens. The field dependent ASF, explicitly includes diffraction, aberrations and pinhole size. It is obtained by using commercially available raytracing software.

First, the microlens PSF including aberration effects and diffraction at the microlens aperture is calculated for a certain field angle. It is then multiplied by the transmission function of the pinhole. The angular offset of the considered field angle from the ommatidium's viewing direction determines, how much power of the PSF is transmitted by the pinhole (Fig. 4.3 (b)). This procedure is repeated for different amounts of offsets of the field angle from the
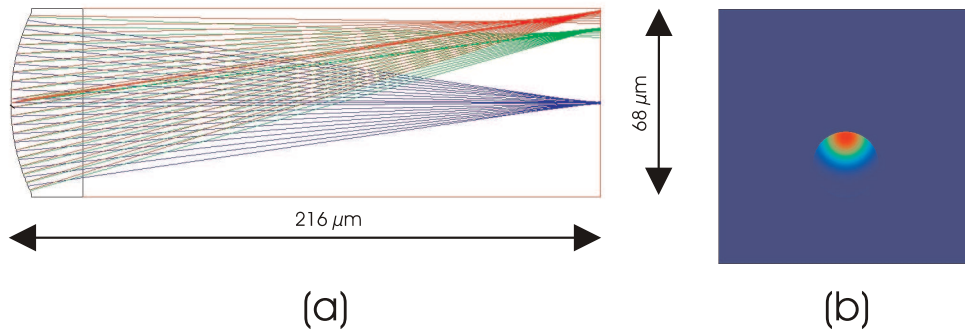

Figure 4.3. Simulation of a single channel for determination of the ASF. (a) Diagonal cross section of single ommatidium. Length is 216μm, $R = 75\mu$m, microlens in UV-curing polymer on glass substrate. Field angles $0°$, $11°$, $13.5°$ are shown. (b) In the focal plane a pinhole of $d = 2\mu$m is centered on the microlenses optical axis. A plane wave incident at $0.35°$ angular offset from the optical axis results in an offset PSF on the pinhole. Consequently a reduced power is coupled, compared to on-axis illumination. Simulation method: "Physical optics propagation" in ZEMAX$^{\text{TM}}$.

ommatidium's viewing direction. The coupled optical power is plotted as a function of the offset.

Figures 4.4 and 4.5 show simulations of the ASF of two different systems, where the efficiency is normalized to the flux incident on the lens at $\lambda = 0.55\mu$m. The APCO-principle shows a clear trade-off between sensitivity and resolution: The larger the pinhole diameter, the larger the sensitivity but the wider the ASF resulting in lower resolution (overlap of the channel's FOVs) and vice versa. As presented in Fig. 4.4, off-axis aberrations of the outer channels lead to larger spot sizes of image points for larger field angles and, wider and lower ASFs. This is equivalent to lower angular resolution and lower sensitivity. An adaption of the pinhole size to the field angle would reduce the degradation of sensitivity with increasing field angle, but further degrade the angular resolution in these cases. In approximation, the angular sensitivity function has a Gaussian shape, if pinhole and PSF are of similar size. The pinhole size is then well matched to the PSF in terms of resolution and sensitivity. If the pinhole is larger than the PSF there results in approximation of the ASF a Super-Gaussian shape, in extreme cases
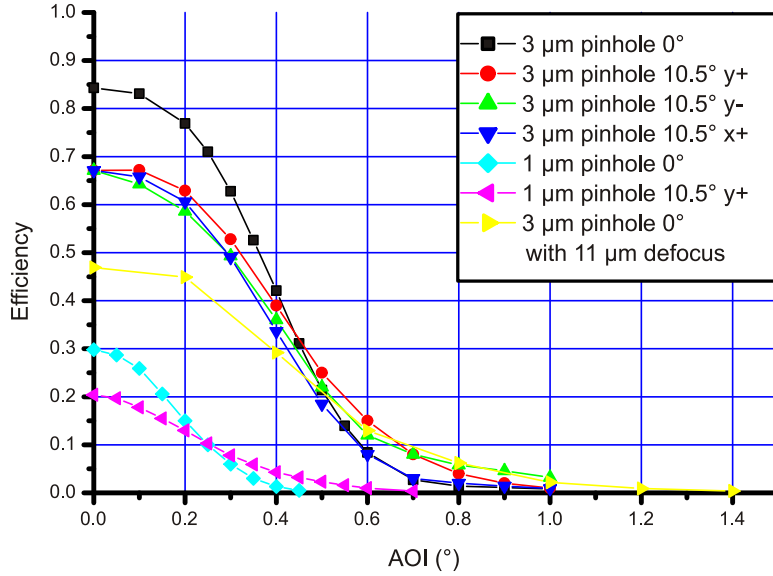
Figure 4.4. Simulated ASF for a single ommatidium with $D = 85\mu$m and focal length in glass $f_{n'} = 300\mu$m. The sagittal (x+) and the tangential (y+/-) sensitivity functions are given. Different pinholes sizes and field angles are examined. In the simulations the system is perfectly focused. One simulation with 11μm defocussing on-axis with $d = 3\mu$m pinhole is presented for comparison with experimental results. Raytracing was used for the transmission of the microlens for accounting for aberrations. Free space wave propagation was used between the microlens and the pinhole to account for diffraction effects.
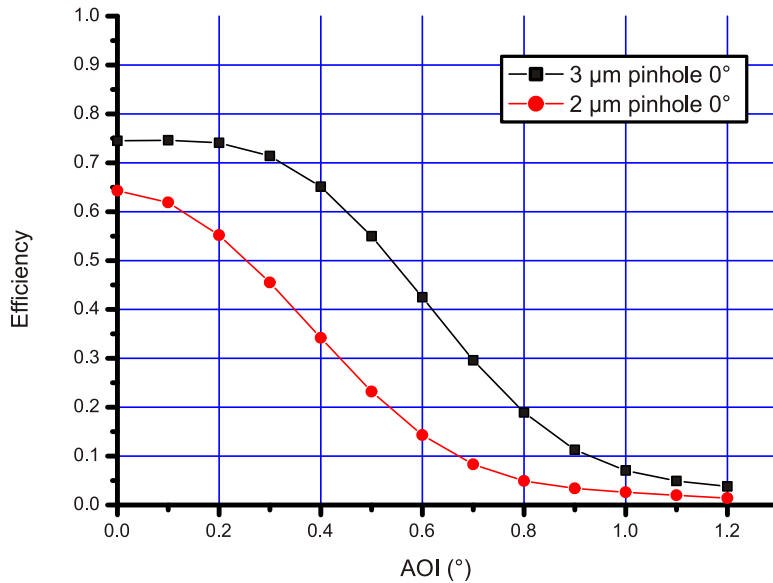

Figure 4.5. Simulated ASF for a single ommatidium with $D = 68\mu$m and $f_{n'} = 216\mu$m. Two different pinholes sizes are examined for on-axis performance. In the simulations the system is perfectly focused.

being even close to a rectangular shape. Then, a small change in object position close to the viewing direction is not reflected in any change of the ASF. The resolution is low. If the pinhole is smaller than the PSF, the width of the ASF is also small, but limited by the size of the PSF. Furthermore the sensitivity is low.

The analysis of two ommatidia with similar $F/\#$ and same pinhole diameter (3μm) but large difference in length (Fig. 4.4 and Fig. 4.5) demonstrates an important effect of scaling: The ASF of the 216μm-system has almost twice the FWHM of the 300μm-system. Consequently the 216μm-system has a lower resolution.

4.2.2 Characteristic Parameters of the APCO

Acceptance angle. The acceptance angle $\Delta\varphi$ (Fig. 4.2) is given by the FWHM of the ASF

$$\Delta\varphi = \frac{\text{FWHM}(\hat{d} \otimes \text{PSF})}{f}. \tag{4.1}$$

Small angles $\Delta\varphi$ are assumed. $\hat{d}$ stands for the transmittance distribution of the pinhole with the diameter d and $\otimes$ stands for convolution. $\Delta\varphi$ equals the smallest resolvable object period defined by the optical cut-off of the ommatidium (see Section 2.1.2).

Artificial receptor response functions are of rectangular shape. Consequently, applying the approximation Eq. (2.3) known from natural apposition compound eyes for simplification of Eq. (4.1) is not exact. However, for those cases examined in Section 4.2.1, Eq. (2.3) showed to deliver the same values of $\Delta\varphi$ as taking the FWHM of the ASFs. If the pinhole size is small compared to, or in the order of magnitude of the PSF, a Gaussian function is consequently a sufficient approximation [5].

If aberrations have a strong influence on an ommatidium's performance a further improvement of accuracy of $\Delta\varphi$ and better approximation of Eq. (4.1) is obtained by additionally considering the effect of aberrations in Eq. (2.3)

$$\Delta\varphi = \sqrt{\left(\frac{d}{f}\right)^2 + \left(\frac{2\xi}{f}\right)^2 + \left(\frac{\lambda}{D}\right)^2}. \tag{4.2}$$

Here, ξ is the RMS geometrical spot radius of the blurred focus due to aberrations.

Interommatidial angle. The Nyquist frequency of resolution of an APCO is defined by the interommatidial angle

$$\Delta\Phi = \arctan\frac{\Delta p}{f}. \tag{4.3}$$

Δp is the pitch difference between microlens- and pinhole array.

Information capacity. The maximum number of resolvable LPs over the FOV is half the number of channels in the APCO if the acceptance angle of the ommatidium is perfectly matched to the interommatidial angle which means $\Delta\varphi = 2\Delta\Phi$ (Nyquist criterion). This means that there is no large overlap of the FOVs of the different ommatidia. If the acceptance angle of an ommatidium is larger than the interommatidial angle ($2\Delta\Phi < \Delta\varphi$), the period of

resolvable LPs is determined by the FWHM of the ASF, $\Delta\varphi$. The obtainable angular resolution is consequently $1/\Delta\varphi$. The number of resolvable LPs over the FOV is then defined by

$$\chi_{LP/FOV} = \text{FOV}/\Delta\varphi. \tag{4.4}$$

This is equal to half the number of obtainable image pixels. For a given acceptance angle it is desired to have a large FOV in order to obtain a large number of image pixels.

The optical performance of an ommatidium usually limits the performance of the overall compound eye imaging system. The space bandwidth product of the single microlens [3] generally limits the information capacity [18] of an artificial apposition compound eye if the lenses are equivalent. The size of the sampled micro-images behind the microlenses is in the order of magnitude of the size of the microlenses themselves and one point of information has approximately the size of the PSF of the microlens. $\Delta\Phi$ and the number of channels are technically simple to tune. However, $\Delta\varphi$ determines, whether the resolution given by the array geometry can be actually exploited. Therefore understanding the behavior of the single channel is the key to reasonably design an APCO.

Micro-image size. The size of the sampled micro-image, a, is determined for a given pitch difference Δp by the number of channels N_{tot} along one dimension in the objective

$$a = \Delta p \, N_{tot}. \tag{4.5}$$

Usually $a < p_L$ is chosen in order to maintain some free space between the micro-images to reduce crosstalk by application of opaque walls between channels. In the case of $a = p_L$ the FOV is determined by the NA of the microlenses. This is interesting when examining the system's scaling behavior.

Field of view. The FOV of the APCO in the exact form is given by

$$\text{FOV} = 2\arcsin\left(\frac{n'}{n}\sin\left(\arctan\frac{a}{2\,n'f}\right)\right). \tag{4.6}$$

Herein, n and n' are the refractive indices of the incident medium and the substrate, respectively. Assuming a small FOV, so that $\sin \approx \tan$ and the incident medium to be air, $n = 1$, the expression for the FOV simplifies to

$$\text{FOV} = 2\arctan\frac{a}{2f}. \tag{4.7}$$

In the approximation of small angles this is equivalent to $\text{FOV} = N_{tot}\,\Delta\Phi$.

Distortion. For large FOVs a considerable amount of distortion occurs because the whole image space is filled with the substrate material $n' > 1$ and there is a constant pitch difference Δp within the whole array. Let N be the number of the considered channel with respect to the

central one. Consequently, $a_{real} = N\Delta p$ is the pinhole position within this considered channel leading to distortion. The real chief ray angle

$$\epsilon_{real} = \arcsin\left(\frac{n'}{n}\sin\left(\arctan\frac{a_{ideal}}{2n'f}\right)\right) \tag{4.8}$$

deviates from the ideal one

$$\epsilon_{ideal} = \arctan\frac{a_{ideal}}{2f} \tag{4.9}$$

where $a_{ideal} = aN/N_{tot}$ is the considered ideal image size, which has to increase linearly from channel to channel, for the imaging system to be free of distortion.

As an example, for $f = 150\mu m$, $n = 1$, $n' = 1.5$ and $\epsilon_{ideal} = 25°$ (maximum angle in a FOV of 35°x35°), ϵ_{real} is 26.5°. This is equivalent to a distortion [17] of 5.6%.

Using the APCO, distortion can be corrected by adjusting the pinhole positions. This is achieved by using

$$a_{real} = \tan\left(\arcsin\left(\frac{n}{n'}\sin\left(\arctan\left(\frac{aN}{N_{tot}2f}\right)\right)\right)\right)2n'f \tag{4.10}$$

for the calculation of the pinhole position within the considered channel instead of $N\Delta p$. Now, the overall objective provides a moiré-magnified image, free of distortion. Since receptor arrays usually have constant pitches, the adjustment of microlens-receptor offset must be implemented in a variable pitch of the MLA.

The angular resolution properties of an artificial apposition compound eye imaging system can now be understood. In the next paragraph its interrelationship with the sensitivity will be analyzed.

4.2.3 Interrelationship of Optical Properties under Scaling

As it was derived in Section 2.3, the sensitivity of an imaging system to an extended source is only determined by the system's $F/\#$ [27, 29]. This also applies to compound eyes [28].

In order to calculate the total flux a receptor receives, the intensity in the image plane and the area of the circular pinhole have to be multiplied. Applying Eq. (2.27), the power captured by one pinhole is consequently

$$P_I = \tau I_O \left(\text{NA}\right)^2 \frac{\pi d^2}{4}. \tag{4.11}$$

This is expanded by L^2/L^2 with L being the optical system length which is $L = f_{n'} = fn'$ where n' is the refractive index of the substrate ($n' \approx 1.5$).

Applying Eq. (4.2) with the pinhole diameter in a region between much larger than the Airy disk diameter and matching the diameter of the Airy disk, it follows $\Delta\varphi \approx \sqrt{2}\,d/f$. Then it is found [202]

$$P_I = \frac{9\pi}{128}\tau I_O \left(\text{NA}\right)^2 L^2\frac{1}{\frac{1}{\Delta\varphi^2}}, \tag{4.12}$$

where $\frac{1}{\Delta\varphi}$ is the angular resolution in LPs per radian (LP/rad).

4.2. Design and Simulation of APCO

The sensitivity P_I/I_O is inversely proportional to the square of the resolution with the product of the NA of the microlenses and the system length squared being the parameter. Figure 4.6 gives a representation of Eq. (4.12) assuming $\tau = 1$.
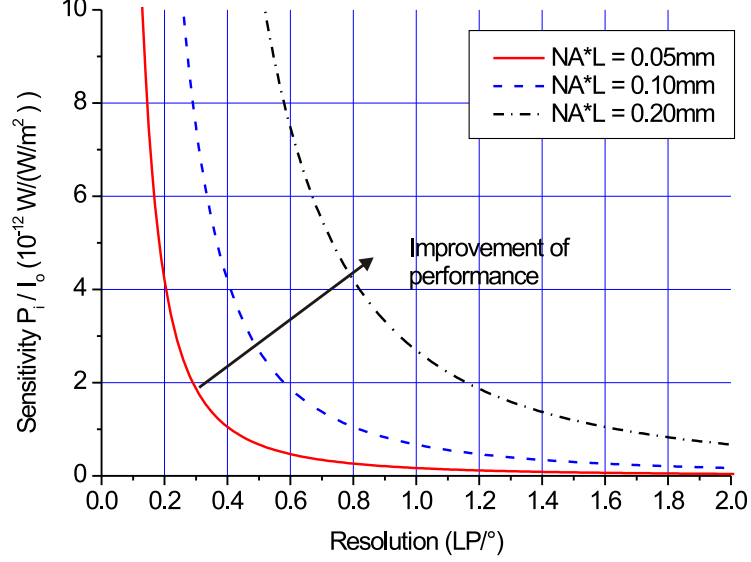

Figure 4.6. Resolution of APCOs vs. sensitivity to an extended source. For a given set of NA and system length there is a trade-off between sensitivity and resolution which is mainly determined by d.

It follows that high sensitivity and high resolution can not be achieved at the same time for a given set of parameters of NA and L (Fig. 4.6). The overall performance of the eye can only be improved if the product NA L is increased. This is consistent with the scaling behavior of natural apposition compound eyes.

The optical performance of the realized systems is well indicated by the red curve in Fig. 4.6.

Let the receptor diameter d be fixed and small compared to the PSF of the microlens resulting in diffraction limited resolution. Table 4.1 presents how angular resolution ($1/\Delta\varphi$), sensitivity (P_I/I_O), FOV ($\sim 2\arctan(D/2f)$) and volume ($V \sim D^2 f$) of the APCO change with a scaling of the geometrical parameters of the microlens using Eq. (4.2) ($\xi = 0$) and Eq. (4.12). For a fixed NA of the microlenses an increasing of length improves resolution but has no influence on sensitivity. However, also the lateral extension of the single channel and thus of the overall objective increases. This is especially important because with smaller $\Delta\varphi$ also $\Delta\Phi$ should be decreased and consequently more channels must be used in order to exploit the full image information. The diffraction limited resolution in case of scaling of length but fixed microlens diameter does not change. Increasing the microlens diameter for a fixed length improves all optical parameters, however, the area of the objective is increased and a large microlens NA results in large aberrations. The enlargement of FOV by an additional beam deflection in the microlenses results in an increased number of resolvable pixels while all other parameters are constant. This can be achieved by using for instance segments of microlenses

which are decentered with respect to the channel origin.

Table 4.1. Scaling of angular resolution $(1/\Delta\varphi)$, sensitivity (P_I/I_O), FOV and volume (V) as a function of the geometrical parameters of the microlenses.

Fixed parameter	Scaling parameter	$1/\Delta\varphi$	P_I/I_O	FOV	V
NA	f	$\sim f$	const.	const.	$\sim f^3$
D	f	const.	$\sim 1/f^2$	$\sim 1/f$	$\sim f$
f	D	$\sim D$	$\sim D^2$	$\sim D$	$\sim D^2$
f, D	FOV	const.	const.	$\sim$ FOV	const.

In case of monitoring tasks such as surveillance and movement detection, requiring only low resolution but high sensitivity, the receptor diameter should be large compared to the microlens PSF. Then the scaling of $1/\Delta\varphi$ with change of f or D is different. $1/\Delta\varphi$ is proportional to f for scaling of f (fixed D) and constant for scaling with D (fixed f).

Summing up the design rules it is important to note that the correct tuning of $\Delta\varphi$ via d/f and λ/D with respect to the desired resolution and sensitivity seems to be most crucial. $\Delta\Phi$ and the adequate number of channels just follow from that and the desired FOV. For a constant microlens NA, the longer an APCO, the larger is its spatial information capacity. The easier it is to achieve a high resolution and a high sensitivity at the same time. But this also leads to an increased lateral extension of the single channel and the overall APCO size which equals the size of the single channel times the number of channels.

4.3 Fabrication of APCO

4.3.1 Imaging System without Opaque Walls Between Adjacent Channels

The fabrication of the APCO has been carried out by using lithographical processes on a wafer scale. It is based on the patterning of a thin 4" glass wafer with arrays of circular microlenses in a rectangular arrangement on one side and pinhole arrays on the opposite side. The thickness of the wafer is matched to the microlens focal length in the glass.

The pitch of the pinholes differs from that of the MLAs to realize a different viewing direction of each channel. The parameters of different arrays on the pinhole photo mask (array size, pinhole pitch and diameter) were varied in such a way that different camera chips were realized on each wafer. The pinholes were generated by photo lithography and wet etching of a thin titanium film on the glass wafer. The ideal diameter of the pinholes to capture as much light as possible at optimum resolution is $d \approx 3.5\mu$m using Eq. (2.16) with the system parameters given in Tab. 4.2 (Type Ib) and assuming $\lambda = 550$nm.

The generation of the MLAs consists of several steps involving master and mold generation and subsequent UV-replication [210]. The photo resist master pattern is fabricated on a silicon

wafer in a standard procedure (photo lithography in combination with a heating/reflow process [187]). The replication is carried out in a modified contact mask aligner (SUSS MA6 with UV-embossing option) where the gap between glass wafer and mask/mold is filled by a UV-curing inorganic-organic hybrid polymer which is subsequently cured and separated from the mold. The mask aligner enables wedge error compensation as well as lateral and axial alignment of front and back side patterns. The most critical fabrication issue is the uniformity of the axial distance between microlens vertex and pinhole, affected by a series of parameters like precision of the MA6-height-alignment ($\pm 1\mu$m), bowing of the mold, mask holder, chuck, and substrate ($\pm 6\mu$m overall) as well as by non-uniform microlens focal lengths across the wafer ($\pm 3\mu$m). A compilation of major technological parameters of the fabricated systems is compiled in Tab. 4.2.

Figure 4.7 presents a schematic side view of the fabricated APCO and Fig. 4.8 a photography of the front view. The MLA fills the whole substrate with identical microlenses. The metal layer with the pinholes determines separation, size, channel number and increment of the FOV of the different cameras. For this first demonstrator, apertures to prevent stray light through the gaps between the microlenses were not applied onto the MLA layer. Next technological steps will include this procedure. Apertures on the microlenses do not necessarily need to be applied after the replication process, e.g. by lift off, but alternatively can be structured on the substrate prior to the replication process.
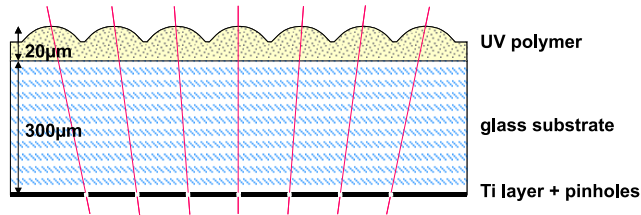

Figure 4.7. Schematic side view of the fabricated APCO (type Ib) consisting of MLA layer, substrate and metal layer.

An APCO has a low fill factor of pinholes in the image plane. It is consequently more suitable for optoelectronic sensor arrays which also have a low fill factor rather than for a combination with conventional densely packed CCD- or CMOS sensor arrays. Therefore, ultra-thin APCOs customized to the geometrical parameters of a large-pitch CMOS sensor for low-cost, fast, and robust vision, even under extreme illumination conditions, were designed and fabricated. The 128x128 pixel sensor array with 69μm pixel pitch and 21.4x21.4μm^2 pixel size includes an on-chip analog computation of the contrast magnitude and the direction of image features by shifting part of the signal processing to the pixel itself which results in a low fill factor ("artificial retina") [211]. This is a reasonable approach because in general relevant visual information, such as object contours, is represented by the changes in intensity (spatial gradients) rather than absolute intensity values. Reducing the image information to significant changes in intensity considerably lowers the computational burden for further processing steps.

The pitch of the APCOs pinhole array was matched to the pixel pitch of the sensor array

Table 4.2. Parameters of fabricated APCOs. Parameters are constant over one objective within fabrication limits. Different objectives for variation of parameters were realized on wafer scale. Refractive indices are given for $\lambda = 550$nm.

Type	Ia	Ib	II
	Fig. 4.1 (b)	Fig. 4.7	Fig. 4.9
System	on supporting substrate with included opaque walls	directly attachable to sensor array no opaque walls	
Thickness (μm)	345	320	214
Number of channels	11x11-150x150		130x130
$F/\#$	2.6		2.2
FOV (°x°)	15x15		20x20
Magnification equivalent focal length (mm)	3.7-34		24
Metal layer	sputtered titanium, thickness 200nm, transmission $< 0.01\%$ structured by photo lithography + wet etching		
Pinhole pitch (μm)	85-90		69
Pinhole diameter (μm)	1-6		2-8
Size of sampled micro-images (μm^2)	60x60		48x48
	gap left to reduce crosstalk or to provide space for opaque walls		
Spacing structure microlens-pinhole	SU8 photo polymer, $n' = 1.60$, structured gaps filled with absorbing polymer cast width of gaps/opaque walls: 30μm	float glass substrate D263T, $n' = 1.52$	
Spacing thickness (μm)	260	300	188
Prevention of cross talk?	yes	no	no
Microlenses	inorganic-organic hybrid UV-polymer, acrylate type $n' = 1.50$, replication by UV-molding, master structures generated by lithography and reflow		
Pitch (μm)	90		69.35, 69
Diameter (μm)	85		68
Layer thickness (μm)	85	20	26
Radius of curvature (μm)	118		75
Form deviation	< 20nm RMS		
Replication	back side alignment in SUSS Microtec MA6, fabrication on 4" wafers		
Lateral registration error	$\pm 3\mu$m		
Axial alignment	$\pm 10\mu$m across 4" including focal length non-uniformity		

(Fig. 4.9). For given FOV and $F/\#$ a design thickness of 206μm and an MLA pitch of 69.35μm resulted for the objective. This thickness is a compromise between focusing on-axis and at the rim of the field. The fabrication of the objective is similar to the previous one. Even with this sophisticated technology for replication, considerable variations of the thickness of the replicated layer occur. They result in a varying resolution across the wafer. The variation is approximately $\pm 10\mu$m around the center value of 214μm, which is actually the length for best focusing on-axis.
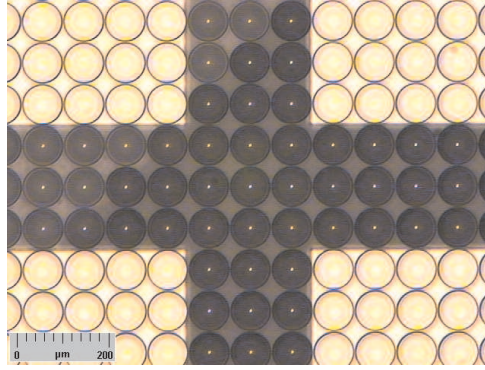
Figure 4.8. Photograph of the front view of a demonstration wafer in the corner between 4 different cameras. The overlap of the metal layer and the MLA layer is presented to show precision of replication. The MLA fills the whole substrate with identical microlenses. The metal layer with the pinholes determines camera size, channel number and increment of the FOV of the cameras.

The parameters of the realized objectives are given in Tab. 4.2 (Type II). Objective chips with different pinhole sizes covering the photo sensitive area of the sensor pixels were realized on wafer scale in order to examine the influence on resolution and sensitivity (Fig. 4.10). Some objectives with equal pitches of microlens- and pinhole array were generated resulting in a unity magnification. The wafers were subsequently diced and the objectives were aligned in front of the detector array (Fig. 4.11). Some objectives were fixed to the sensor array by UV-curable glue for permanent use as thin camera system. Gluing the APCO to the sensor over the complete back surface reduces Fresnel reflections by up to 8%, because of the reduction of an air gap. Care must be taken when fixing objective and sensor array, if materials of both have a large difference in their coefficient of thermal expansion. The sensor temperature may change drastically during operation. Pyrex seems to be an attractive substrate material considering the matching of the coefficient of thermal expansion with Silicon, which usually is the sensor material.
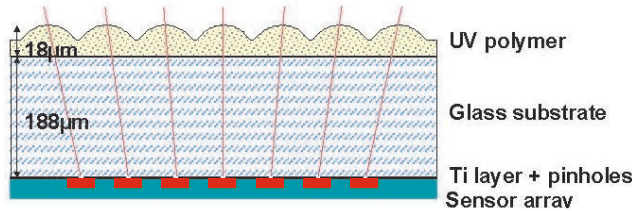

Figure 4.9. Schematic side view of the ideal device without opaque walls (type II), attached to sensor array. The MLA layer, replicated into UV-curing polymer, the glass substrate, the metal layer including the pinholes and the optoelectronic sensor array are exhibited.

The size of the object, presented to the vision system must be matched to its FOV to avoid cross talk of adjacent channels. Otherwise, in case of large AOI from object points outside the FOV in the current setup, light focused by one microlens may be received by a receptor of the
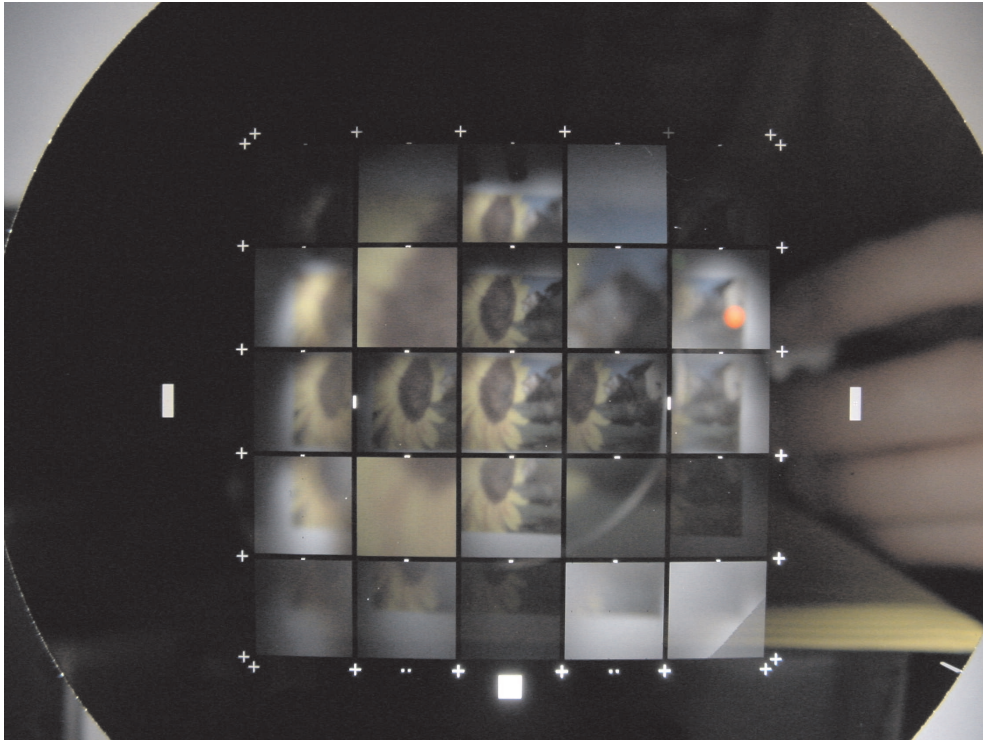
Figure 4.10. Wafer with 5x5 ultra-thin objectives before singularization, imaging the picture of a sunflower. Objectives with different pinholes sizes and also objectives with equal pitches of microlens- and pinhole array resulting in a unity magnification, are realized.
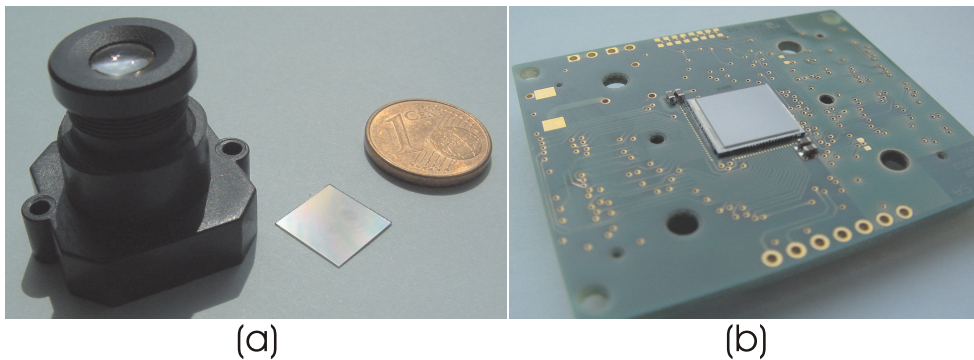

Figure 4.11. Diced APCO. (a) APCO in comparison to 1 Euro cent and a traditional single lens objective with the same magnification and approximate length of 20mm. (b) APCO attached to CMOS sensor array (courtesy of Centre Swiss d'Electronique et de Microtechnique SA (CSEM) Neuchâtel, Switzerland).

adjacent channel because of the lack of opaque walls between ommatidia in this technological approach. Ghost images from objects outside the FOV and a reduction of contrast may result. In order to overcome this problem the realization of an APCO with opaque walls, using a high aspect ratio photo lithography technology on a supporting substrate was investigated (Fig. 4.1 (b)).

4.3.2 Imaging System with Opaque Walls Between Channels

The region between pinholes and microlenses is not formed by a simple substrate but by a structured spacer layer consisting of transparent columns of SU8 photo polymer [212] (EPOXY NOVOLAK EPON SU8) and gaps which are filled by absorbing polymer cast (Fig. 4.12). The patterning of the columns was realized by state of the art SU8 negative resist technology [213] using an additional photo mask (Fig. 4.13 (a)). After hard baking of the SU8 columns for 10min at 110° C the gaps were filled by highly absorbing polymer cast (PSK2000 black matrix polymer, Brewer science) as shown in Fig. 4.13 (b). Pinhole and microlens fabrication remains unchanged. Finally, the MLA was replicated on top of this spacing structure (Fig. 4.13 (c)). The parameters of the realized objectives are given in Tab. 4.2 (Type Ia). Because the replication step is done with respect to the substrate surface (including wedge error compensation), an occurring SU8-thickness non-uniformity is balanced. The sum of SU8-thickness and replicated thickness was uniform within $\pm 1\%$. In future this procedure could be applied directly to the optoelectronics wafer as supporting substrate. This enables an integration of the objective assembly in the electronics fabrication process.
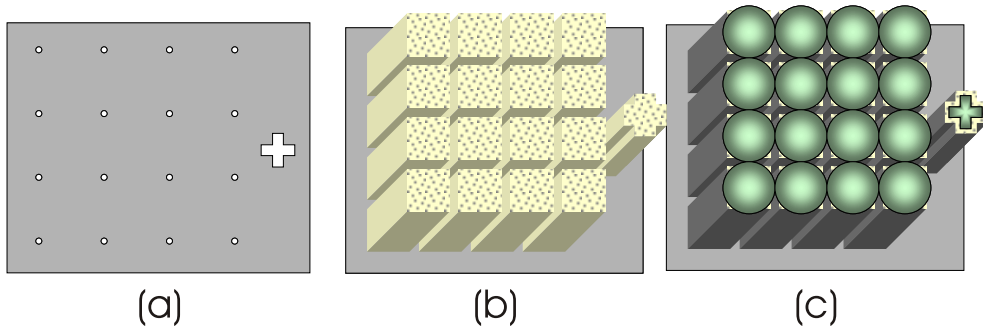

Figure 4.12. Monolithic APCO with optical isolation of the channels and fabrication steps. (a) Pinhole array on substrate works only as carrier and can later be replaced by the electronics chip itself. (b) SU8 pedestals with correct height structured on top. (c) Spacings between pedestals are filled with absorbing polymer and MLA, aligned to pinholes, is embossed on top in UV-curing polymer.
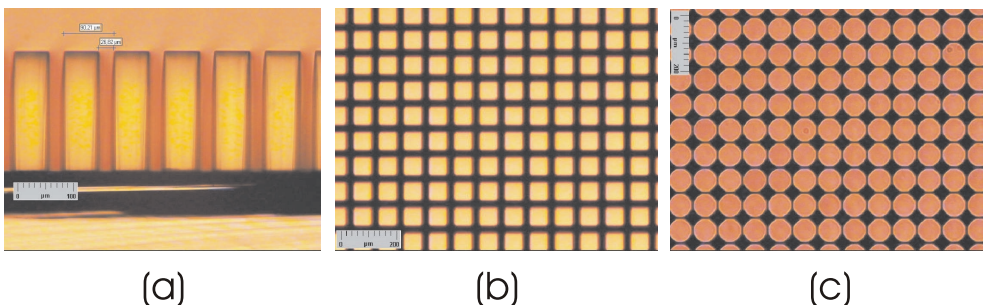

Figure 4.13. Photographs of fabrication of opaque walls. (a) Side view of transparent columns of photo polymer which are structured with high aspect ratio in SU8, forming the bulk structure of the channels. (b) Gaps are filled with absorbing polymer cast (front view). (c) MLA is replicated on top (front view).

4.4 Experimental Characterization of APCO

Different types of APCOs are examined with respect to resolution, sensitivity, FOV and cross talk. Major important parameters such as the pinhole diameter are varied and the effect on the optical performance is analyzed. Captured images are presented and the achieved optical performance is compared to theoretical limitations. For characterization, the image obtained by the APCO is relayed onto a conventional CCD sensor or the objective is directly attached to a CMOS sensor with matched pitch of the detector pixels.

4.4.1 Resolution and Sensitivity

4.4.1.1 Imaging the Pinhole Surface by Relay Optics on a CCD Sensor

Images of different bar targets were registered for characterization of the APCOs of Type I, which were not attached directly to sensor arrays. Here, the pinhole array surface was relayed on a CCD and the MTF was measured (Fig. 4.14 – Relay optics: Schneider-Kreuznach CINEGON 1.4/8 - 0512 or microscope objective). In order to prevent crosstalk between the adjacent channels without optical isolation, the size of test images presented to the device exactly matched to its FOV. The ASF was determined for a single mode fiber end face at $\lambda = 637$nm acting as point source. For measurement of the ASF, the fiber end face was moved laterally in object space at a distance of 300mm in front of a single ommatidium while the captured power in a pinhole was determined. Images of the point source, taken with a camera with 51x51 channels, were also analyzed. The power measured in the pinhole was normalized to the total integrated power of one channel. This was measured without pinhole. The MTF of the device was calculated from the measured ASF for comparison.
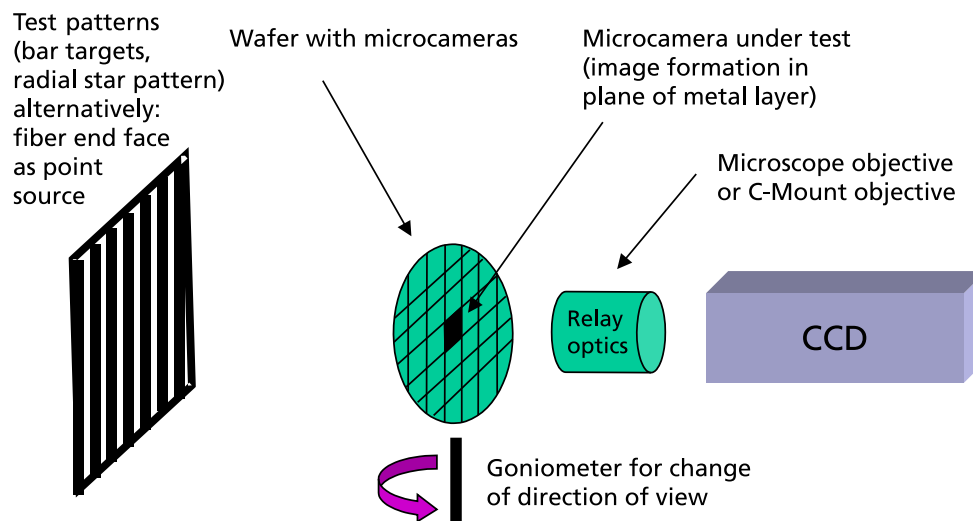

Figure 4.14. Relay setup for characterization of APCO.

Figures 4.15 and 4.16 present the measured on-axis sensitivity function in case of a $d = 3\mu$m pinhole. The measured ASF has a FWHM of approximately 1.3° which is much larger than expected from the simulations presented in Fig. 4.4. Accordingly, the experimental efficiency

is much lower. The theoretical curve according to Eq. (2.2) with $\Delta\varphi = 0.8°$, normalized to the same starting value is given in Fig. 4.16 for comparison. Simulations showed that the experimentally achieved results correspond to a defocussing of the pinhole layer with respect to the MLA of the analyzed APCO of 11μm (compare with Fig. 4.4). The reason for this deviation was found to be a discrepancy of refractive index of the substrate material in design and experimental realization. It is thus not caused by the fabrication tolerances and did not repeat in further fabrication runs. From the theoretical sensitivity function from Fig. 4.4 (FWHM=0.8°) it can be expected that within the horizontal/vertical FOV of 15° approximately 20LP should be resolvable. A sampling with 51x51 channels consequently gathers all available information.
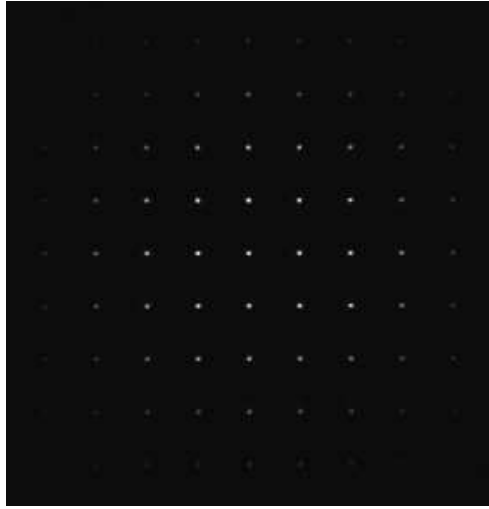

Figure 4.15. Response to a point source (pinhole surface strongly magnified). Image of the single mode fiber end face using a camera with 51x51 optical channels and $d = 3\mu$m. The separation of viewing directions of the channels is 0.3°. The response of several ommatidia in the camera to one source point gives an impression of the resolution of the device.

The MTF of an APCO with 101x101 channels, 15° horizontal FOV and $d = 3\mu$m pinholes was measured imaging bar targets with different spatial frequencies (Fig. 4.17). Each signal frequency response (SFR) was calculated using an FFT formalism. Here, the amplitude of the first harmonic with respect to the DC peak of the original and the imaged bar patterns are compared after

$$\text{SFR} = \frac{\pi}{4}\frac{2G_1}{G_0}. \tag{4.13}$$

G_0 and G_1 are the coefficients of the DC peak and the first harmonic in the Fourier sum

$$G(x) = \frac{G_0}{2} + G_1\cos(2\pi x/p) + ... \tag{4.14}$$

of the bar pattern, respectively. $4/\pi$ is the ratio of $G_1/\frac{G_0}{2}$ in case of an ideal square wave [24,35]. p is the bar targets period and x is the coordinate. This resulted in the experimental MTF presented in Fig. 4.18.

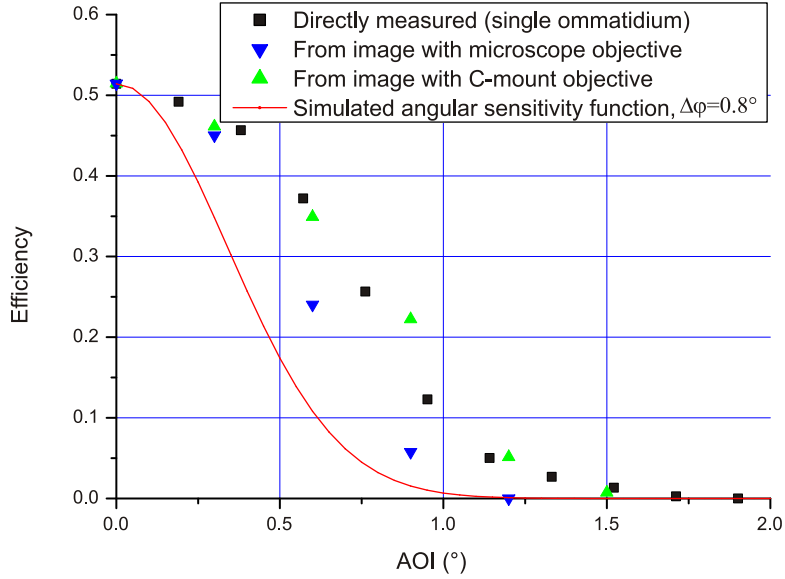**Figure 4.16.** Measured on-axis ASF for ommatidia with $D = 85\mu$m and $f_{n'} = 300\mu$m and $d = 3\mu$m. Results of a direct measurement for a single ommatidium while moving the point source in front of it are presented. Measured and normalized energies in images of a point source taken with a 51x51 channel APCO (Fig. 4.15) were also analyzed. The theoretical curve, normalized to the same starting value and following Eq. (2.2) with $\Delta\varphi = 0.8°$, is given for comparison.
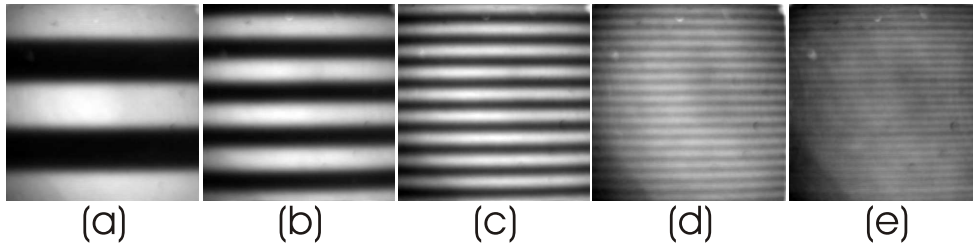

Figure 4.17. Bar targets of different frequencies imaged by an APCO with 101x101 channels, 15° horizontal FOV and $d = 3\mu$m pinholes. (a) 2.5LP/FOV, (b) 5LP/FOV, (c) 10LP/FOV, (c) 20LP/FOV, (c) 28LP/FOV. Image processing as Gaussian blurring (2 CCD pixels), brightness, contrast and intensity was applied to enhance image quality in this figure as done also by commercial digital cameras.

Performing the Fourier transformation of the ASF according to Eq. (2.4) also allows to calculate the ideal MTF of the optical system [5,19]. The simulated MTF for $\Delta\varphi = 0.8°$, with the spatial frequency given relative to the FOV, is compared to the measured MTF in Fig. 4.18. A good correspondence can be observed. It can be seen in Fig. 4.18 that the cut-off of the MTF calculated from experimental data is between 20LP/FOV and 30LP/FOV. This is larger than to be expected from the experimental ASF at the determined amount of defocussing.

Figure 4.19 (a) and (b) present different test images taken by cameras with 101x101 channels without opaque walls and $d = 3\mu$m pinholes. Figure 4.19 (c) shows the image of a radial star pattern centered within the FOV using an objective with 101x101 channels, included opaque walls and $d = 5\mu$m pinholes. Because of inhomogeneities in the height of the SU8 photo polymer
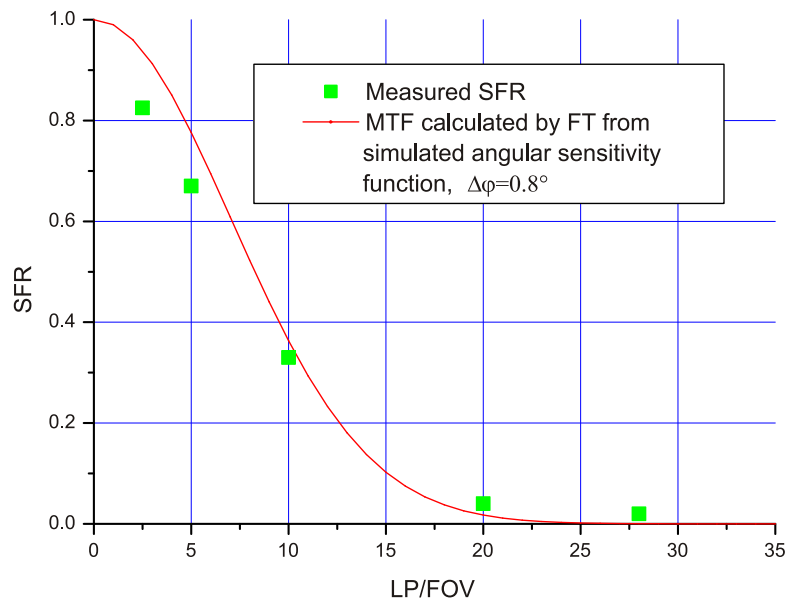
Figure 4.18. Measured and ideal MTF. The ideal MTF was calculated using Eq. (2.4) with $\Delta\varphi = 0.8°$. The experimental MTF was determined from the imaged bar targets presented in Fig. 4.17. It was acquired without any subsequent image processing except Gaussian blurring with 2 CCD pixels for smoothing of the images determined by the CCD resolution.

and the difference in refractive index between SU8 and the polymer the MLA is replicated in, the optical thickness across the objective varies, even if the geometrical thickness is constant. Streaks within the SU8 columns also increase the microlenses PSFs. The resolution varies across the objective area and the images are slightly distorted.
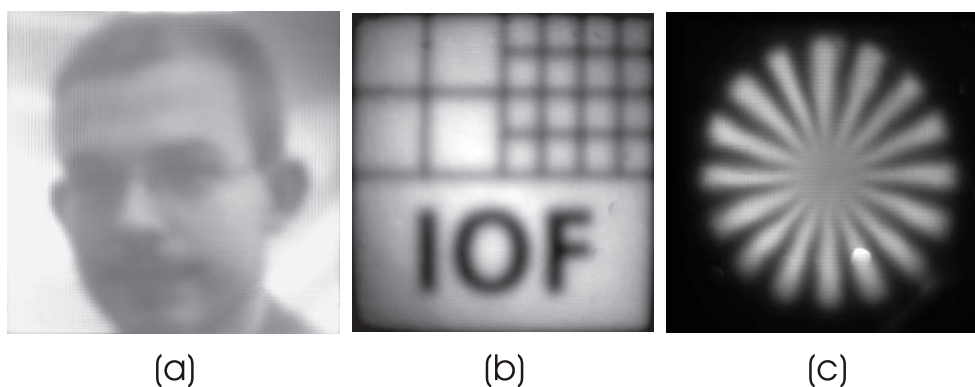

Figure 4.19. Test patterns imaged by the same APCO as used in Fig. 4.17 ((a) and (b)) and by a system with included opaque walls (c). Test objects fill the FOV of the camera under test. The object distance has no noticeable influence on the image quality. The observable distortion and reduced illumination at the outer parts of the images are mainly due to the relay optics. (a) Image of a passport photograph of the author (Compare to page 139). (b) Image of the institute's logo. (c) Objective with included opaque walls between channels imaging a radial star pattern. 101x101 channels, $d = 5\mu$m pinholes. The white dot is a mask defect.

4.4.1.2 APCO is Directly Attached to Optoelectronic Sensor

The APCO (Type II) is now aligned actively in front of the sensor array using a vacuum gripper arm which is attached to a precision six axis translation stage. The sensor board is fixed to a rotation stage with the rotation axis in the center of the detector array. A homogeneous white target is presented to the camera. The APCO and the sensor board are aligned with respect to each other until all pinholes are centered on their corresponding detector pixels and a homogeneous bright image is obtained from the sensor. Rotation between objective and sensor is especially critical and has to be avoided.

Different test patterns were presented to the vision system composed of the thin APCO and the "artificial retina" optoelectronic sensor array. The captured images are analyzed with respect to resolution and sensitivity, focusing homogeneity and subjective information content. As a result of the lack of opaque walls between the channels also in this technological approach, the size of the object presented to the vision system had to be matched to its FOV to avoid cross talk of adjacent channels.

A radial star pattern is well suited to determine the optical cut-off frequency of an imaging system. Here the object frequency is a function of the radial coordinate in the image. The resolution $\chi_{LP/deg}$ in LP/° is estimated by the cut-off of resolution in the image of the radial star pattern centered within the objective's FOV by

$$\chi_{LP/deg} = \frac{\chi_{LP}}{2\pi\beta}. \tag{4.15}$$

χ_{LP} is the number of angular LPs in the pattern. β is the angle in degree with respect to the optical axis at which the modulation of the angular pattern vanishes.

Figure 4.20 (a) and Fig. 4.21 (a) show the taking of the same star pattern using the APCO in Fig. 4.20 (a) and using a bulk, 1/3" image-format objective in Fig. 4.21 (a). Figure 4.21 (a) demonstrates the limitation of resolution by the sensors Nyquist frequency. The APCO achieves approximately half that resolution (Fig. 4.20 (a)). For an APCO with $d = 2\mu$m pinholes, a cut-off resolution of 32LP/FOV was determined. The capabilities of the optoelectronic sensor array with low fill factor are presented in Fig. 4.20 (b) and (c). It suits not only for acquisition of intensity images, but especially for close-to-the-pixel on-chip analogous computation of contrast and contrast direction without post processing in a subsequent computer.

Figure 4.21 (b) shows the caption of a portrait photograph of Carl Zeiss using the APCO. This demonstrates the capability of face recognition.

Bar targets of different spatial frequencies, such as in Fig. 4.21 (c), were imaged for a quantitative MTF determination. Each SFR was calculated after Eq. (4.13) and plotted vs. the corresponding angular frequency in Fig. 4.22. The measured MTF for $d = 2\mu$m pinholes corresponds to the cut-off predicted by the image of the radial star pattern in Fig. 4.20 (a). Approximately 30LP can be resolved over the entire FOV. The limiting factor of resolution of the generated APCO is the overlapping of the acceptance angles $\Delta\varphi$ of adjacent channels in object space which increases with increasing pinhole diameters. As expected, the smallest
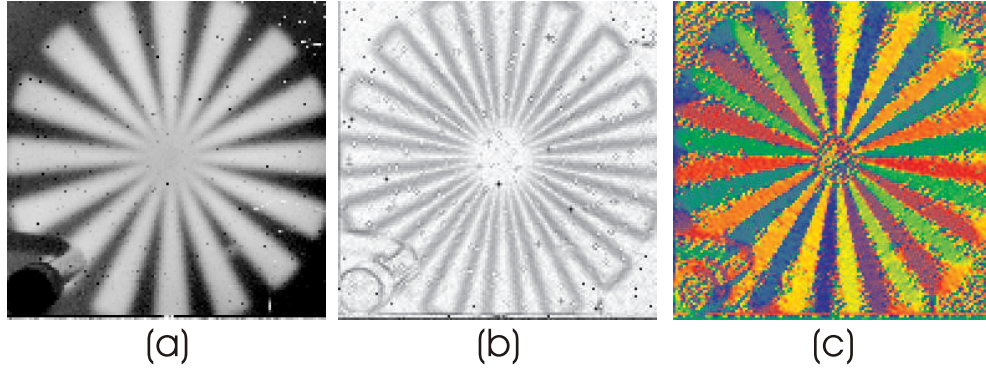
Figure 4.20. Radial star pattern with 16LP filling the FOV of the 0.2mm thin APCO of Type II with $d = 2\mu$m pinholes. A cut-off resolution at 32LP/FOV can be determined resulting in a resolution of 3.6LP/mm or 1.5LP/°. The black and white dots are due to random data transmission errors of the sensor's ethernet communication with the PC. The vacuum gripper for holding the objective over the sensor array, appears in the lower left corner of the captured test images. (a) Intensity image. (b) Close-to-the-pixel analogous computation of contrast. (c) Edge orientation (false color coded).
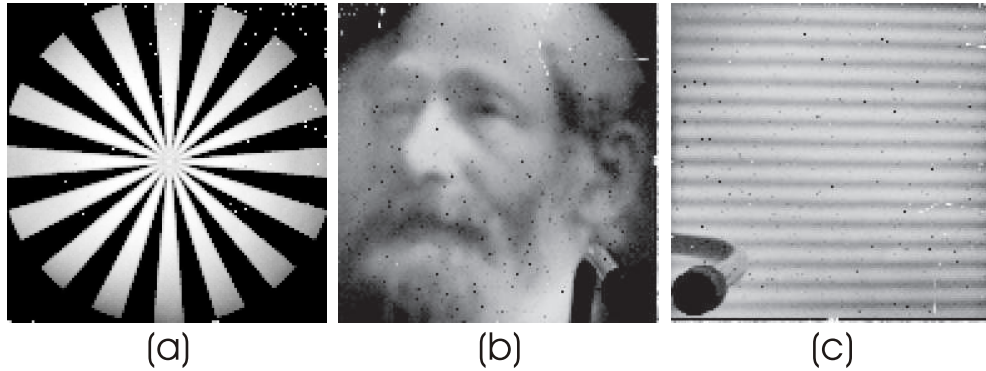

Figure 4.21. Test images using a bulk objective for comparison (a) and captured by the APCO of Type II (b, c). (a) The same test pattern as in Fig. 4.20 was also recorded using a bulk objective for 1/3" image format with a focal length of 12mm and an $F/\#$ of 2.0. In this case, the resolution is limited by the sensor's Nyquist frequency to 64LP/FOV. (b) Image of a portrait photograph of Carl Zeiss. (c) Example of imaged bar targets for MTF determination (here 16LP bar target).

pinhole size leads to the best MTF characteristics.

However, using small pinholes for improvement of resolution results in reduced sensitivity as shown in Fig. 4.6. In Tab. 4.3 the captured optical powers using APCOs with different pinhole sizes are normalized to the power using the bulk objective with a sensor array with bare pixels for the taking of the same plain image.

4.4.2 Ghost and Flare Analysis – Test of the Opaque Walls

A ghost image in the context of this analysis is understood as light which is focused from an object point outside the objective's FOV into its image plane not taking the originally desired path. High-intensity false signals may result. The overall (integrated) power in the image plane
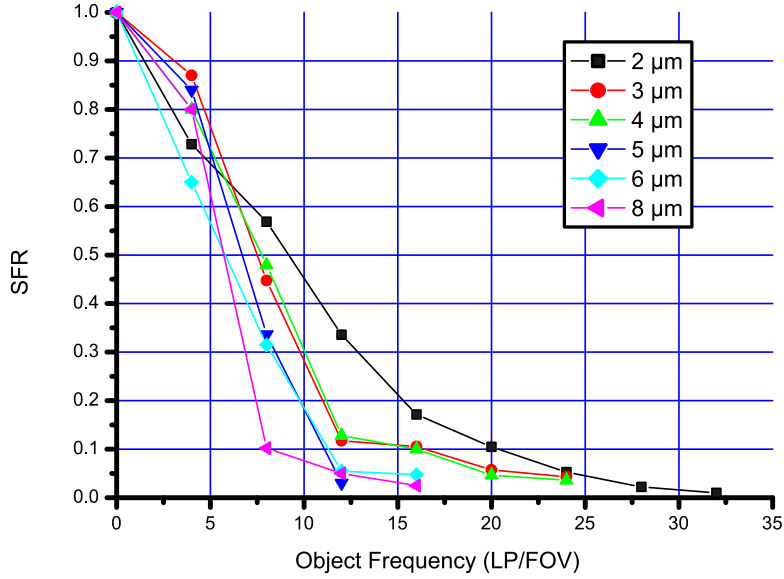
Figure 4.22. MTF of APCO with d as parameter.

Table 4.3. Measured sensitivity of compound eye camera normalized to using bulk objective with the same sensor array and bare pixels.

Pinhole diameter (μm)	2	3	4	5	6	8
Relative sensitivity (%)	2.4	4.8	10.0	15.2	35.0	38.3

as a result of a ghost may be the same as for a direct image point.

Light from one object point which is not brought to the desired image point but strongly distributed over the overall image plane is considered as flare, sometimes also referred to as veiling glare. The intensity usually is considerably lower than that of ghosts. The overall power on the sensor can be also in the order of magnitude of that of a desired image point.

Without optical isolation between channels, in case of large AOIs from object points outside the FOV, light focused by one microlens is received by an adjacent channel's receptor. Ghost images (upper part in Fig. 4.23 (a) and (b), lower part is original) of objects outside the FOV and a reduction of contrast result. This behavior prohibits the use of the APCO without opaque walls for arbitrary large objects compared to the system's FOV.

For evaluation of cross talk the radial star pattern was imaged off-axis by a system without opaque walls (Fig. 4.23 (a), (b)) under the same conditions as by a system including an optical isolation between ommatidia (Fig. 4.23 (c)). The radial star pattern is imaged under a large AOI so that half of it is outside the objective's FOV.

At this stage of development the APCO with opaque walls is patterned on a thick supporting substrate. This prohibits the direct assembly of the fabricated objective onto an optoelectronic sensor array. The obtained images of the APCO are relayed onto a conventional CCD camera for characterization [202].

For APCOs of Type Ib and II (without opaque walls), a ghost image of the test pattern part which is outside the objective's FOV appears on the opposite side of the image. For the APCO

of Type Ia, there results a blocking of light from outside the FOV because of the introduction of opaque walls in the spacing structure. Only the original part of the pattern is imaged (Fig. 4.23 (c), compare to Fig. 4.23 (a)). Ghost images are suppressed.
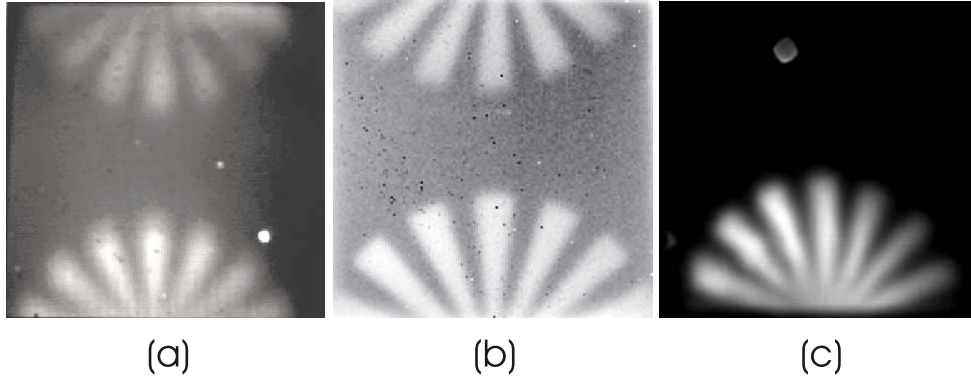

(a)   (b)   (c)

Figure 4.23. Original and ghost images with and without opaque walls by imaging a test pattern strongly off-axis. (a) Type Ib, without opaque walls, 101x101 channels, $d = 5\mu$m pinholes. (b) Type II, without opaque walls, 128x128 channels, $d = 2\mu$m pinholes, directly attached to sensor. (c) Type Ia, with opaque walls, 101x101 channels, $d = 5\mu$m pinholes. White dots are mask defects.

This is confirmed by a quantitative measurement of the response of the APCOs of Type Ia and Ib with 101x101 channels and $d = 3\mu$m pinholes to a 0.65° extended source. The source is presented to the imaging system under different angles of illumination inside and outside the FOV (Fig. 4.24 for system without opaque walls, Fig. 4.25 for system with included opaque walls). The wafers with the APCOs are attached to a rotation stage and tilted in order to do not loose light by the transfer through the relay optics for large AOI. The test object, the relay optics and the CCD are fixed. The corresponding diagrams for maximum intensity and integrated power on the sensor as a function of AOI are given in Fig. 4.26 and Fig. 4.27, respectively. In Fig. 4.24 all images have same source conditions. The blurred focus of the

(a)   (b)   (c)   (d)

Figure 4.24. False light analysis of APCO without opaque walls between channels. Images by the APCO of a 0.65° extended source. (a) -1° AOI (inside FOV). (b) 22.5° (outside FOV, focus of adjacent microlens). (c) 32.5° (outside FOV, intermediate position, no ghost). (d) 42.5° (outside FOV, focus of next but one microlens).

neighboring or next but one microlens on a pinhole can be observed even for large AOI. In Fig. 4.25 – system with opaque walls – false light becomes only visible because of increasing the
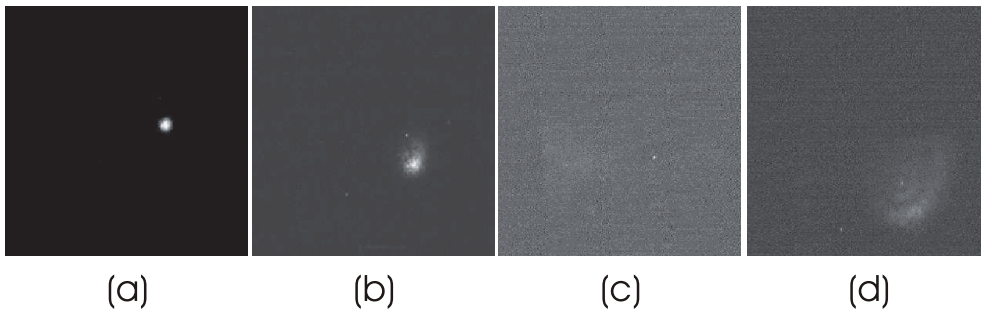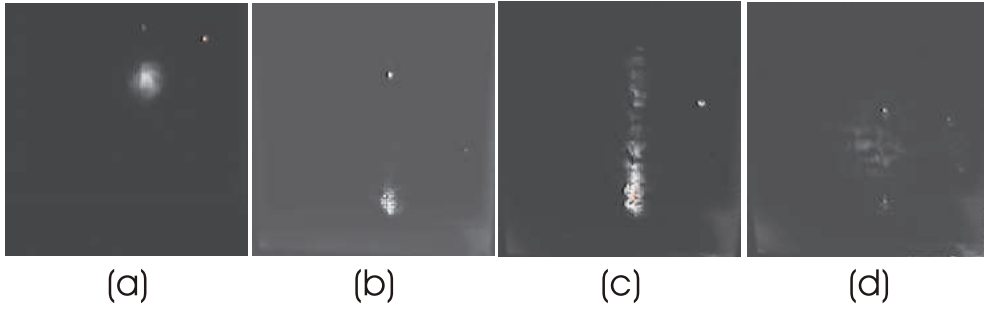
Figure 4.25. False light analysis of APCO with opaque walls between channels. Images by the APCO of a 0.65° extended source. (a) 0° AOI (inside FOV). It is important to note that for perpendicular incidence, an absorptive filter of transmission 0.06 was set in front of the source. This filter was removed for capturing (b) 22.5° (outside FOV), (c) 32.5° (outside FOV) and (d) 42.5° (outside FOV) so the effect of flare from the opaque walls could actually be observed.
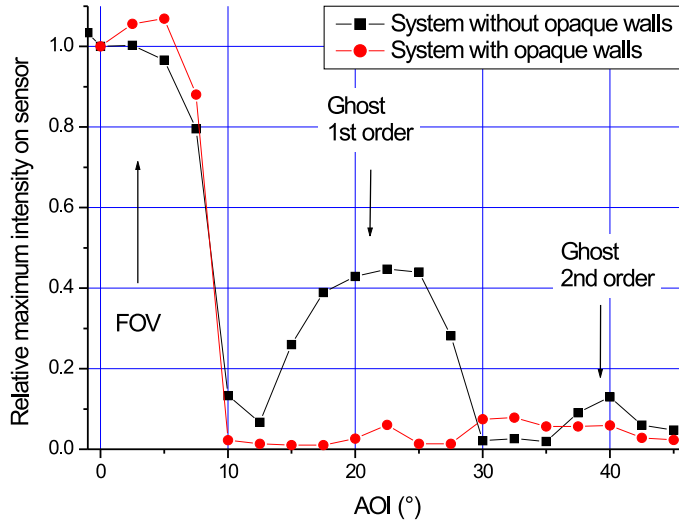

Figure 4.26. Maximum intensity on sensor vs. AOI. The region of AOI "FOV" is that with the corresponding microlens focusing on a pinhole. In the angular region of "Ghost 1st order" the focus of the adjacent microlens is brought on a pinhole and consequently for "Ghost 2nd order" the focus of the next but one microlens.

overall light level by a factor of 17 with respect to the on-axis illumination. Here, instead of observing the foci of the adjacent microlenses, the reflections within the channels can be seen, resulting in flare. False light is spread all over the image plane.

Finally, Fig. 4.26 and Fig. 4.27 quantitatively show the effect of opaque walls on imaging quality. The signal to noise ratio (SNR) of maximum intensity as well as of overall power on the sensor are drastically increased. Real image signals can be separated from false light much easier than without opaque walls. A fully operational ultra-thin imaging device based on artificial compound eye vision even for arbitrary large illuminated scenes is only achieved, if opaque walls are introduced between adjacent channels.

Residual false light using opaque walls can have different origins. There can be reflections
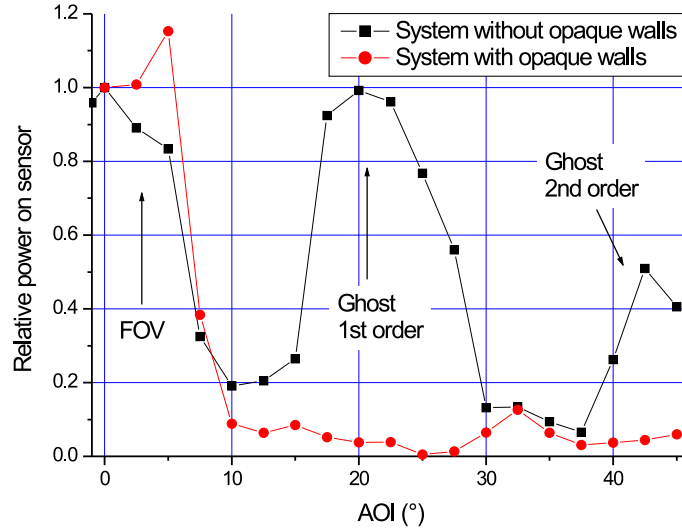
Figure 4.27. Integrated power on sensor vs. AOI.

at the opaque walls and streaks in the SU8 photo polymer. If the gaps between channels are not completely filled with absorbing polymer cast or microlens-polymer, even stronger reflections at polymer-air interfaces can occur. The height of the SU8 columns does not cover the complete thickness of the objective but the transparent layer of the replicated microlenses may be quite thick. Under large angles, light might cross channels at this position and lead to flare by reflections at the walls. The reflectivity of the interface SU8-absorbing polymer was not measured. Under large AOI the dielectric might have a high reflectivity. Further examination has to take place.

4.4.3 Extension of the FOV by an Additional Diverging (Fresnel-) Lens

The capabilities of FOV enlargement by the use of a diverging lens [7] in front of the APCO were investigated. This lens can be – as a Fresnel lens – almost as thin as the groove depth. The focal length of the used Fresnel lens is F_F = -21.6mm which after Eq. (4.16) results in an extension of the FOV by 23°.

$$\tan(\alpha_e) = \frac{S_F}{2F_F}. \tag{4.16}$$

Here, S_F is the used edge length of the Fresnel lens (in this case ≈ 9mm) and α_e is the half angle of FOV enlargement.

In order to demonstrate the effect of the Fresnel lens it was first combined with an objective without pitch difference between MLA and pinhole array (unity magnification). A usable FOV of 23°x23° of the objective resulted (Fig. 4.28 (a)). Figure 4.28 (b) shows the image of a test pattern (diameter of 28°) using an objective with pitch difference between microlens- and pinhole array without Fresnel lens. Introducing the Fresnel lens in front of the objective in the same setup, the FOV is drastically increased as can be seen in Fig. 4.28 (c). However, due to the lack of opaque walls in this arrangement, ghost images of the test pattern appear on all

sides. An enlargement of FOV by an external Fresnel lens without using opaque walls does actually not increase the visible object size.

Using the circular Fresnel lens, a moiré-effect becomes visible as the result of the overlap of rotational symmetric lens grooves with cartesian arranged channels. Consequently a large number of channels is covered by a groove of the lens resulting in a symmetrical pattern.

Figure 4.29 (b) presents the image of a 28°-diameter radial star pattern imaged by an objective with optical isolation of adjacent channels (101x101 channels and $d = 3\mu$m pinholes) without Fresnel lens. Introducing the Fresnel lens in the same setup, the objective's FOV is drastically increased as can be seen in Fig. 4.29 (c). A clear image without overlap with ghost images on the sides of the image is obtained (see Fig. 4.28 (c) for comparison with a system without opaque walls). The resulting FOV is approximately 38°x38°.

(a)   (b)   (c)

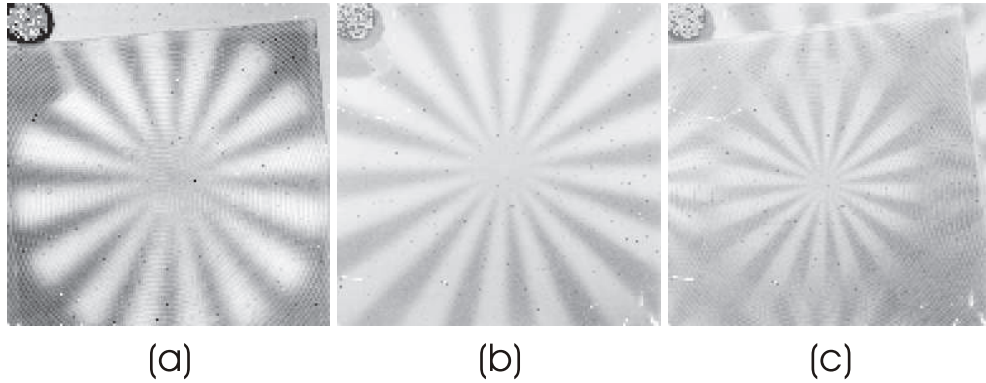**Figure 4.28.** APCO without opaque walls, directly attached to sensor (Type II, $d = 2\mu$m pinholes). (a) Generation of a FOV for an objective without pitch difference between microlens- and pinhole array (unity magnification) by attaching a Fresnel lens of focal length -21.6mm. The resulting FOV of the device is 23°x23°. (b) Image of radial star pattern with an angular extension of 28° in diameter, using an objective with pitch difference of microlens- and pinhole array but without the use of the Fresnel lens. (c) The implementation of the Fresnel lens in same setup is resulting in a FOV of the camera of approximately 42°x42°. Ghost images of the 28° diameter test pattern appear on the sides because of cross talk between channels.

4.5 Summary and Outlook on APCO

An APCO consists of an MLA and a pinhole array with different pitch in its focal plane with the optical axes of the ommatidia directed outwards and an optical isolation of adjacent channels. An optical channel delivers a signal only if an object point is situated on, or close to, its optical axis.

For the first time, a microoptical APCO with a thickness of 320μm and FOV of 15°x15° was experimentally demonstrated with a comparatively high resolution. The determined cut-off of resolution occurs approximately at 30LP over a horizontal FOV of 15°. This is sufficient for many sensor and imaging applications where system thickness is emphasized. It was shown
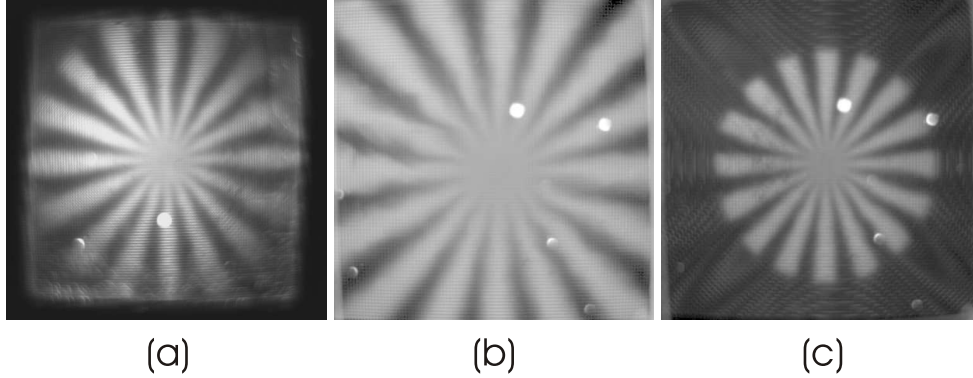
Figure 4.29. APCO with included opaque walls, image relayed onto conventional CCD sensor by C-mount objective (Type Ia, $d = 3\mu$m pinholes). White dots are mask defects. (a) Generation of a FOV for an objective without pitch difference between microlens- and pinhole array (unity magnification, 150x150 channels) by attaching the Fresnel lens. The resulting FOV of the device is 23°x23°. (b) Image of radial star pattern with angular extension of 28° in diameter using an objective with pitch difference of microlens- and pinhole array but without the use of the Fresnel lens (101x101 channels). (c) The implementation of the Fresnel lens in same setup is extending the FOV of the objective to approximately 38°x38°. Ghost images of the 28°-diameter test pattern on the sides of the image are suppressed (compare to Fig. 4.28 (c)).

that APCOs have the capability of a drastic reduction of the imaging system length far below 1mm. However, there is a trade-off between FOV, resolution and sensitivity. Larger pinhole diameters result in higher efficiency but lower resolution. The limiting factors of resolution are the size of the solid angle in the object space which each channel interprets as one image point and the relatively small FOV. The largest resolvable spatial frequency of the presented ultra-thin objective is thus much smaller than the Nyquist frequency which is determined by half the number of optical channels sampling the FOV.

The direct combination of the novel objective type based on artificial compound eye vision with an optoelectronic sensor array was successfully demonstrated. The thickness of the optics is approximately 0.2mm, and a resolution of 60x60 pixels and a FOV of 20°x20° was obtained. The experimental results show the suitability of the APCO concept for vision sensors with large pixel pitch but low fill factor. Such can be e.g. sensor arrays which allow on-chip signal processing. The technically achieved resolution of 1.5LP/° is comparable to the angular resolution of many invertebrate eyes.

The pinhole layer in the microlenses' focal plane was realized in titanium. Strong reflections may result. Future fabrication runs will include the testing of more absorbing materials for the pinhole layer such as black matrix polymer, "dark chromium" or "dark silicon", known from semiconductor technology.

Opaque walls have to be introduced between adjacent optical channels to prevent cross talk and resulting ghost images.

In contrast to classical single aperture eye imaging systems, in the APCO the magnification

is not determined by the microlenses' focal length and thus also not by the system length. The magnification is defined by the size and number of channels contributing to the moiré-image. It can consequently be much shorter than a classical imaging system with the same magnification. Furthermore, the optoelectronic pixel pitch and pixel size are separated. A high fill factor, such as in conventional imaging systems, is not necessary, even not desired in the APCO. A high resolution can be achieved by a short imaging system, even for large-pitch optoelectronic pixels, if only the pixels are small. This is not possible using a single aperture objective.

The space bandwidth product is equivalent to the theoretical maximum number of image pixels. For the realized systems it is 69x69 pixels for the Type I and 65x65 pixels for the Type II without consideration of the pinholes according to Eq. (2.21). As Section 4.4 shows, this corresponds well with the experimentally achieved values of resolution.

The problem of limited resolution is not a problem of limited channel number but of strongly overlapping ASFs of adjacent channels.

A further advantage of using MLAs for image transfer is the increasing of the overall space bandwidth product of an imaging system, or number of obtainable image pixels, above that of the single microlens. This was not exploited in the presented realizations of APCOs. Because all microlenses in the array were equivalent, they produce identical micro-images – they look at identical object portions. Only the variation of the pinhole positions within the channels allows an extraction of different information from each channel, but always the same micro-image is sampled. The sum of information in the moiré-magnified image is equal to that of the micro-image of the single microlens.

There are several ways of increasing the system's FOV, but their effect on resolution enhancement is different. The FOV of the APCO was extended by a Fresnel lens up to 42°x42°. However, using this approach, an increased FOV did not lead to an increased number of resolvable pixels. The net number of image pixels remains approximately constant because the Fresnel lens increases the acceptance angle the same as it separates the viewing directions of the channels. This is the result of the local curvature and grooves of the Fresnel lens over the channels.

Array of chirped ellipsoidal microlenses for channelwise correction of astigmatism and field curvature. Since each optical channel of the APCO gathers the light for one chief ray angle $\epsilon_{i,j} = \arctan(\Delta p \sqrt{i^2 + j^2}/f)$ only, channelwise correction of astigmatism and field curvature can be performed (see Chapter 3). i,j is the index of the considered channel describing the channel's position within the array with respect to the central channel. By use of Eq. (3.5) and Eq. (3.6) the required radii of curvature are calculated for each microlens. Applying Eq. (3.8) the major and minor axes of the ellipsoidal base for each microlens are calculated. These determine the geometry of the base of the photo resist cylinders to be melted during the reflow process to form the desired anamorphic microlenses. In order to make the major and minor axes of the ellipses channelwise coincide with the tangential and sagittal plane of the channel's

ray bundle, each ellipse has to turned by the angle

$$\vartheta_{i,j} = \arccos\left(\frac{i}{\sqrt{i^2 + j^2}}\right). \tag{4.17}$$

This system is currently under fabrication. It is expected to provide a homogeneous resolution of on-axis quality over the complete FOV.

Array of chirped aspherical off-axis microlens segments.   As discussed in Section 4.2.3, besides simple scaling, increasing the resolvable number of image pixels could be achieved by an additional separation of the viewing directions of the channels without increasing the channel's acceptance angles (increasing of FOV). This is obtained by adding a channel-dependent beam deflection to the microlenses, in more detail, by using arrays of microlens segments where each has a different decentration with respect to the channel origin (Fig. 4.30). Representations of such microlens segments in the simulation software are aspherical microlenses with decentration or free form descriptions as for instance a polynomial surface. Aberration correction for the corresponding viewing direction can simply be implemented in the decentered aspherical or free form surface shape. Technologies for manufacturing of such chirped MLAs, such as laser beam

(a)   (b)
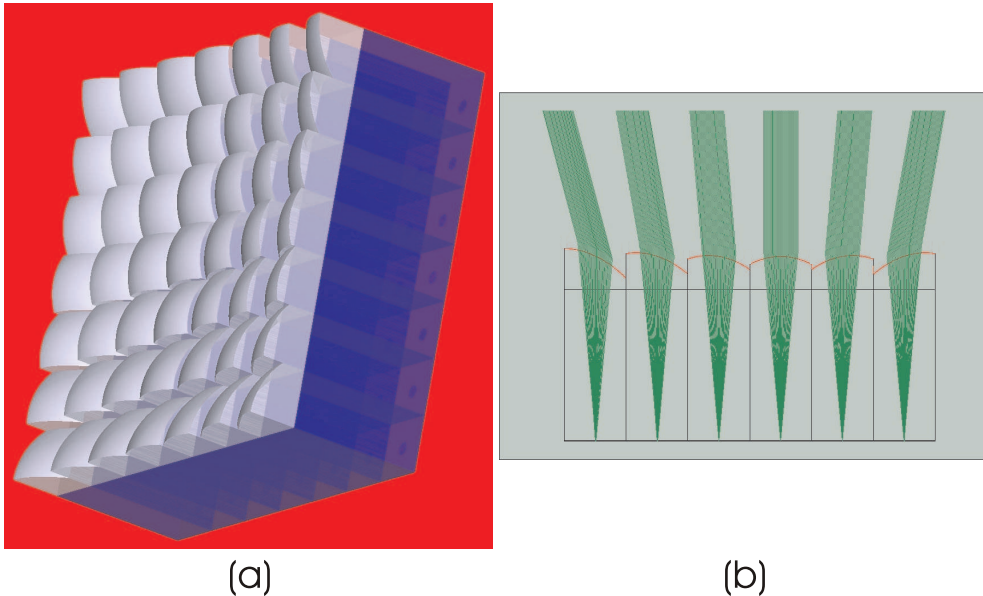
Figure 4.30.   Compound eye objective with chirped MLA. (a) Array of aspherical off-axis microlens segments with channel-dependent decentration within the cell. (b) Each channel's viewing direction is tuned by the microlens segment's decentration. A pitch difference between microlens- and detector array is not necessary. The microlenses are individually corrected with respect to aberrations for their working AOI. Here, the resulting FOV is 30°x30°.

writing, are currently under evaluation.

A combination of a homogeneous refractive MLA with another structure adding a channelwise beam deflection could be an alternative. Necessary structures such as a chirped two-dimensional prism array, two crossed one-dimensional chirped prism arrays or chirped diffractive gratings [214] could be much easier fabricated.

However, increasing the FOV is limited by gracing incidence at the steep prism structures and a reduced size of the projected entrance pupil, which will lead to stronger diffraction effects and a reduced illumination.

The effect of resolution enhancement by using off-axis microlens segments can be completely understood by the above discussion of an additional beam deflection and the enlarged FOV. Alternatively it can be also discussed in terms of the effective image size and of the space bandwidth product. The physical size of the image space behind each microlens is constant, defined by the channel size. As the result of the use of different segments of larger, offset microlenses, a different section of a larger image is actually centered in the small channel. The actual size of the image of a microlens is increased at a constant PSF resulting in an increased resolution.

5 Cluster Eye (CLEY)

A new optical concept for compact digital image acquisition devices for large FOVs is developed and experimentally verified is this chapter [199, 215, 216]. Archetypes for this microoptical telescope compound eye imaging system are natural superposition compound eyes of small insects and the Gabor superlens with the constraint that the different channels are optically isolated (see Section 5.1). The parallel transfer of different parts of an overall FOV (different information) with strong demagnification by separated optical channels allows the CLEY to have a collective space bandwidth product which is equal to the sum of the individual channel's space bandwidth products. Consequently, the CLEY has the potential of much higher resolution than the experimentally demonstrated APCO. Other advantages of using artificial compound eye imaging systems apply in the same way for the CLEY as they do for the APCO. Such advantages are the manufacturing of the objective by microoptics technology due to the small required lens sags and correction of each channel for its central viewing direction.

A full description of such a system has to be based on an analytical model to find all reasonable parameter sets and the fundamental relationships. In Section 5.2 it is reported of the determination and validation of the first order parameters of a CLEY in the one-dimensional case using a paraxial 3x3 matrix formalism. The obtained paraxial parameters are transferred to parameters of real microlenses. A 2mm thin imaging system with 21x3 channels, 70°x10° FOV and 4.5x0.5mm^2 image size is then optimized using sequential raytracing. Non-sequential raytracing analysis is used for the evaluation of ghost images and stray light of the CLEY. It is furthermore examined which sensitivities and resolution can theoretically be obtained with the CLEY. In Sections 5.3 and 5.4, the fabrication and experimental characterization of the telescope compound eye imaging system are discussed.

5.1 Principle – Array of Telescopes with Tilted Optical Axes

Figure 5.1 presents the proposed optical system with no or only a small amount of overlap of the images transferred by different channels but a perfect spatial annexation to the upright overall image in the detector surface. Three MLAs with different pitches form Keplerian telescopes including a field lens- and field aperture array in the intermediate image plane. The arrangement of refracting surfaces is similar to that of a Gabor superlens.

The system can be interpreted as a cluster of single pupil microcameras which have tilted optical axes to obtain a large overall FOV [167]. Each channel images only a small angular section. The widths and positions of the field apertures determine the amount of overlap and spatial annexation of the partial-images. The ratio of focal lengths of the telescope lenses and tilt of the optical axes of the telescopes determine the magnification and image annexation.

Anamorphic microlenses with ellipsoidal lens bases as shown in Fig. 5.2 (b) are used for correction of astigmatism and field curvature under oblique incidence as well as to keep a

constant projected aperture size. As a result of small lens sags, the CLEY is well suited for microoptical fabrication technologies. Fig. 5.2 (c) shows that the proposed approach allows wafer level assembling and packaging.
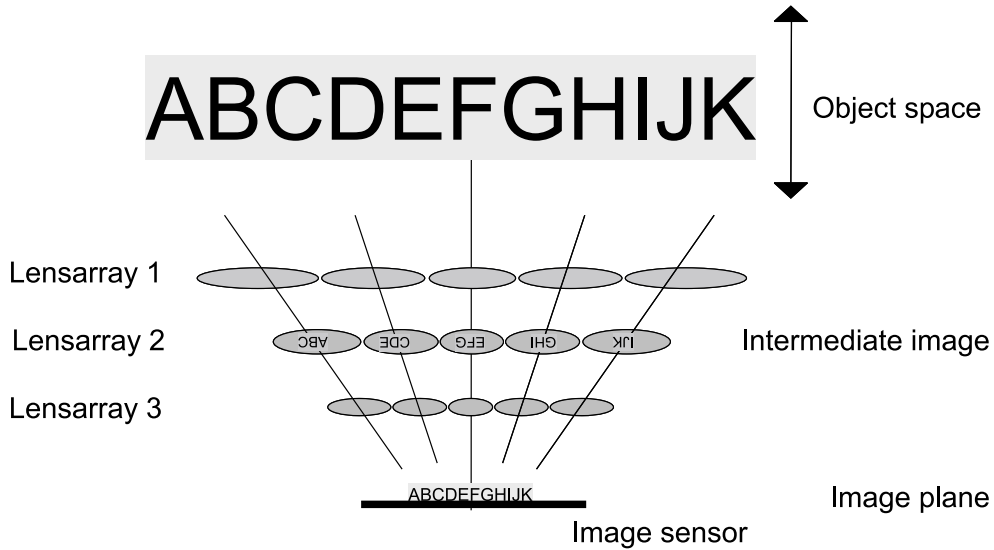
Figure 5.1. Working principle of the telescope compound eye imaging system with optical image reconstruction.
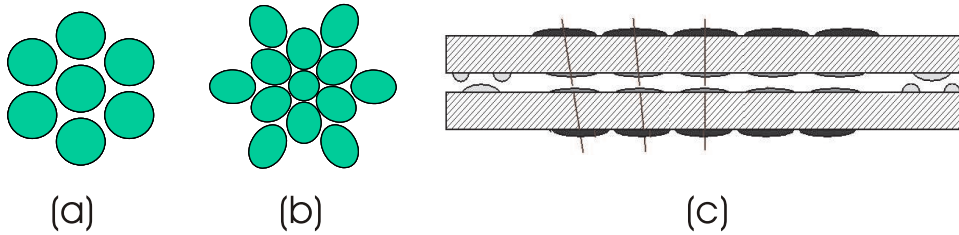
Figure 5.2. Front view of CLEY with hexagonal arrangement of channels. (a) Circular microlenses in array. (b) Anamorphic microlenses with ellipsoidal lens-bases in MLA. (c) Side view of CLEY. Field MLA is partitioned. This arrangement allows wafer scale microlens manufacturing and wafer level packaging for the imaging system. Mechanical alignment structures can be implemented in the MLA fabrication.

5.2 Design and Simulation of CLEY

5.2.1 Paraxial Description

A simplified arrangement as shown in Fig. 5.3 was examined for a basic understanding of the performance of the CLEY.

Three MLAs with different pitches form telescopes with field lenses and tilted optical axes. Each telescope channel transmits a certain part of the overall FOV which is determined by a field stop array in the intermediate image plane at the position of the field MLA. The separately transferred parts of the object superimpose in the image plane to reconstruct the overall image.
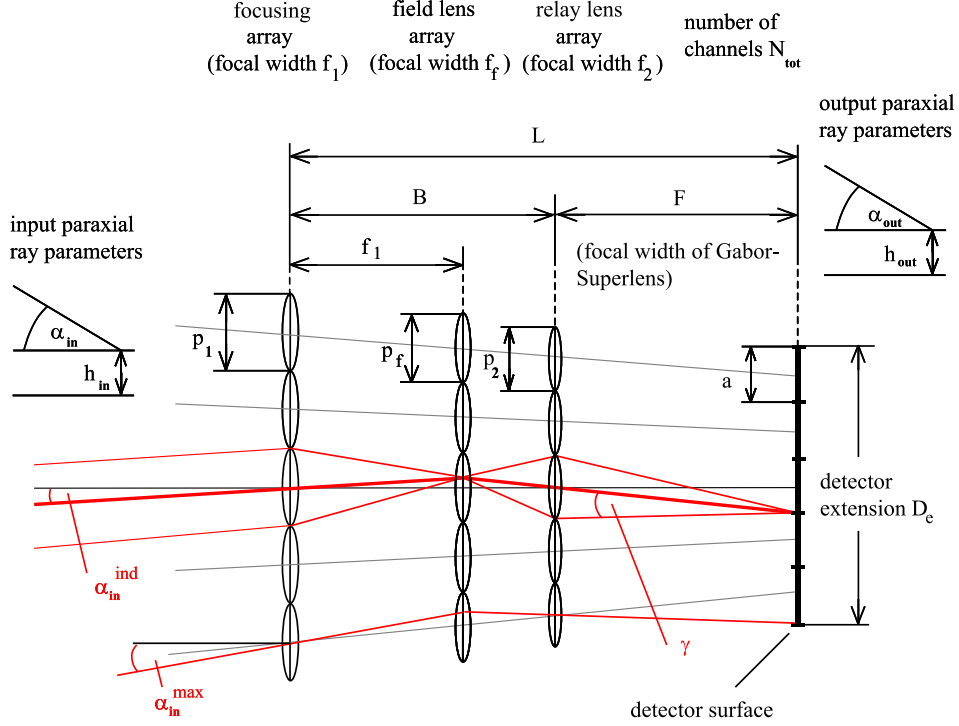
Figure 5.3. Scheme of the paraxial optical model of the CLEY for visualization of the used variables. Input ray vector $(h_{in}, \alpha_{in}, 1)^T$ is transformed to output ray vector $(h_{out}, \alpha_{out}, 1)^T$ by the imaging system's paraxial transfer matrix $\tilde{M}$. ^{T} stands for transposition.

The focusing MLA (pitch p_1, focal length f_1) focuses the light in the intermediate image plane (object assumed to be at infinity). The field MLA (pitch p_f, focal length f_f) is located in the intermediate image plane and redirects all light of the intermediate images into the relaying MLA. The relaying MLA (pitch p_2, focal length f_2) magnifies the intermediate images onto the detector plane. The distance between focusing and relaying MLA is B. The distance from the relaying MLA to the detector surface is F. The total length of the CLEY is determined by L. The total number of channels is N_{tot}. The half angle of the maximum FOV is α_{in}^{max} while the half angle of a channel's FOV is given by α_{in}^{ind}. The paraxial transfer function of the CLEY, $\tilde{M}$, is found by applying the 3x3 matrix formalism presented in Section 2.4:

$$\tilde{M} = \begin{pmatrix} 1 & F & 0 \\ 0 & 1 & 0 \\ 0 & 0 & 1 \end{pmatrix} \begin{pmatrix} 1 & 0 & -Np_1 \\ 0 & 1 & 0 \\ 0 & 0 & 1 \end{pmatrix} \begin{pmatrix} 1 & 0 & 0 \\ -1/f_2 & 1 & N/f_2 \cdot (p_1 - p_2) \\ 0 & 0 & 1 \end{pmatrix} \cdot \ldots$$

$$\cdot \begin{pmatrix} 1 & B - f_1 & 0 \\ 0 & 1 & 0 \\ 0 & 0 & 1 \end{pmatrix} \begin{pmatrix} 1 & 0 & 0 \\ -1/f_f & 1 & N/f_f \cdot (p_1 - p_f) \\ 0 & 0 & 1 \end{pmatrix} \begin{pmatrix} 1 & f_1 & 0 \\ 0 & 1 & 0 \\ 0 & 0 & 1 \end{pmatrix} \begin{pmatrix} 1 & 0 & 0 \\ -1/f_1 & 1 & 0 \\ 0 & 0 & 1 \end{pmatrix} \quad (5.1)$$

where N is the number of the considered telescope channel. The ray offset $-Np_1$ representing the array arrangement of the optical channels can be included at any arbitrary position of the matrix multiplication because all matrices are referred to the same coordinate system within the considered channel – the coordinate system of focusing microlens. Here, the ray offset

67

$-Np_1$ was implemented after the relaying MLA. Thus, it is sufficient to consider just one single channel to this point.

An incident paraxial ray is first refracted by the lens with the focal length f_1. By definition it is then propagated the distance f_1 into the focal plane of the focusing lens where the field lens is situated. As a result of the difference in pitch the paraxial ray is refracted by the laterally shifted field lens (see Eq. (2.34)) with focal length f_f. The lateral shift is given by the product of the pitch difference $p_1 - p_f$ and the channel number of the considered channel N. The center channel has the number zero. After propagation of the distance $B - f_1$ the paraxial ray is refracted by the laterally shifted relaying microlens (focal length f_2 and lateral shift $(p_1 - p_2)N$). The global ray offset of the incident paraxial ray resulting from the array arrangement is applied at this point. Finally the paraxial ray is propagated into the focal plane of the overall lens system where the detector surface is located.

By execution of the multiplications in Eq. (5.1) the simplified form

$$\tilde{M} = \begin{pmatrix} M_{11} & M_{12} & M_{13} \\ M_{21} & M_{22} & M_{23} \\ 0 & 0 & 1 \end{pmatrix} \tag{5.2}$$

is determined, with the matrix elements to be found in Appendix C. Using Eq. (5.2) a number of different conditions are applied to the parameters of the CLEY which guarantee the desired optical performance.

5.2.2 Sets of Equations Determining the Performance of the CLEY

Image forming condition for the individual telescopes. All the telescopes have to have their image plane in the overall detector surface. Consequently, all rays entering the entrance pupil of a telescope under a certain angle must have a common focal plane. This implies that h_{out} must be independent of h_{in}, but only a function of the AOI. It follows $M_{11} = 0$. This is accomplished by

$$F = \frac{f_1 - B}{f_1 + f_2 - B} f_2. \tag{5.3}$$

As expected this is independent of the parameters of the field microlenses.

Gabor condition (superposition condition). The separately transferred partial-images must have perfect connection or overlap in the detector surface to form one regular image. This is achieved if all rays entering different channels under the same angle meet at the same point in the detector plane. This implies that h_{out} must be independent of the channel number N of the considered channel, thus $M_{13} = 0$. It follows that

$$F = \frac{Bp_1 - Bp_f - f_1 p_1 + f_1 p_f - p_1 f_f}{Bp_1 - Bp_f - f_1 p_1 + f_1 p_f - f_2 p_1 + f_2 p_f - p_1 f_f + p_2 f_f} f_2. \tag{5.4}$$

For a system without field microlenses ($f_f = \infty$), the Gabor condition [134] can be derived from Eq. (5.4). This is

$$F = \frac{p_1}{p_1 - p_2} f_2. \tag{5.5}$$

Magnification. The magnification of a telescope channel is determined by the individual channel's FOV $2\alpha_{in}^{ind}$ and the extension of the detector segment a the partial-image has to fill. Using Eq. (5.2) is found that

$$\frac{a}{2} = -M_{12}\alpha_{in}^{ind}. \tag{5.6}$$

For a system without field lenses this simplifies (by the use of Appendix C) to

$$\frac{a}{2} = -\left(F + B - \frac{F}{f_2}B\right)\alpha_{in}^{ind}. \tag{5.7}$$

The magnification m of a channel is determined by the ratio of of the image size and the corresponding FOV

$$m = \frac{a/2}{\alpha_{in}^{ind}} = -\left(F + B - \frac{F}{f_2}B\right). \tag{5.8}$$

Solving Eq. (5.3) for B gives

$$B = \frac{F(f_1 + f_2) - f_1 f_2}{F - f_2}. \tag{5.9}$$

B is substituted in Eq. (5.8) leading to

$$m = \frac{f_1}{f_2}(F - f_2). \tag{5.10}$$

The angular magnification in the CLEY is given by the ratio of focal lengths of focusing microlens, f_1 and relaying microlens, f_2, respectively. The focal length of the Gabor superlens, F, reduced by f_2 determines the resulting spatial magnification. The telescope arrangement, where the ratio of focal lengths of the telescope lenses mainly determines the magnification, provides the difference in magnification compared to a conventional imaging system. In a conventional imaging system, the magnification is only determined by the microlenses' focal length and thus system length. Even for small $F - f_2 \approx F$ a large magnification can be achieved, if only the ratio f_1/f_2 is large enough.

The necessity of using arrays of optical channels instead of only one channel comes up immediately: Short desired focal lengths and a large desired image size would result in too large NAs of the microlenses and strong field aberrations (image size assumed to be similar to channel size). Segmenting the imaging system into many channels having microlenses of reasonable NAs is a well known strategy in microoptical system design [217–219].

In a similar way conditions on segmentation of detector and FOV, $F/\#$ of image formation as well as tilt of optical axes, system length and vignetting (by the use of field lenses) are established in Appendix D.

5.2.3 Determination of the Paraxial Geometrical Parameters

In the previous section it was shown that it is possible to find the primary relationships of the parameters of the CLEY by a paraxial matrix treatment. However, for a full understanding of the optical behavior of the CLEY it is essential to determine its geometrical parameters uncoupled and only as a function of the desired optical system parameters. This is achieved by first solving the equation system consisting of the equations of the CLEY without field lenses for the geometrical parameters. The equation system including the field lenses is solved afterwards.

In Appendix E the list of the paraxial conditional equations of the CLEY is given. The necessary input parameters are D_e (detector extension), α_{in}^{max} (half angle of FOV), γ (half angle of image forming light cone), L (system length) and F (distance from relaying MLA to detector surface). From the resolvability of the equation system follows the free choice of the length F in the input parameters. This is not to be seen as an overall system parameter, but gives a degree of freedom for the design.

By using the Equations (E.1) to (E.13) it is now possible for the first time to determine the influence of the desired optical input parameters on the geometrical parameters p_1, p_f, p_2, f_1, f_f, f_2, B, α_{in}^{ind}, N_{tot}, a, NA$_1$, NA$_f$ and NA$_2$ of the MLAs which build up the CLEY.

5.2.4 Paraxial System, Examples

The paraxial geometrical parameter sets obtained by the formulas of the previous section were implemented as paraxial lens models into a raytracing program. The raytracing verified that the obtained equation system delivers paraxial optical systems which satisfy the desired optical specifications. Table 5.1 gives the major parameters of a calculated paraxial example system using the equations of the previous section. In Appendix F (Tab. F.1) the detailed optical input parameters for the paraxial example system and the calculated paraxial geometrical system parameters using the equations of Section 5.2.3 are presented.

The corresponding paraxial optical system is shown in Fig. 5.4 (a). The tilted optical axes of the telescopes enable a large overall FOV. Each channel is assigned to a portion of the overall FOV. In the paraxial model this is given by the spectrum of input angles for each channel to avoid spurious light or crosstalk for the illustration. In a "real" system, the field stops in the plane of the intermediate image determine a channel's FOV and further baffles in different planes block the spurious light. The maximum marginal field of one channel is the minimum marginal field of the adjacent channel. A perfect annexation of the partial-images to one overall image can be noticed because the same field angle transmitted by two adjacent channels delivers one image point.

Figure 5.4 (b) demonstrates the behavior of this system as a Gabor superlens where all channels contribute to the image point for a given object point if no constraints for the channel's FOVs are given. All field angles are transmitted by all channels.

Table 5.1. Parameters of example systems presented in raytracing simulations and fabricated by microoptics technology.

Parameter	Paraxial example	Circular system with toroidal microlenses	Rectangular arrangement with toroidal microlenses
$F/\#$	2	16	10
Overall length	2mm	1.8mm	1.92mm
FOV (full angle)	70°x15°	27° (diameter)	90°x10°
Detector width	4.5mm	1.5mm (diameter)	4.0x0.5mm^2
Number of channels	column of 5	on diameter: 11 overall: 91	vertical: 25 horizontal: 3

The presented system is non-telecentric. The image space chief ray angle equals the field angle for all image coordinates. But telecentricity may be desired, because perpendicular incidence on the optoelectronic sensor in the image plane for all field angles has many advantages. However, this can not be achieved using a three-microlenses-telescope. An additional MLA is required to provide one more degree of freedom for beam deflection. Furthermore, the relaying MLA must have the same pitch as the image segments to provide a perpendicular incidence for all central chief rays. A splitting of the field lens can be a method to provide this degree of freedom.

A demonstration of the segmented image transfer and overall image superposition / reconstruction in the detector surface is given in Fig. 5.5 for the paraxial example system. A portion of a two-dimensional FOV (Fig. 5.5 (a)) of 70°x70° is imaged by a column of five channels with FOVs of 14.9°x14.9° into the detector surface with the lateral extension of 4.5mm. Each of the letters in the center column of the object (C, H, M, R, W) is separately imaged by the corresponding channel (Fig. 5.5 (b)). The lateral position of the partial-images in the detector surface allows an optical reconstruction of the image (Fig. 5.5 (c)) which fully resembles the corresponding portion of the object.

A further interesting application of the array of microlens telescopes, besides imaging, is the use as a spatial integrator or concentrator. This is introduced in Appendix G.

5.2.5 Considerations to Sensitivity and Equivalent F/# of the CLEY

The sensitivity of an imaging system to an extended source is given by Eq. (2.27) to be only a function of the system's $F/\#$ [28]. The first question to be answered is, if this also holds for a telescope arrangement with the relay of an intermediate image.

Let I_I be the the intensity in the image plane of the focusing microlens. By definition, here the above mentioned relation to the microlenses' $F/\#$ must apply. Let furthermore I'_I be intensity in the image plane of the relaying microlens. From the consideration of energy
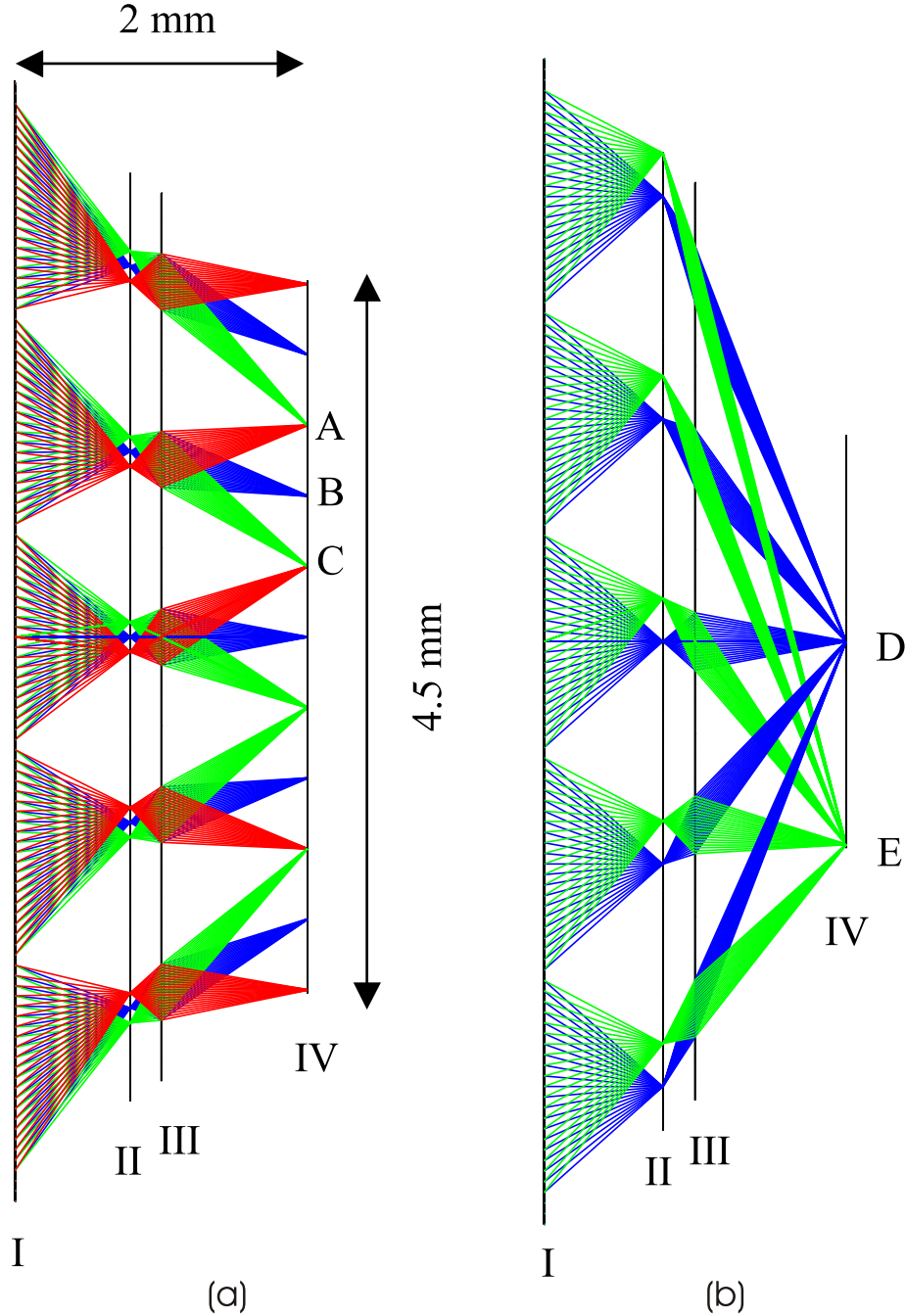
Figure 5.4. Paraxial five channel example system for demonstration of (a) the image transfer by the CLEY principle and (b) behavior like a Gabor superlens. I: Focusing MLA, II: Field MLA, also position of field aperture array, III: Relaying MLA, IV: Image plane. A and C show marginal fields of a channel, B represents the center field. D shows the focus for a field of $0°$, and E for a field of $20°$. In (a) and (b) exactly the same arrangement of MLAs is presented. The only difference is the angular spectrum applied to the imaging system. For modeling the field apertures of the CLEY in (a), each channel is assigned to a portion of the overall FOV, the adjacent channel's FOVs are attached to. In (b) the performance as a Gabor superlens becomes visible because no constraints are set for the channel's FOVs but each channel can transfer the full FOV. Exemplarily AOIs of $0°$ and $20°$ are presented.
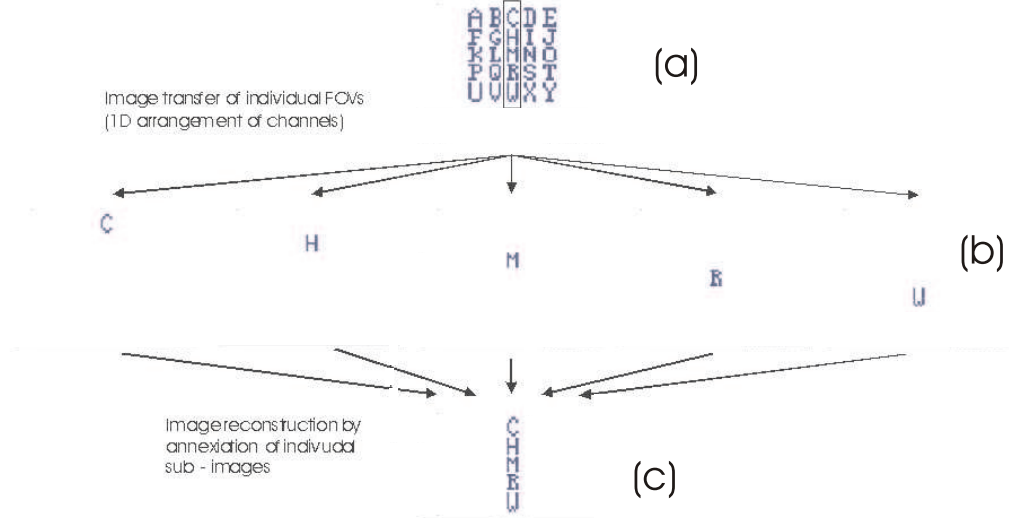
Figure 5.5. Demonstration of the separated transfer of segments of the overall FOV and of the image annexation for the paraxial five channels in the one-column-example-system. (a) Object. (b) Individually transferred partial-images. (c) Optical image reconstruction.

conservation and geometry on similar triangles follows

$$I_I' = I_I \frac{a^2}{a'^2} = I_I \frac{(B - f_1)^2}{F^2} \tag{5.11}$$

where a and a' are the sizes of the image segments in the intermediate image plane and in the final image plane, respectively. $B - f_1$ is the distance from the intermediate image to the relaying microlens and F is the distance from the relaying microlens to the final image plane (see Fig. 5.3). For the intensity of the focusing microlens

$$I_I \propto \frac{D^2}{4f_1^2} \tag{5.12}$$

is obvious. D is the diameter of the focusing microlens. Furthermore the image forming light cone in front of the intermediate image has the same solid angle as after the intermediate image, thus

$$D = D' \frac{f_1}{B - f_1}. \tag{5.13}$$

D' is the diameter of the relaying microlens. Substituting I_I in Eq. (5.11) by Eq. (5.12) and D in Eq. (5.12) by Eq. (5.13) leads to

$$I_I' \propto \frac{D'^2}{4F^2} = \frac{1}{4(F/\#)^2}. \tag{5.14}$$

The sensitivity of the CLEY is only a function of the $F/\#$ in the image forming light cone behind the relaying MLA and this is directly accessible in the equation systems of Sections 5.2.2 and 5.2.3. The segmentation of the CLEY into channels does not reduce the sensitivity.

The second question to be answered is, why only comparatively large $F/\#$s can be achieved for a short CLEY with NAs of the microlenses which are within the fabrication limits and a

competitively large magnification. The key to understand this is in Eq. (5.10). For a large magnification, f_2 must be small compared to f_1 and F must be large. But on the other hand f_1 and F must be small in order to achieve a short system. The diameter of the relaying microlens D' must be small, in order to have a reasonable NA_2 for small f_2. The magnification is independently form the CLEY's segmentation. However, for reasonable NAs of the microlenses with respect to aberrations and manufacturing, the CLEY must be the more segmented, the shorter it is, after Eq. (5.14) leading to large channel $F/\#$s.

Technological constraints and aberrations limit the NAs of reflow microlenses to maximum 0.3-0.4. These are already values using state of the art microoptics technologies. Using this constraint, minimum achievable channel $F/\#$s were calculated as a function of system length using Equations (E.1) to (E.10) to get some impression of the sensitivity capabilities of the CLEY. For all other optical parameters fixed as above, Fig. 5.6 shows the channel $F/\#$ as a function of system length. For fixed magnification and fixed NAs of the microlenses, the channel $F/\#$ increases drastically with a decrease in system length because of stronger necessary segmentation of the CLEY.
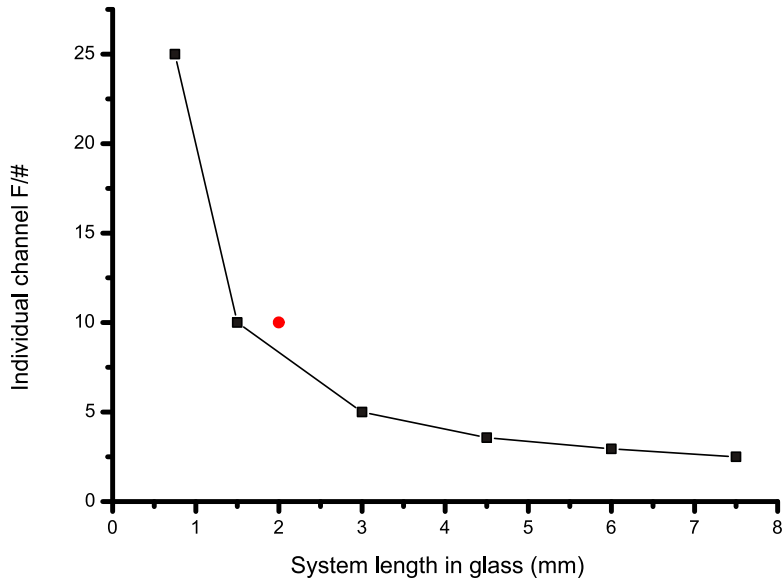

Figure 5.6. Channel $F/\#$ vs. system length for maximum microlens NAs of 0.3-0.4 in case of no image overlap.

The rectangular arrangement of toroidal microlenses presented in Section 5.2.7 makes use of microlenses with maximum NA of 0.2 in order to reduce aberrations. Thus the corresponding value of length vs. $F/\#$, (2,10), for this system is situated above the presented curve in Fig. 5.6.

The possible shortness of CLEY systems which classical optics with the same magnification could never reach, has to be paid by an increased $F/\#$.

5.2.6 Transfer of Paraxial Lens Array Parameters to Chirped Real MLAs

The calculated paraxial geometrical parameters serve only as starting values for the layout of a system consisting of real MLA telescopes. When transferring the paraxial lens parameters to those of real microlenses, focal widths and apertures are a function of the main field angles (tilt of the optical axis) of the considered channel. Off-axis aberrations such as astigmatism and field curvature are minimized. The reduction of the light flux through the projected aperture is partially compensated. Anamorphic microlenses with different radii of curvature and lens sizes as a function of the channel number are established (see Chapter 3).

From raytracing simulations and third order aberration theory [178] it is derived that the focal widths of the microlenses must approximately change with $1/\cos^2(2\alpha_{in}^{ind})$ in the direction where the field angle is increased and with $1/\cos(2\alpha_{in}^{ind})$ in the perpendicular direction in order to keep the image surface of each channel at the position of the detector surface. In order to minimize the dependence of the light flux on field angle, the microlens aperture is changing with $1/\cos(2\alpha_{in}^{ind})$ in direction of increasing field angle. Figure 5.7 demonstrates the described change of focal widths and apertures. A factor $1/\cos(2\alpha_{in}^{ind})$ in all above factors of the chirp of the focal widths is the result of the projection of the tilted optical axis of the considered channel onto the overall optical axis needing to be constant.
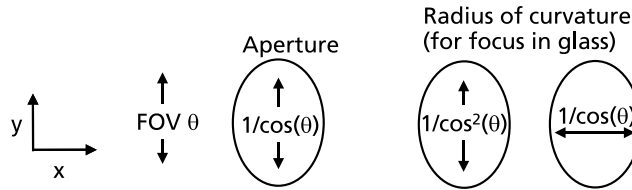

Figure 5.7. Correction for astigmatism, field curvature and conservation of projected aperture size for large AOI. This leads to anamorphic microlenses where the ratios of curvatures and lens-base-widths in the different directions depend on the tilt of the optical axis of the considered channel $\theta = 2\alpha_{in}^{ind}$.

As a result of the change in pitch, the decentration of corresponding microlenses changes with $1/\cos(2\alpha_{in}^{ind})$. But the focal widths of the microlenses on the axis of the considered channel also change with $1/\cos(2\alpha_{in}^{ind})$ for tilted optical axes. Consequently the deflection angle, which is the ratio of decentration and focal width, remains constant.

5.2.7 Simulation of Imaging Systems with Real Microlenses

For validation of the paraxial design strategy and the recipe for the channel-dependent transfer of the paraxial lens parameters to toroidal microlenses, two optical systems were simulated by raytracing. The major optical parameters are listed in Tab. 5.1. In Appendix F (Tab. F.1) the detailed optical input parameters for of the paraxial starting system and the calculated paraxial geometrical system parameters using the equations of Section 5.2.3 are given. For these sets of parameters, NAs of the microlenses were obtained which are still within the fabrication limits and result in a good field performance.

These paraxial system parameters serve as the starting values for imaging systems consisting of real microlenses on substrates, which are further optimized by real raytracing optimization. In the paraxial calculation, the system length must be chosen approximately a factor $1/1.5$ shorter than the required real system length. The real system consists of real microlenses on glass substrates of refractive index of approximately $n' = 1.5$. The glass in the optical path makes the system a factor 1.5 thicker. This must be retarded for.

Rotational symmetric system. A CLEY with real microlenses in a circular arrangement was analyzed using raytracing to verify the two-dimensional imaging capabilities (Fig. 5.8). The system's general parameters are listed in Tab. 5.1.
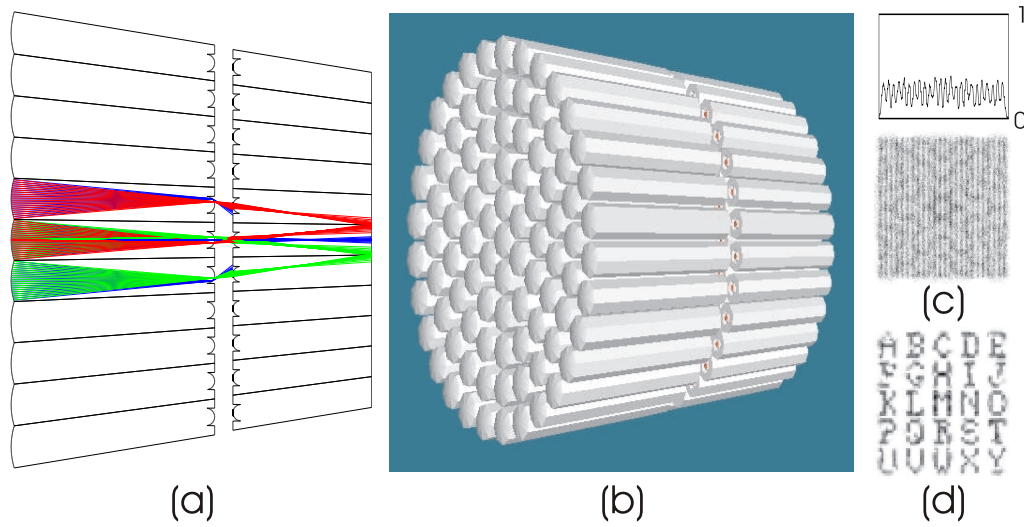

Figure 5.8. CLEY in a circular arrangement of toroidal microlenses. (a) Cross section of layout. The focusing MLA and field MLA are on two sides of the same substrate. The relaying MLA is on the front side of a second substrate on whose backside the image plane is situated. Field angles $0°$, and $±1.3°$ are traced. For the marginal fields, the overlap in the image plane of bundles of same the AOI, transmitted by adjacent channels can be observed. (b) 3D layout-plot visualizing the circular arrangement of the three MLAs. (c) Sample object (25LP) imaged by the CLEY. A pattern with $0.9LP/°$ can still be resolved with sufficient modulation using this arrangement. Undesired overlap of adjacent partial-images can be recognized as an overlaying structure related to the channel distribution. (d) Sample object (alphabet) imaged by the CLEY. Pixel size in image space is chosen to match the size of the diffraction limited spot. Image transfer through a segmented imaging system and formation of one overall two-dimensional image using realistic microlenses is validated.

System of 21x3 channels. A CLEY in a cartesian arrangement of channels was optimized and analyzed using raytracing simulation. This layout was later fabricated by microoptics technology. The fundamental parameters are shown in Tab. 5.1. Only 21 rows of the 25 rows which resulted from the paraxial calculation are further evaluated. After real raytracing

optimization this resulted in a FOV of 70°x10° and an overall image size of 4.5x0.5mm² at a system length of 1.92mm.

The optimization results of sequential raytracing, where each channel is treated in a separate configuration, for $\lambda = 550$nm and microlenses with spherical curvatures are presented in Fig. 5.9 and Fig. 5.10. Lens curvatures in x- and y-direction as well as lens positions and image sizes were optimized to obtain minimum spot size and good image annexation. Using anamorphic lenses for the focusing MLA, astigmatism and field curvature could be minimized to large extend but coma is still present. Lenses of the field MLA and relaying MLA are circular and transmit offset from the microlens vertex. The center chief ray consequently has perpendicular incidence on the corresponding microlens, there are few off-axis aberrations added.

Only a small increase of the geometrical spot size can be observed within the entire array, for the central field of each channel. But for marginal fields of each channel, large aberrations are introduced. This leads to large spots for the marginal fields of channels at the rim of the array. As can be seen from Fig. 5.10 the image superposition works quite well for the central channels but as a result of large aberrations for marginal channel's marginal fields, adjacent fields do not overlap perfectly anymore. However, the alignment of the partial-images is sufficient to form one regular image, but resolution suffers at the positions of image stitching. The magnification is sufficiently kept constant for all channels.

Because of the large channel $F/\#$, the Airy disk diameter is in the magnitude of 10μm to 15μm and the system sensitivity is comparatively low.

Sequential raytracing treatment of the CLEY in a multi-configuration model is sufficient to optimize each channel's parameters individually in order to achieve the desired imaging properties. It is, however, not possible to observe any effect of interaction between channels, because all channels are treated completely separately in different configurations. A non-sequential raytracing analysis of this imaging system is presented in Appendix H. The optical interconnection between channels and thus, the influence of light which passes from one channel to another and/or is reflected at the metal apertures of the microlenses, is analyzed. The resulting effects are ghost images and represent an increased background as a result of stray light. The problem of spurious- or ghost light is partly solved by aperture arrays placed on the focusing MLAs with openings of the size of the microlenses, in the plane of the field MLA (field stop array – rectangular) and the relaying MLA. These aperture arrays shall block all undesired light. At least all spurious light which reaches the detector has to be sufficiently out of focus to be distinguished from a real signal. From the simulation in Appendix H, spurious light appears not to be dominant. An additional aperture layer was found to be helpful to block cross talk through different channel's apertures. Apertures must be placed on the front side of S2 (see Fig. 5.9). However, this can not be considered for the fabrication run discussed in Section 5.3.
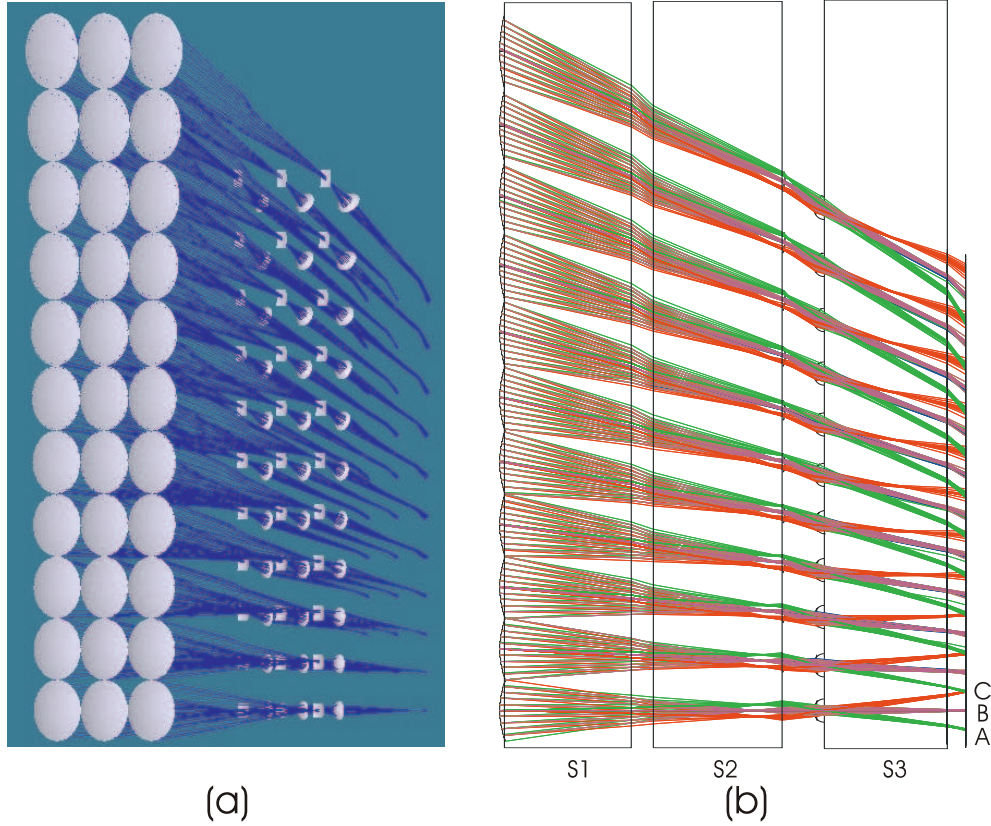
(a)　　　　　　　　(b)

Figure 5.9. CLEY in a rectangular arrangement of toroidal microlenses in a matrix of 21x3 channels. Only channel rows 0 to 10 are shown due to the y-symmetry of the system. (a) 3D view of the system showing the increasing ellipticity of the microlenses in the focusing array with increasing field angle. Substrates are hidden. Only central field angle is traced. (b) Side view of the system. Three MLAs are placed on 550μm thick quartz glass substrates S1, S2, S3 (focusing array consists of toroidal microlenses). Microlenses and apertures are placed on the front side of S1, backside of S2 and front side of S3. For each channel the central field as well as the y-marginal fields are shown. The maximum marginal field of one channel equals the minimum marginal field of the adjacent channel. A perfect annexation of the partial-images to one regular image can be noticed because the same field angle transmitted by two adjacent channels delivers one image point. A, C and B indicate the positions of the marginal and the central field, respectively, of the central channel in the image plane.

5.3 Fabrication of CLEY with 21x3 Channels

A CLEY with 21x3 optical channels was fabricated by microoptics technology. The microlens shapes are defined by reflow of photo resist cylinders on varying (ellipsoidal) bases [194]. The microlenses are subsequently transferred into fused silica by reactive ion etching [220, 221]. Arrays of apertures with ellipsoidal (focusing array), rectangular (field MLA) and circular openings (relaying MLA) are applied onto the corresponding MLAs by chromium etching or lift-off. Finally, the three MLA wafers are stacked in a modified SUSS mask aligner MA8/BA6 with active control of axial distances, wedge error compensation and lateral alignment using
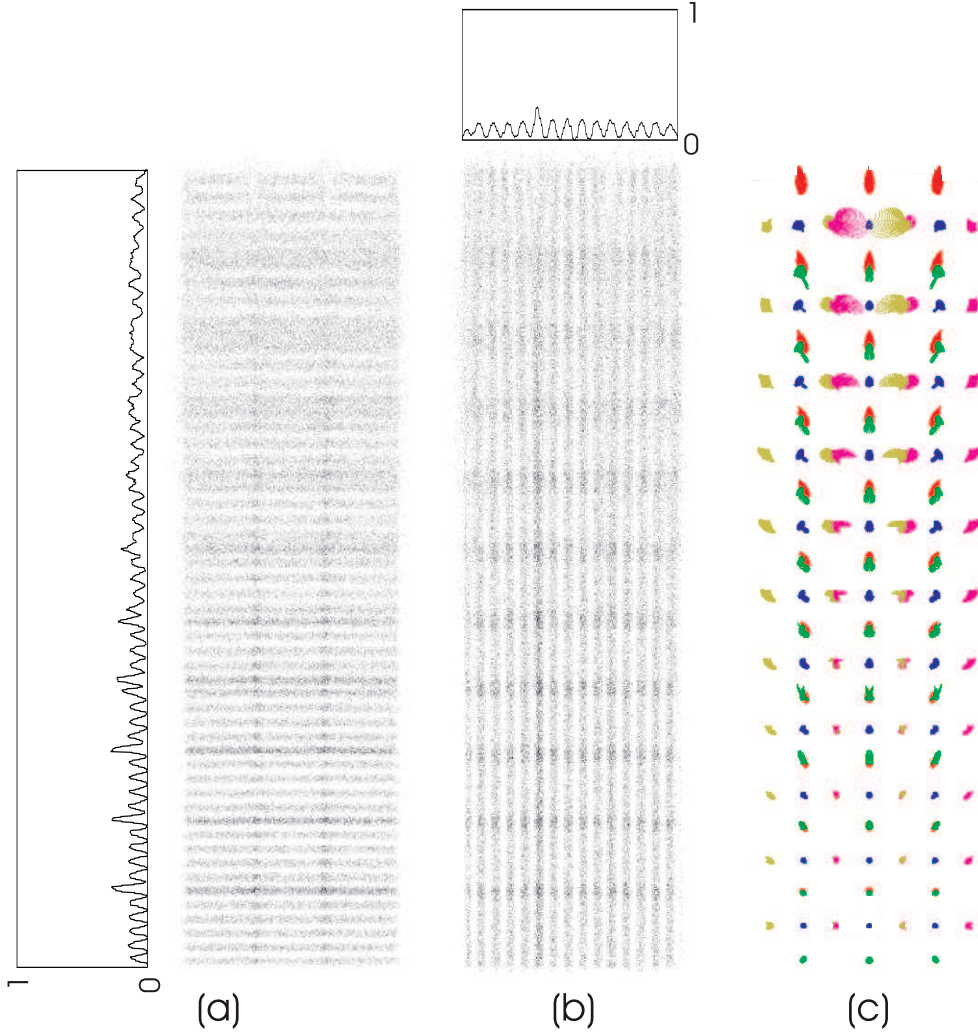
Figure 5.10. Analysis of system presented in Fig. 5.9. Only field angles from -1.8° to 35° are shown due to y-symmetry. (a) Horizontal and (b) vertical sample objects with 1.2LP/° are imaged by the CLEY. The resolution of the patterns decreases with increasing y-field angle because of aberrations and image overlap. However, even for large field angles the line patterns can be resolved. (c) Spot diagram of the presented system. For each channel a central and 4 marginal field bundles (+x,-x,+y,-y) are traced. Increasing spot size with y-field because of coma as well as sufficient overlap of marginal fields of adjacent channels can be observed.

appropriate marks. The principle arrangement of the realized CLEY is given in Fig. 5.11.

The major issue of the MLA fabrication by reflow process is the predetermination of the microlens shape by the resist height and the shape of the lens-base within the used parameter space [193]. As experiments showed (Chapter 3), the microlens height is approximately constant for a variation of the resist cylinder base within a certain accuracy [199], thus the radius of curvature of the microlens is just given by the size of the lens-base according to Eq. (3.7). By using Eq. (3.8), the desired change of radii of curvature is tuned from channel to channel. Table 5.2 summarizes the ideal parameters of the three MLA layers.

After the RIE transfer of the photo resist profiles into fused silica the MLAs were first
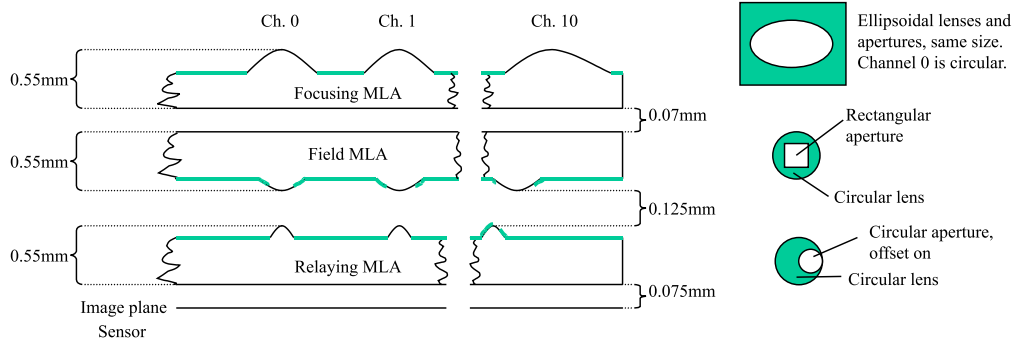
Figure 5.11. Scheme of experimentally realized CLEY. The focusing MLA includes ellipsoidal microlenses. The field MLA and the relaying MLA consist of circular microlenses. Chromium apertures are attached to all MLAs. Rectangular field apertures on the field lenses allow a spatial annexation of the partial-images to one regular image. The design total thickness is 1.92mm.

Table 5.2. Ideal parameters of MLA layers of CLEY. Microlens heights, full sizes of lens-bases, radii of curvatures of microlenses and sizes of apertures are given for center channel (0) and for marginal channel (10). Units are μm.

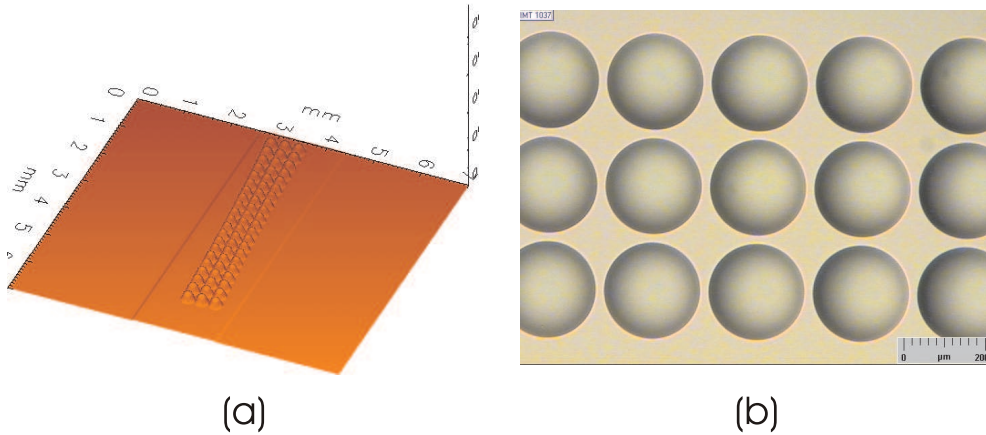| Parameter	Focusing	Ap.	Field	Ap.	Relaying	Ap.
Microlens height	20.2		8.0		41.0	
Size (0)	255	255	73.2	62x57	111.2	80x60
Radius (0)	375.2		87.7		58.3	
Size (10)	311.2x277.8	311.2x277.8	231.8	68x51	119.8	80x90
Radius (10)	609.4x487.9		213.8		64.2	

Figure 5.12. Fabricated focusing array. (a) 3D height profile. Measured by Jurca optical profiling instrument (Type: Jurca Microprof). (b) Photograph of the central section.

characterized with respect to general layout (Fig. 5.12 (a)) and visually inspected with respect to surface quality (Fig. 5.12 (b)).

A critical task in fabrication was to determine the experimentally obtained radii of curvature and deviations of the cross sections of the ellipsoidal lenses from circles in order to find best combinations of fabricated samples of all three layers. The MLAs were analyzed by a mechanical

stylus instrument which was moved on paths crossing all microlens vertices of the corresponding row or column (Fig. 5.13).
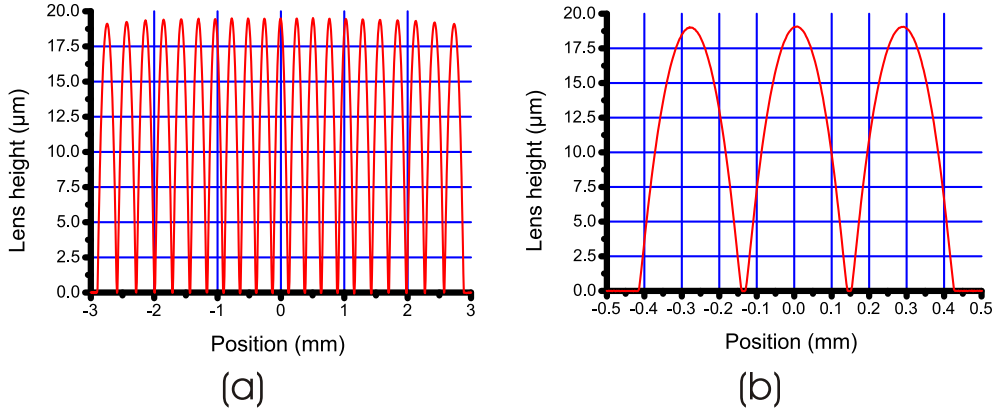

(a)   (b)

Figure 5.13. Cross sections of MLA profiles of focusing array measured using a Rank Taylor Hobson mechanical profiling instrument (Type: FormTalysurf PGI+). (a) Central column with 21 channels. (b) Marginal row of 3 channels.

Figure 5.14 demonstrates exemplarily the measured radii of curvature of the focusing array (ellipsoidal microlenses) in comparison to the ideal values. The deviation of the microlens cross sections from a sphere is always below 90nm (RMS). The radius error is below 2%.
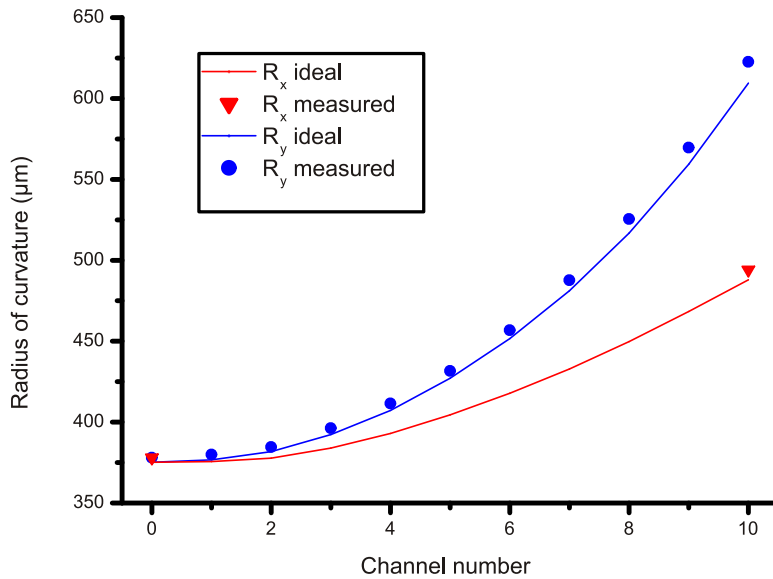
Figure 5.14. Comparison of ideal and experimentally obtained radii of curvatures of ellipsoidal microlenses of focusing array.

The best combination of fabricated MLAs taking into account lens fabrication errors was found by implementing the measured microlens data into the raytracing and optimization software ZEMAX^{TM} and starting a redesign. The degree of freedom left to achieve optimum performance are the axial distances between the arrays defined by the glue thicknesses.

Tolerances for lateral and axial alignment of the different substrates when stacking in the SUSS alignment system are better than $\pm 2\mu$m and $\pm 2.5\mu$m, respectively.

81

5.4 Experimental Characterization of CLEY

Test patterns were presented to the realized CLEY and the overall image was relayed onto a conventional CCD camera by a microscope objective with a magnification of x5 and NA 0.18.

The image annexation of all the partial-images can be observed by imaging a white surface, because one smooth white image should be generated. Figure 5.15 demonstrates that a perfect image stitching could not be obtained with this first demonstrator. Either the partial-images are of roughly rectangular shape but do not connect to each other (Fig. 5.15 (a)) or they connect only in some portions (Fig. 5.15 (b)) or have strong overlap in others (Fig. 5.15 (c)). This causes a considerable intensity modulation even for a smooth white object. Analyzing the
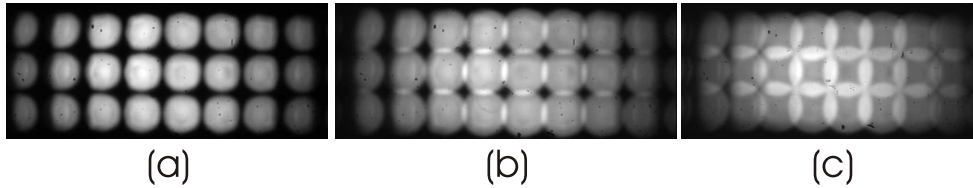

Figure 5.15. Image of a white surface. (a), (b) and (c) show the same image produced by the CLEY but with different axial positions of the relay optics (distance of 120μm with respect to each other).

quality of the field apertures, it was observed that they are not exactly rectangularly due to fabrication problems as can be seen in Fig. 5.16.
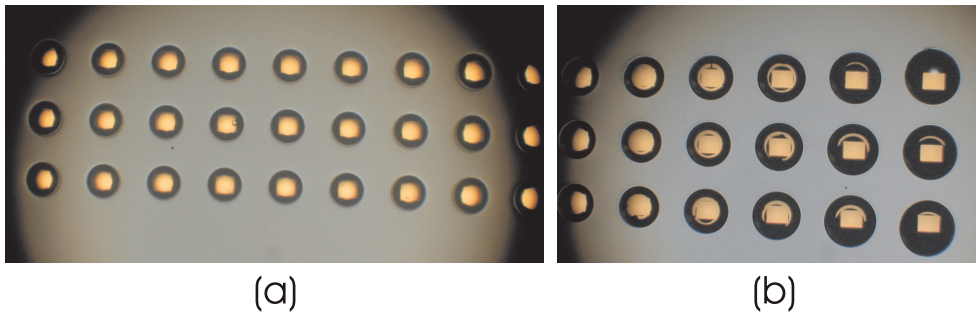
Figure 5.16. Microscope image of field MLA with applied field apertures. (a) Center channels. (b) Marginal channels.

Due the non-telecentric behavior of the CLEY and the limited NA of the relaying microscope objective, the transmitted field angles are restricted and only a limited number of channels can be observed. However, with the central 8x3 channels the following images were captured.

Figure 5.17 shows the images of a radial star pattern, captured at different axial positions from the CLEY. It can be observed that the matching of the image plane of the individual telescopes with the position of the perfect annexation of the partial-images is particularly critical. This is mainly influenced by the correspondence of the axial position of the intermediate images with the position of the field apertures. The poor quality of the produced field apertures is considered to be less important.

Tolerances of MLA fabrication and assembly are very tight (in the μm order of magnitude)

(a)   (b)

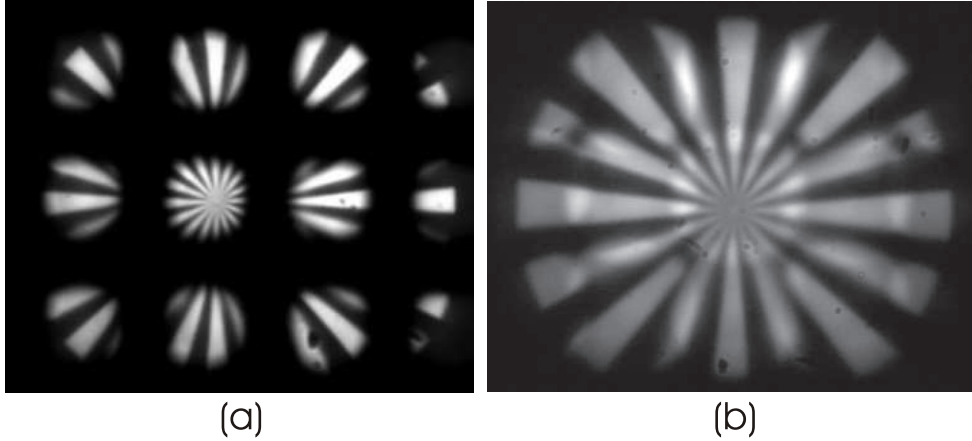**Figure 5.17.** Images of a radial star test pattern at an object distance of 41cm. (Here 5x3 channels are contributing.) (a) At a certain distance from the CLEY, the partial-images have high contrast but are separated from each other. (b) When moving the image plane 120μm further away from the CLEY, all the partial-images exhibit a very good annexation with only minor areas of overlap or lack of annexation. One regular image is generated by transfer of the different image section through separate channels. However, the contrast of the partial-images is reduced compared to (a) because the image plane of the telescopes is slightly defocused.

and there are no compensation possibilities without reducing either contrast of the partial-images or degrading the image stitching.

However, it is demonstrated that one overall image is generated by the transfer of the different image section through separated channels with a strong demagnification. Each channel has a FOV of 4.1°x4.1°, the size of the partial-images is 192x192μm^2. This results in a magnification with an equivalent focal length of 2.75mm at a system length of the realized CLEY of only 1.99mm equivalent to a telephoto ratio of 1.4.

In Fig. 5.18, images of bar targets of different spatial frequencies are presented. Over a FOV of 33°x12°, a resolution of 3.3LP/° is achieved. Problems of image stitching and aberrations of each channel's marginal field angles can be observed in Fig. 5.18 (b) and (c). Bar targets which are oriented parallel to the transition between channels loose modulation in the transition area, while bar targets, which are perpendicular to the direction of transition are still visible in the transition area. This is the result of a slight offset of the images in the direction of transition between images and the asymmetrical form of the geometrical spots. This is caused by the off-axis aberrations of each channel's marginal fields.

Bar targets of different spatial frequencies, such as in Fig. 5.18, were imaged for a quantitative MTF determination. Each SFR was calculated after Eq. (4.13). Test patterns with frequencies up to 14LP/channel can be imaged with at least 10% modulation (patterns of Fig. 5.18 (b), (c)). This is equivalent to a maximum resolution of 71LP/mm or 3.3LP/° at 10% modulation.

Finally, images of different test patterns visualizing the optical performance of the CLEY are presented in Fig. 5.20. Distant text and faces can be resolved.

(a)

(b)   (c)
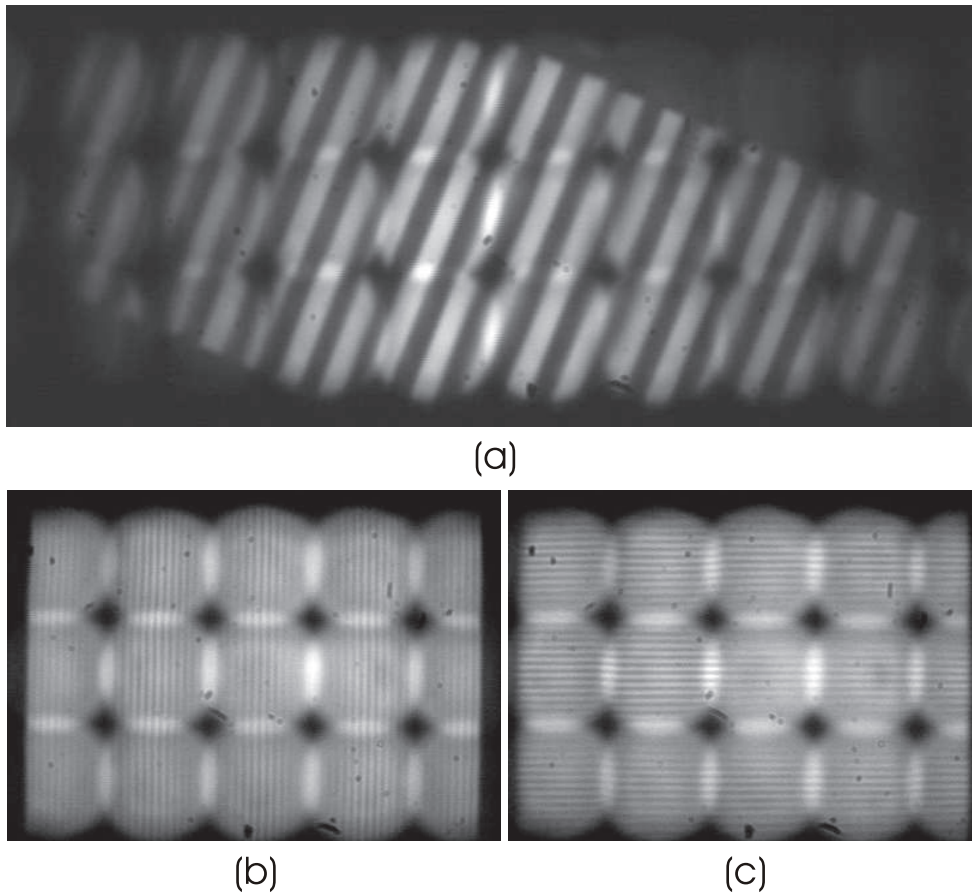
Figure 5.18. Imaged bar targets. (a) Tilted bar target with a period of 8.8mm/LP and a height of 7cm at a distance of 55cm. A good image annexation can be observed, the edges of the bars are imaged sharply. (b) Image of vertical test pattern at a distance of 41cm and size of 13.5cm, demonstrating the maximum resolution of the CLEY. (c) The same resolution is achieved imaging a horizontal test pattern.
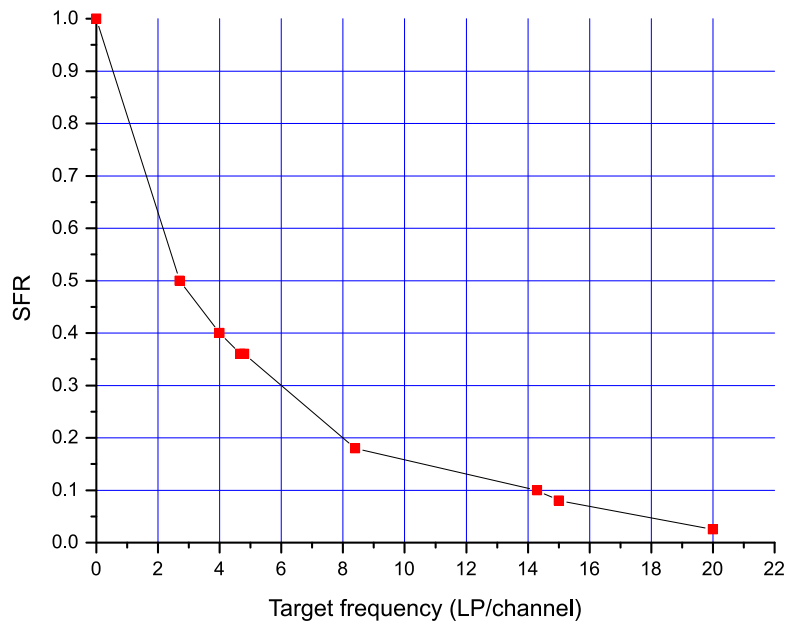

Figure 5.19. Measured MTF of fabricated CLEY.

(a)

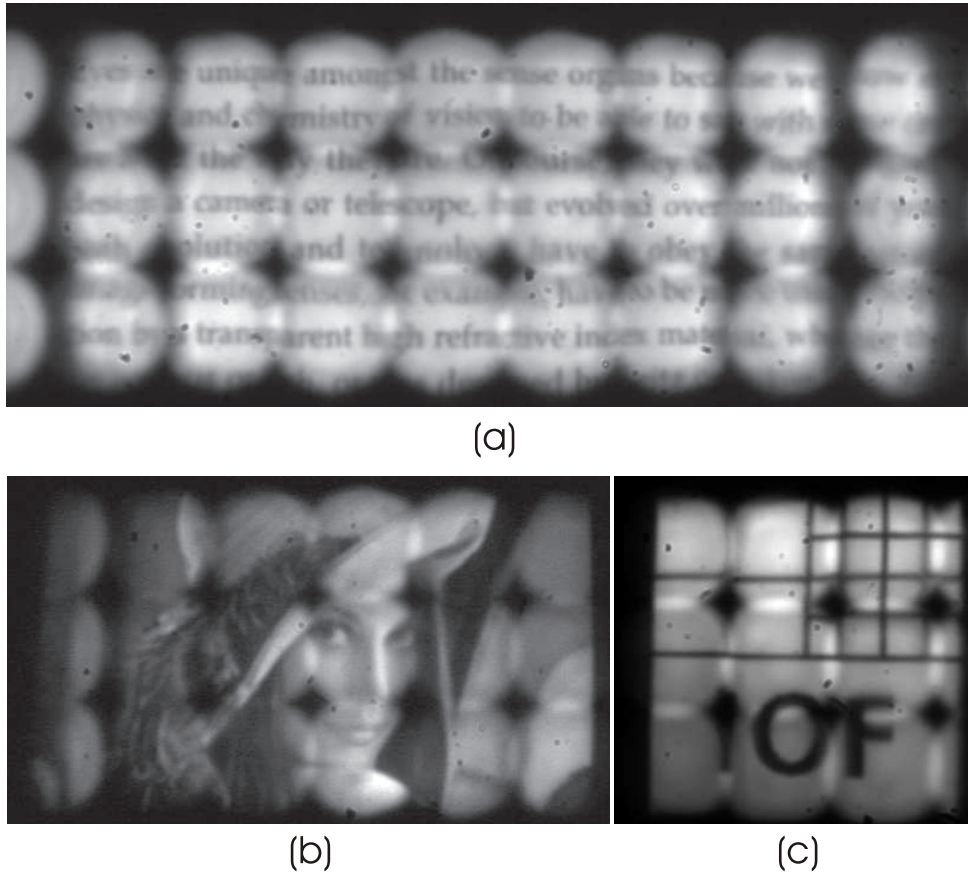(b)   (c)

Figure 5.20. Experimental demonstration of the imaging capabilities of the CLEY. (a) Image of a text section of M. F. Land's book "Animal Eyes", Section 3: "What makes a good eye" [1] with size 10x3.7cm^2 at a distance of 17cm. (b) Image of a picture of "Image processing Lena". (c) Image of the IOF institute logo. Sharp edges and small resolved image features demonstrate the promising imaging capabilities of the CLEY.

Introducing a thin ground diffusing glass in the image plane of the CLEY, the relayed image becomes more coarse but is still visible (Fig. 5.21 (a)) and larger FOVs can be relayed.

The whole image plane of the CLEY is now relayed using a C-mount objective instead of a microscope objective. The functionality of the CLEY for objects filling almost the design FOV is shown in Fig. 5.21 (b) and (c).

5.5 Summary and Conclusions on CLEY

A novel imaging principle based on artificial compound eye vision for large FOVs was designed, fabricated by microoptics technology, and the performance was experimentally demonstrated for the first time. The optical channels have optical axes that are tilted with respect to each other. Each channel images only a small section of the object, which combine to one regular image. A paraxial 3x3 matrix formalism was used to describe the telescope arrangement of three MLAs with different pitches, to find the first order parameters of the imaging system. As to the geometrical arrangement of the microlenses, the CLEY is similar to a Gabor superlens.
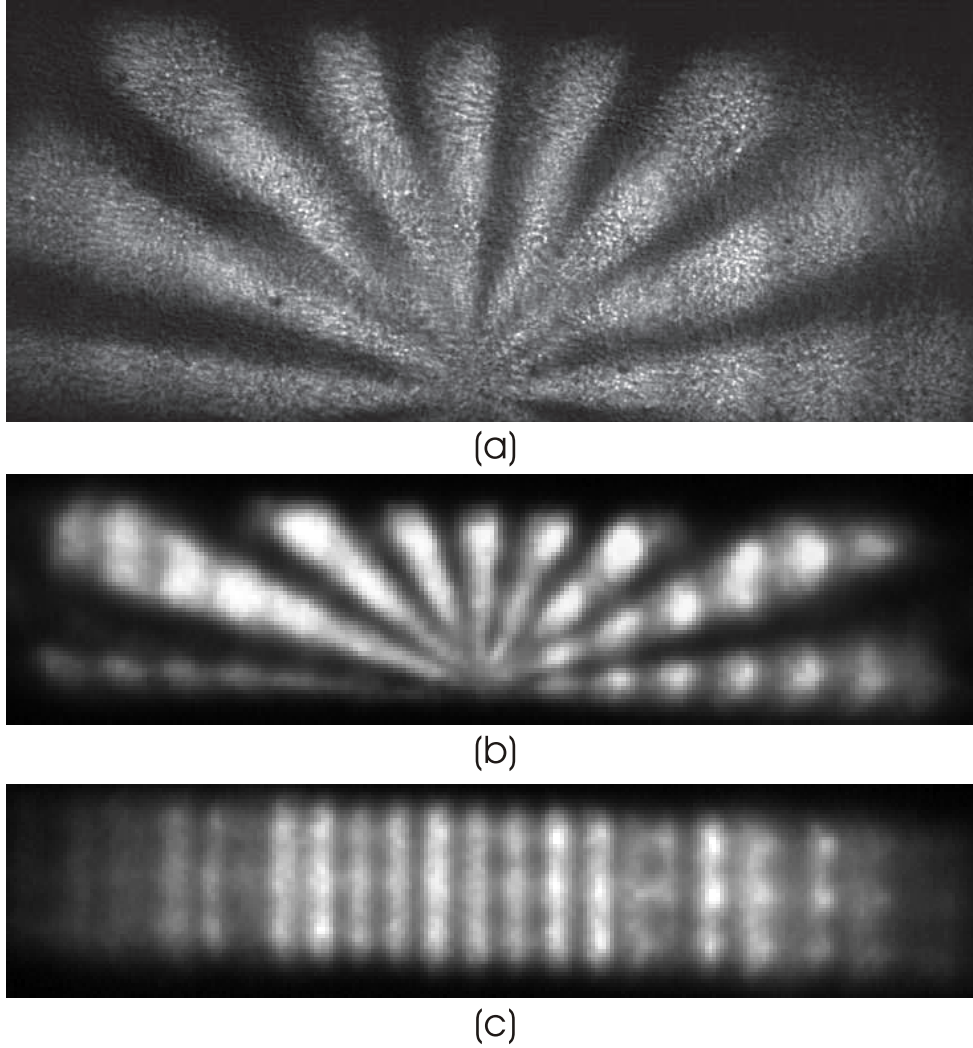
Figure 5.21. Ground diffusing glass introduced in image plane of CLEY. (a) Relay by microscope objective (8x3 channels observed, imaging a section of a radial star pattern). (b) C-mount objective (f=16mm, $F/\# = 1.4$, with extension rings) used for relay of image of a radial star pattern formed by the CLEY. A horizontal FOV of 63° can be observed. 16x3 channels contribute. (c) A bar target with period 3°/LP is imaged by the CLEY onto the diffusing glass and relayed by the C-mount objective onto the CCD. 21LPs can be observed resulting in a FOV of 63°. The resolution is degraded for the outer channels.

However, the superposition of light beams transferred by different channels is prevented by field apertures in the intermediate image plane. The magnification of the CLEY is not determined by the focal length as in the conventional single channel imaging principle but mainly by the ratio of focal lengths in the array of microtelescopes.

A 2mm thin imaging system with 21x3 channels, 70°x10° FOV and 4.5x0.5mm^2 image size was designed, optimized and analyzed by sequential raytracing simulation and also analyzed by non-sequential raytracing simulation. A trade-off between system length, channel $F/\#$ and microlens NAs was derived. The system was fabricated using microoptics technology. Anamorphic microlenses with channel-dependent parameters are used to achieve a homogeneous optical

performance over the whole FOV. The functionality of 16x3 optical channels having a horizontal FOV of 63° was experimentally demonstrated. The resolution of the central channels was experimentally determined to be 3.3LP/° (equal to 71LP/mm). The applied design formalism was consequently verified.

The experimentally obtained resolution is larger than the one which was tested for in the raytracing simulations (image analysis). This is a result of raytracing of a "multi-configuration" where most of the traced rays, do not actually contribute to the image formation. The experimentally obtained resolution, however, corresponds well to the resolution expected from the system's $F/\#$ together with Eq. (2.16).

Correct image stitching has been identified to be the critical issue. Image stitching is partly controlled by the quality of the field apertures and, most important, by the accordance of the axial position of the intermediate images with the position of the field apertures. This shall be considered more rigorously in future designs.

The problem of highly accurate image stitching can be relaxed in the future designs by the application of so called "soft apertures", where the transmission changes continuously from one to zero. An overlap of the partial-images in the overall image plane should not cause undesired modulation anymore, as it currently occurs e.g. for a white target such as in Fig. 5.15 (c).

The complexity of the presented system, compared to other artificial compound eye imaging approaches [202], is much higher. Nevertheless, the telescope compound eye allows for the first time the use of microoptical fabrication technology for a compact imaging system which produces a regular macroscopic image of a far distant object. The spatial information capacity of the CLEY is much higher than that of the artificial APCO because of the transfer of different image segments by separated optical channels (separated viewing directions as a result of tilted optical axes of the telescopes). The CLEY has the potential to achieve a resolution similar to that of conventional imaging systems.

6 Conclusions and Outlook

Two different artificial compound eye concepts for compact vision systems have been investigated in detail: The artificial apposition compound eye objective and the cluster eye. Optical design methods and characterization tools were developed or modified to allow the layout and analysis of the microoptical imaging systems which were fabricated for the first time by microoptics technology.

In contrast to classical single channel imaging systems, the magnification of an artificial apposition compound eye objective is not determined by the microlenses' focal length (and hence by the system length) but by the size and number of channels. An artificial apposition compound eye objective can consequently be realized much shorter than a classical imaging system with the same magnification. For the first time, an objective length of 0.2mm has been demonstrated for an imaging system that as a magnification which is equivalent to a focal length of a single aperture objective of 24mm. This artificial apposition compound eye objective delivers an image with the resolution of 60x60 pixels. Captured images reveal that the obtained resolution is sufficient for a large number of imaging applications.

In this thesis it was shown that the understanding of the behavior of the single channel and its correct layout constitute the key to properly designing an artificial apposition compound eye objective. The arrangement of an array of channels with different viewing directions then follows straightforwardly, but must be matched to the characteristics of the single channel. The angular sensitivity function seems to be the most appropriate method to characterize the single channel, because it contains information about resolution and sensitivity at the same time and can take into account combined effects of detector size, diffraction at the microlens aperture, and aberrations.

The scaling laws of artificial apposition compound eye objectives were established. The sensitivity to an extended source is constant when scaling the system thickness with constant F-number and receptor size. However, the angular resolution is decreased with system miniaturization. The key to increasing the information capacity of artificial apposition compound eye objectives was found to be the separation of the channel's viewing directions not only by pinholes with different amounts of offset in the focal planes of identical microlenses but by an additional, channelwise beam deflection.

Different types of demonstrators of the artificial apposition compound eye objective were designed, fabricated and experimentally characterized for the first time. The master structures for the microlenses were defined by the reflow process. The objectives were fabricated by aligned embossing of the replication tools, with respect to the pinhole array layer, into UV-curing photo polymer – on 4" wafer scale. Opaque walls were introduced in the spacing layer between adjacent optical channels. They prevent ghost images that otherwise arise from cross talk of channels for objects that are outside the imaging system's field of view. This was achieved by lithographic patterning of a high aspect ratio photo polymer.

A second, much more complex, bioinspired microoptics vision system was designed and experimentally validated for the first time: The cluster eye. Also the cluster eye's magnification is not determined by the system length. Instead, the ratio of focal lengths in the array of microtelescopes mainly defines the magnification.

The cluster eye was designed using a paraxial 3x3 matrix formalism and optimized and analyzed by raytracing simulation. It was then fabricated by a reflow technique, subsequent transfer into fused silica by reactive ion etching, metal aperture application and stacking of wafers. For a channelwise correction of off-axis aberrations, the microlenses of the focusing array are of variable ellipsoidal shape.

The experimentally realized device had a thickness of 1.99mm. The functionality of 16x3 optical channels having a horizontal FOV of 63° was experimentally demonstrated. The resolution of the central 5x3 channels was experimentally determined to be 3.3LP/° (LP means line pair). The matching of the image plane of the telescopes with the position of the perfect annexation of the partial-images appears to be particularly critical. It was verified that one regular image is generated by the transfer of the different image sections through different channels, while a strong demagnification occurs. The information capacity can be seen to be much higher than that of the artificial apposition compound eye objective. This is a result of the larger field of view and higher angular resolution at the same time.

The complexity of the cluster eye is much higher as compared with the artificial apposition compound eye objective, and the cluster eye is thicker by a factor of ten. Three wafers of microlens arrays with applied aperture arrays have to be stacked precisely, and there is a high demand on the microlens quality with respect to focal length accuracy. However, this telescope compound eye for the first time allows the use of microoptical fabrication technology for a compact imaging system which produces a regular macroscopic image of a far distant object.

Image transfer by separated channels benefits from the possibility to individually correct each channel for the corresponding viewing direction. Spot size measurements under oblique incidence using spherical and ellipsoidal microlenses showed that a homogeneous resolution over the complete field of view can be achieved with anamorphic microlenses. They enable a channelwise correction of astigmatism and field curvature, which are the main off-axis aberrations for small numerical apertures of the microlenses. These lenses are fabricated by reflow of photo resist on an ellipsoidal base.

The technically achieved resolutions of 1.5LP/° of the artificial apposition compound eye objective and 3.3LP/° for the cluster eye seem rather promising compared to today's standard imaging devices, if the difference in system length of approximately one order of magnitude is taken into account. For comparison: A classical single aperture wide-angle objective with 70° horizontal field of view and a "1 Megapixel" sensor provides an angular resolution of 7.1LP/° if homogeneous resolution over the field of view is assumed. The total track of such a "miniature" single aperture objective is typically in the order of magnitude of 5-10mm. The angular resolution of the demonstrated artificial compound eyes is furthermore comparable to that of

many invertebrate eyes such as e.g. the honey bee (0.5LP/°) or the jumping spider (3-6LP/°). The natural archetypes show: It is not the highest resolution that provides the optical solution capable of surviving for millions of years, but the simplest solution in perfect adaptation to the image capturing task and to the environmental circumstances such as minimum volume, no need for focusing for different object distances, and minimum necessary signal processing.

The space bandwidth product is the limiting factor of the resolution of a miniaturized imaging system, as long as no further deflection is implemented in the optical channels. In the artificial apposition compound eye objective, the resolution of the whole camera is not higher than that of the single microlens. Since identical microlenses are used, all channels image the same part of the object space. Only the extracted image points are different as a result of the difference in pitch of microlens- and detector array. In the cluster eye, there are separated viewing directions of all channels because of the tilted optical axes of the telescopes. The overall objective's spatial information capacity is the sum of the capacity of all channels. This is an optimum array arrangement in terms of space bandwidth product. The realized artificial apposition compound eye objective can be considered as a simple imaging optical sensor while the cluster eye is capable of becoming a real alternative to classical bulk objectives. The proposed future changes in the microlenses of the artificial apposition compound eye objective to segments of differently decentered microlenses could also improve the resolution drastically but will arise a noticeably technological challenge.

In the future, modifications of the technology have to be developed for the field of view and resolution of artificial compound eye imaging systems to be increased, the expensive lithographical process to be replaced by cheap replication, objectives to become mechanically flexible or be directly integrated in the electronics fabrication process. Additional functions which are also provided by the natural archetypes such as color vision, polarization sensitivity and movement detection shall be integrated as well. The combination of microoptical imaging systems with task-specific image processing such as artificial neural networks, which also could be inspired by insect vision, must be investigated.

Finally, comparing the analyzed artificial compound eye concepts with their natural archetypes the following conclusions can be drawn: The major difference at this stage of development is the planar arrangement of the artificial systems compared to the curved geometry of the natural ones. This is the consequence of today's limitation to planar lithographic patterning technologies. The advantages of a curved basis compared to a planar one are obvious: The immanence of a large field of view, avoiding of off-axis aberrations, and avoiding of declining illumination with increasing field angle due to the $\cos^4$-law. Technologies to generate microlens arrays on curved surfaces, e.g. by a special type of laser beam writer, are currently being developed. Optoelectronics on curved surfaces have to be future investigations. A detailed listing of future tasks in order to develop bioinspired microoptical vision from the proof of principle to commercial applications can be found in Appendix I.

Bibliography

[1] M. F. Land and D.-E. Nilsson, *Animal Eyes*, Oxford Animal Biology Series (Oxford University Press, Oxford, 2002).

[2] J. S. Sanders, ed., *Selected Papers on Natural and Artificial Compound Eye Sensors*, SPIE Milestone Series, 122nd ed. (SPIE Optical Engineering Press, Bellingham, 1996).

[3] A. W. Lohmann, "Scaling laws for lens systems," Appl. Opt. **28**(23), 4996–4998 (1989).

[4] R. Völkel, M. Eisner, and K. J. Weible, "Miniaturized imaging systems," Microelectron. Eng. **67-68**, 461–472 (2003).

[5] J. S. Sanders and C. E. Halford, "Design and analysis of apposition compound eye optical sensors," Opt. Eng. **34**(1), 222–235 (1995).

[6] N. Franceschini, J. M. Pichon, and C. Blanes, "From insect vision to robot vision," Phil. Trans. R. Soc. Lond. B **337**, 283–294 (1992).

[7] K. Hamanaka and H. Koshi, "An artificial compound eye using a microlens array and its application to scale-invariant processing," Opt. Rev. **3**(4), 264–268 (1996).

[8] S. Ogata, J. Ishida, and T. Sasano, "Optical sensor array in an artificial compound eye," Opt. Eng. **33**(11), 3649–3655 (1994).

[9] M. F. Land, "The optics of animal eyes," Contemp. Phys. **29**(5), 435–455 (1988).

[10] S. Exner, *Die Physiologie der facettierten Augen von Krebsen und Insecten* (Deuticke, Leipzig, 1891).

[11] M. F. Land, "Animal eyes with mirror optics," in *Sci. Am.*, 6, ed. (126-134, December, 239).

[12] M. F. Land, "Eyes with mirror optics," Pure Appl. Opt. **2**, R44–R50 (2000).

[13] A. W. Snyder, D. G. Stavenga, and S. B. Laughlin, "Spatial Information Capacity of Compound Eyes," J. Comp. Physiol. A **116**, 183–207 (1977).

[14] G. A. Horridge, "Apposition eyes of large diurnal insects as organs adapted to seeing," Proc. R. Soc. Lond. B **207**, 287–309 (1980).

[15] K. G. Goetz, "Die optischen Uebertragungseigenschaften der Komplexaugen von Drosophila," Kybernetik **2**, 215–221 (1965).

[16] M. F. Land, "Compound eyes: old and new optical mechanisms," Nature **287**, 681–686 (1980).

[17] R. Fischer and B. Tadic-Galeb, *Optical System Design* (McGraw-Hill, New York, 2000).

[18] A. W. Snyder, "Physics of Vision in Compound Eyes," in *Handbook of sensory physiology*, 225–313 (Springer, 1977).

[19] A. W. Snyder, "Acuity of Compound Eyes: Physical Limitations and Design," J. Comp. Physiol. A **116**, 161–182 (1977).

[20] R. Wehner, "Pattern recognition," in *The Compound Eye and Vision of Insects*, G. A. Horridge, ed., 75–95 (Clarendon Press, Oxford, 1975).

[21] E. Hecht, *Optik*, 3rd ed. (Addison–Wesley, 1989).

Bibliography

[22] G. A. Horridge, "The separation of visual axes in apposition compound eyes," Phil. Trans. R. Soc. Lond. B **285**, 1–59 (1978).

[23] J. W. Goodman, *Introduction to Fourier Optics* (McGraw–Hill, New York, 1968).

[24] I. N. Bronstein, K. A. Semandjajew, G. Musiol, and H. Mühlig, *Taschenbuch der Mathematik* (H. Deutsch, Frankfurt, 1995).

[25] M. F. Land, "Variations in Structure and Design of Compound Eyes," in *Facets of Vision*, D. Stavenga and R. C. Hardie, eds., chap. 5, 90–111 (Springer, 1989).

[26] G. A. Horridge, "The compound eye of insects," Sci. Am. **237**, 108–120 (1977).

[27] R. McCluney, *Introduction to Radiometry and Photometry* (Artech House, Boston, 1994).

[28] K. Kirschfeld, "The Absolute Sensitivity of Lens and Compound Eyes," Z. Naturforsch. **29**, 592–596 (1974).

[29] R. Kingslake, *Optical System Design* (Academic Press, New York, 1983).

[30] E. J. Warrant and P. D. McIntyre, "Strategies for retinal design in arthropod eyes of low F– number," J. Comp. Physiol. A **168**, 398–411 (1991).

[31] G. A. Horridge, K. Mimura, and R. C. Hardie, "Fly photoreceptors III. Angular sensitivity as a function of wavelength and the limits of resolution," Proc. R. Soc. Lond. B **194**, 151–177 (1976).

[32] H. B. Barlow, "The size of ommatidia in apposition eyes," J. Exp. Biol. **29**, 667–674 (1952).

[33] K. Kirschfeld, "The resolution of lens and compound eyes," Neural Principles in Vision 354–370 (1976).

[34] R. Wehner, "Spatial Vision in Arthropods," in *Comparative Physiology and Evolution of Vision in Invertebrates - Handbook of Sensory Physiology*, H. Autrum, ed., **VII/6C**, chap. 4, 287–317, 551–616 (Springer, Berlin-Heidelberg, 1981).

[35] H. Naumann and G. Schröder, *Bauelemente der Optik - Taschenbuch der technischen Optik*, 6th ed. (Hanser, München, 1992).

[36] R. Wehner, "The world as the Insect sees it," in *Insect Communication*, T. Lewis, ed., chap. 2, 29–47 (R. Ent. Soc. Lond., London, 1984).

[37] P. McIntyre and S. Caveney, "Graded index optics are matched to optical geometry in the superposition eyes of scarab beetles," Phil. Trans. R. Soc. Lond. B **311**, 237–269 (1985).

[38] G. A. Horridge, "Optical mechanisms of clear–zone eyes," in *The Compound Eye and Vision of Insects*, G. A. Horridge, ed., 255–298 (Clarendon Press, Oxford, 1975).

[39] M. F. Land, F. Burton, and V. Meyer-Rochow, "The Optical Geometry of Euphausiid Eyes," J. Comp. Physiol. A **130**(1), 49–62 (1979).

[40] E. J. Warrant and P. D. McIntyre, "Limitations to resolution in superposition eyes," J. Comp. Physiol. A **167**, 785–803 (1990).

[41] R. Navarro and N. Franceschini, "On image quality of microlens arrays in diurnal superposition eyes," Pure Appl. Opt. **7**(6), 69–78 (1998).

[42] P. Carricaburu, "Examination of the classical optics of ideal apposition and superposition eyes," in *The Compound Eye and Vision of Insects*, G. A. Horridge, ed., 237–254 (Clarendon Press, Oxford, 1975).

[43] M. F. Land, "Structure of the retinae of the principal eyes of jumping spiders (salticidae: dendryphantinae) in relation to visual optics," J. exp. Biol. **51**, 443–470 (1969).

[44] D. S. Williams and P. McIntyre, "The principal eyes of a jumping spider have a telephoto component," Nature **288**, 578–580 (1980).

[45] P. Vukusic and J. R. Sambles, "Photonic structures in biology," Nature **424**, 852–855 (2003).

[46] M. F. Land, "Microlens arrays in the animal kingdom," Pure Appl. Opt. **6**, 599–602 (1997).

[47] D. Malacara and Z. Malacara, *Handbook of optical design*, 2nd ed. (Marcel Dekker, 2003).

[48] W. J. Smith, *Modern Optical Engineering: The Design of Optical Systems*, 2nd ed. (McGraw–Hill, New York, 1990).

[49] D. C. O'Shea, *Elements of modern optical design* (Wiley, 1985).

[50] M. Laikin, *Lens Design*, 2nd ed. (Marcel Dekker, 1995).

[51] G. Litfin, *Technische Optik in der Praxis* (Springer, 1995).

[52] K. Iizuka, *Engineering Optics*, 2nd ed. (Springer, 1987).

[53] D. Malacara, *Optical Shop Testing* (Wiley, New York, 1992).

[54] V. N. Mahajan, *Aberration theory made simple* (SPIE Optical Engineering Press, Bellingham, 1991).

[55] R. R. Shannon, *The Art and Science of Optical Design* (Cambridge University Press, 1997).

[56] J. Duparré, P. Schreiber, P. Dannberg, A. Bräuer, and M. Bitzer, "Miniaturisiertes Objektiv für digitale Kameras und Herstellung im Wafer-Maßstab," Pat. DE 10 2004 036 469.9 (2004).

[57] N. Schalm, "Entwicklung eines Messplatzes zur Bestimmung der Abbildungsqualität von miniaturisierten Kameraobjektiven," Master's thesis, Fachhochschule Jena / IOF Jena (2003).

[58] M. Oikawa, E. Okuda, K. Hamanaka, and H. Nemoto, "Integrated planar microlens and its applications," in *Proc. of Miniature Optics and Lasers*, L. E. Cramer, C. Roychoudhuri, and G. T. Forrest, eds., SPIE **898**, 3–11 (1988).

[59] K. Hamanaka, H. Nemoto, M. Oikawa, and E. Okuda, "Aberration properties of the planar microlens array and its applications to imaging optics," in *Proc. of Micro–Optics*, A. V. Scheggi, ed., SPIE **1014**, 58–65 (1988).

[60] A. Akiba and K. Iga, "Image multiplexer using a planar microlens array," Appl. Opt. **29**(28), 4092–4097 (1990).

[61] S. Kakizaki, J. Tanida, and Y. Ichioka, "Gray–image processing using optical array logic," Appl. Opt. **31**(8), 1093–1102 (1992).

[62] I. Glaser, "Lenslet array processors," Appl. Opt. **21**(7), 1271–1280 (1982).

[63] I. Glaser and L. Perelmutter, "Optical interconnections for digital processing: A noncoherent method," Opt. Soc. Am. **11**(1), 53–55 (1986).

[64] K. Matsushita, Y. Kajiki, E. Shimizu, and F. T. S. Yu, "Optical symbolic substitution using lenslet arrays," Opt. Eng. **32**(4), 847–851 (1993).

[65] I. Glaser, "Noncoherent parallel optical processor for discrete two– dimensional linear transformations," Opt. Lett. **5**(10), 449–451 (1980).

[66] C. v. Berkel, B. P. McGarvey, and J. A. Clarke, "Microlens arrays for 2D large area image sensors," Pure Appl. Opt. **3**, 177–182 (1994).

[67] J. A. Clarke, "Image sensor in which each lens element is associated with a plurality of pixels," Pat. US 6,057,538A (2000).

[68] I. Fujieda and H. Haga, "Contact type image sensor comprising a plurality of microlenses," Pat. US 5,877,492 (1999).

[69] G. B. Immega and G. H. Chapman, "Vision system and proximity detector," Pat. US 5,726,443 (1998).

[70] F. Mura, I. Shimoyama, and K. Hoshino, "A One–chip Scanning Retina with an Integrated Micromechanical Scanning Actuator," J. of Microelectromech. Syst. **10**(4), 492–497 (2001).

[71] F. Mura, I. Shimoyama, and K. Hoshino, "Design and performance of a micro–sized biomorphic compound eye with a scanning retina," J. Microelectromech. Syst. **9**(1), 32–37 (2000).

Bibliography

[72] R. F. Miracky, J. D. Reed, K. Hu, and C. Hilbert, "Integrated optical microelectromechanical systems and methods of fabricating and operating the same," Pat. US 6,636,653 (2003).

[73] K. Umeda and M. Sekine, "Simple Compound–Eye–Type Micro Vision Sensor and its Application for Detecting Motion," J. Robot. Mechatr. **14**(2), 193–198 (2002).

[74] D. Stipanicev, "Artificial compound eye (fuzzy eye) and its visual signal perception," in *Proc. of 2nd IMACS Int. Symp. on Mathematical and Intelligent Models in System Simulation*, **2**, 374–379 (1993).

[75] L. R. Lopez, "Optical compound eye sensor with ommatidium sensor and related methods," Pat. US 5,517,019 (1996).

[76] W. R. Clayton, R. G. Driggers, and K. M. Harmon, "Target location by a multiaperture vision system coupled to a back–propagation neural network," Opt. Eng. **32**(11), 2703–2708 (1993).

[77] M. S. Currin, P. Schonbaum, R. G. Driggers, and C. E. Halford, "Three gradient index lens tracker," Opt. Eng. **34**(2), 607–611 (1995).

[78] E. O. Cole, "Optical surveillance sensor apparatus," Pat. US 5,015,844 (1991).

[79] J. A. Cox, "Binary optical microlens detector array," Pat. US 5,401,968A (1995).

[80] M. Rothley, R. Mueller-Fiedler, E. Zabler, L. Erdmann, W. Leneke, M. Simon, K. Storck, and J. Schieferdecker, "Vorrichtung zur Erfassung elektromagnetischer Strahlung," Pat. DE 1992 360 6A1 (1999).

[81] M. Rothley, R. Mueller-Fiedler, E. Zabler, L. Erdmann, W. Leneke, M. Simon, K. Storck, and J. Schieferdecker, "Apparatus for sensing electromagnetic radiation," Pat. US 6,710,348B1 (2004).

[82] M. D. Rostoker, "Sensing device for capturing a light image," Pat. US 5,648,655 (1997).

[83] M. D. Rostoker, "Electronic camera with binary lens element array," Pat. US 5,760,834 (1998).

[84] M. D. Rostoker and D. E. Sanders, "Image-sensing display panels with LCD display panel and photosensitive element array," Pat. US 5,340,978 (1994).

[85] M. D. Rostoker and D. E. Sanders, "Image–sensing display panels with lcd display panel and photosensor array," Pat. US 5,432,333A (1995).

[86] M. M. Meyers, "Diffractive / Refractive lenslet array," Pat. US 5,696,371A (1997).

[87] M. M. Meyers, "A diffractive/refractive lenslet array," Pat. EP 0,809,124A2/A3 (1997).

[88] M. M. Meyers, "Diffractive / refractive lenslet array incorporating a second aspheric surface," Pat. US 5,571,492A (1998).

[89] G. Gal, "Dispersive microlens," Pat. US 5,497,269A (1996).

[90] K. Yamada, J. Tanida, W. Yu, S. Miyatake, K. Ishida, D. Miyazaki, and Y. Ichioka, "Fabrication off diffractive microlens array for opto–electronic hybrid information system," in *Proc. of Diffractive Optics' 99*, 52–53 (EOS, 1999).

[91] J. Tanida, T. Kumagai, K. Yamada, and S. Miyatake, "Thin observation module by bound optics (TOMBO) concept and experimental verification," Appl. Opt. **40**(11), 1806–1813 (2001).

[92] Y. Kitamura, R. Shogenji, K. Yamada, S. Miyatake, M. Miyamoto, T. Morimoto, Y. Masaki, N. Kondou, D. Miyazaki, J. Tanida, and Y. Ichioka, "Compact image capturing system based on compound imaging and digital reconstruction," in *Proc. of Micro– and Nano–optics for optical interconnection and information processing*, M. R. Taghizadeh, H. Thienpont, and G. E. Jabbour, eds., SPIE **4455**, 34–41 (2001).

[93] Y. Kitamura, R. Shogenji, K. Yamada, S. Miyatake, M. Miyamoto, T. Morimoto, Y. Masaki, N. Kondou, D. Miyazaki, J. Tanida, and Y. Ichioka, "Reconstruction of a high–resolution image on a compound–eye image–capturing system," Appl. Opt. **43**(8), 1719–1727 (2004).

[94] Y. Kitamura, R. Shogenji, K. Yamada, S. Miyatake, M. Miyamoto, and J. Tanida, "Color imaging with an integrated compound imaging system," Opt. Exp. **11**(18), 2109–2117 (2003).

Bibliography

[95] G. Lippmann, "La photographie integrale," Comptes-Rendus Academie des Sciences **146**, 446–451 (1908).

[96] H. E. Ives, "Optical properties of a Lippmann lenticulated sheet," J. Opt. Soc. Am. **21**, 171–176 (1931).

[97] C. B. Burckhardt, "Optimum parameters and resolution limitation of integral photography," J. Opt. Soc. Am. **58**(1), 71–76 (1968).

[98] N. Davies and M. McCormick, "The use of microlens arrays in integral photography," in *Digest of Short Meet. on Microlens Arrays at NPL, Teddington*, M. C. Hutley, ed., IOP **30**, 109–122 (1991).

[99] N. Davies, M. McCormick, and M. Brewin, "Design and analysis of an image transfer system using microlens arrays," Opt. Eng. **33**(11), 3624–3633 (1994).

[100] B. Lee, S. Jung, S. W. Min, and J. H. Park, "Study for wide–viewing integral photography using an aspheric Fresnel–lens array," Opt. Eng. **41**(10), 2572–2576 (2002).

[101] L. Erdmann and K. J. Gabriel, "High–resolution digital integral photography by use of a scanning microlens array," Appl. Opt. **40**(31), 5592–5599 (2001).

[102] B. Lee, S. Jung, S. W. Min, and J. H. Park, "Three–dimensional display by use of integral photography with dynamically variable images planes," Opt. Lett. **26**(19), 1481–1482 (2001).

[103] J. H. Park, S. W. Min, S. Jung, and B. Lee, "Analysis of viewing parameters for two display methods based on integral photography," Appl. Opt. **40**(29), 5217–5232 (2001).

[104] J. S. Jang, Y. S. Oh, and B. Javidi, "Spatiotemporally multiplexed integral imaging projector for large–scale high–resolution three–dimensional display," Opt. Exp. **12**(4), 557–563 (2004).

[105] S. Kurahashi, K. Iijima, K. Yano, H. Morishima, K. Mori, and T. Sakimura, "Compound eye camera system," Pat. US 6,278,480B1 (2001).

[106] K. Mori, K. Iijima, K. Yano, S. Kurahasi, and T. Sakimura, "Multi–lens image pickup apparatus," Pat. US 6,507,358B1 (2003).

[107] A. K. Weiss, "Light sensing device with lenticular pixels," Pat. US 4,694,185 (1987).

[108] Y. Iizuka and A. Komatsu, "Solid state image sensor device with microlenses," Pat. US 5,250,798 (1993).

[109] W. B. Veldkamp, "Optically coupled focal plane arrays using lenslets and multiplexers," Pat. US 4,994,664 (1991).

[110] H. Miyano, "Solid–state image pickup device having microlenses each with displaced optical axis," Pat. US 5,610,390A (1997).

[111] T. Hidekazu and K. Tetsunobu, "Solid-state image pickup device and solid-state image pickup system provided with the same," Pat. JP 2001210812A (2001).

[112] H. Takahashi and T. Kochi, "Image pickup apparatus," Pat. Application US 2001/0026322A1 (2001).

[113] K. Akito, T. Mitsugi, N. Yoshiaki, K. Norihisa, T. katsumi, and K. Hirotatsu, "Solid image pickup device," Pat. JP 06118209A, April (1994).

[114] M. Toshiji, "Solid-state image pickup element having micro lens," Pat. JP 06133229A (1994).

[115] J. S. Sanders, "Ultra–wide field of view imaging optical system designs based on arthropod vision systems," in *Proc. of Acquisition, Tracking and Pointing XI*, M. K. Masten and L. A. Stockum, eds., SPIE **3086**, 359–366 (1997).

[116] A. B. Meinel, "Aperture synthesis using independent telescopes," Appl. Opt. **9**(11), 2501–2504 (1970).

[117] R. V. Shack, J. D. Rancourt, and H. Morrow, "Effects of dilution on a six–element sythetic aperture," Appl. Opt. **10**(2), 257–259 (1971).

[118] C. Hogge, J. Schultz, D. Mason, and W. Thompson, "Physical optics of multiaperture systems," Appl. Opt. **27**(24), 5127–5134 (1988).

Bibliography

[119] A. B. Meinel, M. P. Meinel, and N. J. Woolf, "Multiple aperture telescope diffraction images," in *Applied Optics and Optical Engineering*, R. R. Shannon and J. C. Wyant, eds., **9**, chap. 5 (Academic Press, San Diego, 1983).

[120] K. Vogt, "Ray path and reflection mechanisms in crayfish eyes," Z. Naturforsch. 451–453 (1977).

[121] K. Vogt, "Die Spiegeloptik des Flusskrebsauges," J. Comp. Physiol. A **135**(1), 1–19 (1980).

[122] M. F. Land, "Superposition images are formed by reflection in the eyes of some oceanic decapod crustacea," Nature **263**, 764–765 (1976).

[123] K. P. Bryceson and P. McIntyre, "Image Quality and Acceptance Angle in a Reflecting Superposition Eye," J. Comp. Phys. A **151**, 367–380 (1983).

[124] D.-E. Nilsson, "A new type of imaging optics in compound eyes," Nature **332**(6159), 76–78 (1988).

[125] J. R. P. Angel, "Lobster eyes as x-ray telescopes," Astrophys. J. **233**(1), 364–373 (1979).

[126] D. Gabor, "Improvements in or relating to optical systems composed of lenticules," Pat. UK 541,753 (1940).

[127] M. C. Hutley, "Integral photography, superlenses and the moiré magnifier," in *Digest of Top. Meet. on Microlens Arrays at NPL, Teddington*, M. C. Hutley, ed., EOS **2**, 72–75 (1993).

[128] C. Hembd-Sölner, R. F. Stevens, and M. C. Hutley, "Imaging properties of the Gabor superlens," J. Opt. A: Pure Appl. Opt. **1**, 94–102 (1999).

[129] R. F. Stevens and N. Davies, "Lens Arrays and Photography," J. Photograph. Sci. **39**, 199–208 (1991).

[130] R. F. Stevens and T. G. Harvey, "Lens arrays for a three–dimensional imaging system," J. Opt. A: Pure Appl. Opt **4**, 17–21 (2002).

[131] H. Nemoto, T. Kishimoto, and K. Hamanaka, "Method for manufatcuring an erect image, unity magnification, resin lens array," Pat. US 6,625,864B2 (2003).

[132] A. Wirth, A. J. Jankevics, F. M. Landers, T. L. Bruno, D. P. D'Amato, and L. E. Schmutz, "Optical instrument with micro–lenses," Pat. US 5,270,859A (1993).

[133] A. Wirth, A. J. Jankevics, F. M. Landers, T. L. Bruno, D. P. D'Amato, L. E. Schmutz, L. H. Gilligan, and J. L. Duncan, "Micro–lens panoramic imager," Pat. US 5,291,334A (1994).

[134] M. Hutley, R. F. Stevens, and C. Hembd, "Imaging Properties of the "Gabor Superlens"," in *Digest of Top. Meet. on Microlens Arrays at NPL, Teddington*, M. C. Hutley, ed., EOS **13**, 101–104 (1997).

[135] M. Hutley and R. F. Stevens, "The Formation of Integral Images by Afocal Pairs of Lens Arrays ("Superlenses")," in *Digest of Short Meet. on Microlens Arrays at NPL, Teddington*, M. C. Hutley, ed., IOP **30**, 147–154 (1991).

[136] M. Kawazu and Y. Ogura, "Application of gradient-index fiber arrays to copying machines," Appl. Opt. **19**(7), 1105–1112 (1980).

[137] J. D. Rees, "Non-Gaussian imaging properties of GRIN fiber lens arrays," Appl. Opt. **21**(6), 1009–1012 (1982).

[138] J. D. Rees and W. Lama, "Some radiometric properties of gradient–index fiber lenses," Appl. Opt. **19**(7), 1065–1069 (1980).

[139] M. Toyama and M. Takami, "Luminous intensity of gradient-index lens array," Appl. Opt. **21**(6), 1013–1016 (1982).

[140] N. F. Borrelli, R. H. Bellman, J. A. Durbin, and W. Lama, "Imaging and radiometric properties of microlens arrays," Appl. Opt. **30**(25), 3633–3642 (1991).

[141] J. D. Rees, D. B. Kay, and W. L. Lama, "Gradient index lens array having reduction properties," Pat. US 4,331,380 (1982).

Bibliography

[142] J. D. Rees and W. Lama, "Reduction/enlargement gradient–index lens array," Appl. Opt. **23**(11), 1715–1724 (1984).

[143] K. Araki, "Optical projection system," Pat. US 4,750,022 (1988).

[144] K. Araki, "Compound eye systems for nonunity magnification projection," Appl. Opt. **29**(28), 4098–4104 (1990).

[145] W. B. Hugle, R. Daendliker, and H. P. Herzig, "Lens array photolithography," Pat. US 8,114,732 (1993).

[146] R. Völkel, W. Singer, H. P. Herzig, and R. Dändliker, "Imaging properties of microlens array systems," in *Proc. of MOC'95 in Hiroshima* (1995).

[147] R. Völkel, H. P. Herzig, P. Nussbaum, and R. Dändliker, "Microlens array imaging system for photolithography," Opt. Eng. **35**(11), 3323–3330 (1996).

[148] P. Nussbaum, R. Völkel, H. P. Herzig, M. Eisner, and S. Haselbeck, "Design, fabrication and testing of microlens arrays for sensors and Microsystems," Pure Appl. Opt. **6**, 617–636 (1997).

[149] R. Völkel, C. Ossmann, T. Scharf, H. P. Herzig, and R. Dändliker, "Optical microsystems for imaging," in *Proc. of Electronic Image Capture and Publishing*, T. M. Bernard, ed., EOS/SPIE **3410**, 54–63 (1998).

[150] H. Horiguchi, "Directly detectable image sensor employing a lens array and method of producing the same," Pat. US 4,733,096 (1988).

[151] V. Shaoulov and J. P. Rolland, "Design and assessment of microlenslet–array relay optics," Appl. Opt. **42**(34), 6838–6845 (2003).

[152] N. J. Krasutsky, "Focal array reimaging system," Pat. US 4,970,403 (1990).

[153] H. Tokumaru, "Optical projection system," Pat. US 4,474,459 (1984).

[154] N. Mochizuki, S. Minami, and Y. Matsui, "Compound eye projection device," Pat. US 4,512,641 (1985).

[155] N. Mochizuki and S. Minami, "Compound eye optical system having a variable magnification function," Pat. US 4,630,902 (1986).

[156] R. H. Anderson, "Optical apparatus including a pair of mosaics of optical imaging elements," Pat. US 28,162 (1974).

[157] R. H. Anderson, "Close-up imaging of documents and displays with lens arrays," Appl. Opt. **18**(4), 477–484 (1979).

[158] R. J. Burger, "Lenslet array systems and methods," Pat. US 5,973,844A (1999).

[159] R. J. Burger, "Lenslet array systems and methods," Pat. US 6,124,974A (2000).

[160] K. Hamanaka, H. Nemoto, M. Oikawa, E. okuda, and T. Kishimoto, "Multiple imaging and multiple Fourier transformation using planar microlens arrays," Appl. Opt. **29**(28), 4064 (1990).

[161] K. Iga, M. Oikawa, S. Misawa, J. Banno, and Y. Kokubun, "Stacked planar optics: An application of the planar microlens," Appl. Opt. **21**(19), 3456–3460 (1982).

[162] K. H. Brenner and W. Singer, "Stacked Micro–optical Systems," in *Micro–Optics: Elements, systems and applications*, H. P. Herzig, ed., chap. 8, 199–221 (Taylor & Francis, 1997).

[163] M. M. Meyers, "Compact digital camera with segmented fields of view," Pat. EP 0,840,502A2 (1998).

[164] M. M. Meyers, "Compact digital camera with segmented fields of view," Pat. US 6,137,535A (2000).

[165] M. M. Meyers, "Lenslet array system incorparting an integral field lens/reimager lenslet array," Pat. US 5,731,899A (1998).

[166] M. M. Meyers, "Lenslet array system incorporating a field lenslet array," Pat. US 5,812,322 (1998).

[167] R. Völkel and S. Wallstab, "Flachbauendes Bilderfassungssystem," Pat. DE 199 17 890A1 (1999).

[168] K. D. Möller, *Optics* (University Science Books, Mill Valley, 1988).

Bibliography

[169] S. Sinzinger and J. Jahns, *Microoptics* (Wiley–VCH, Weinheim, 1999).

[170] M. Born and E. Wolf, *Principles of optics*, 7th ed. (Cambridge University Press, 1999).

[171] N. Hodgson and H.Weber, *Optische Resonatoren* (Springer, 1992).

[172] A. E. Siegmann, *Lasers* (University Science Books, Mill Valey, 1986).

[173] W. Shaomin and L. Ronchi, "Principles and design of optical arrays," in *Progress in Optics*, E. Wolf, ed., 25, 279–347 (North-Holland, Amsterdam, 1988).

[174] F. L. Pedrotti and S. J. Pedrotti, *Introduction to optics*, 2nd ed. (Prentice–Hall, 1993).

[175] S. A. Collins, "Lens-system diffraction integral written in terms of matrix optics," JOSA A **60**(9), 1168–1177 (1970).

[176] H. K. A. El-Hady, "Design properties of optical arrays," Ph.D. thesis, University complutense of Madrid, Faculty of physics, Optics department (1998).

[177] N. Lindlein, "Simulation of micro-optical systems including microlens arrays," J. Opt. A: Pure Appl. Opt. **4**, 1–9 (2002).

[178] C. Hofmann, *Die Optische Abbildung*, 1st ed. (Geest & Portig, Leipzig, 1980).

[179] A. Gullstrand, "Beitrag zur Theorie des Astigmatismus," Skand. Arch. Physiol. **2**, 269–359 (1889).

[180] H. P. Herzig, *Micro–Optics: Elements, systems and applications* (Taylor & Francis, 1997).

[181] D. Daly, *Microlens Arrays* (Taylor & Francis, London, 2001).

[182] N. F. Borrelli, *Microoptics Technology: Fabrication and Applications of lens and arrays and devices* (Marcel Dekker, New York, 1999).

[183] K. Iga, Y. Kokubun, and M. Oikawa, *Fundamentals of Microoptics* (Academic Press, New York, 1984).

[184] T. Hessler, M. Rossi, J. Pedersen, M. T. Gale, M. Wegner, and H. J. Tiziani, "Microlens arrays with spatial variation of the optical functions," in *Digest of Top. Meet. on Microlens Arrays at NPL, Teddington*, M. C. Hutley, ed., EOS **13**, 42–47 (1997).

[185] T. L. Hoopman, "Method of making an array of variable focal length microlenses," Pat. US 5,439,621A (1995).

[186] S. Sinzinger and J. Jahns, "Integrated micro–optical imaging system with a high interconnection capacity fabricated in planar optics," Appl. Opt. **36**(20), 4729–4735 (1997).

[187] Z. D. Popovich, R. A. Sprague, and G. A. N. Conell, "Technique for monolithic fabrication of microlens arrays," Appl. Opt. **27**(7), 1281–1284 (1988).

[188] D. Daly, R. F. Stevens, M. C. Hutley, and N. Davies, "The manufacture of microlenses by melting photoresist," J. Meas. Sci. Technol. **1**, 759–766 (1990).

[189] K. Mersereau, C. R. Nijander, W. P. Townsend, R. J. Crisci, A. Y. Feldblum, and D. Daly, "Design, fabrication and testing of refractive microlens arrays," in *Digest of Top. Meet. on Microlens Arrays at NPL, Teddington*, M. C. Hutley, ed., EOS **2**, 60–64 (1993).

[190] L. Erdmann and D. Efferenn, "Technique for monolithic fabrication of silicon microlenses with selectable rim angles," Opt. Eng. **36**, 1094–1098 (1997).

[191] A. Schilling, R. Merz, C. Ossmann, and H. P. Herzig, "Surface profiles of reflow microlenses under the influence of surface tension and gravity," Opt. Eng. **39**(8), 2171–2176 (2000).

[192] S. Haselbeck, H. Schreiber, J. Schwider, and N. Streibl, "Microlenses fabricated by melting a photoresist on a base layer," Opt. Eng. **32**(6), 1322–1324 (1993).

[193] N. Lindlein, S. Haselbeck, and J. Schwider, "Simplified Theory for Ellipsoidal Melted Microlenses," in *Digest of Top. Meet. on Microlens Arrays at NPL, Teddington*, M. C. Hutley, ed., EOS **5**, 7–10 (1995).

[194] M. Eisner, N. Lindlein, and J. Schwider, "Making diffraction limited refractive microlenses of spherical and elliptical form," in *Digest of Top. Meet. on Microlens Arrays at NPL, Teddington*, M. C. Hutley, ed., EOS **13**, 39–41 (1997).

[195] C. D. Carey, D. P. Godwin, P. C. H. Poon, D. J. Daly, D. R. Selviah, and J. E. Midwinter, "Astigmatism in ellipsoidal and spherical photoresist microlenses used at oblique incidence," in *Digest of Top. Meet. on Microlens Arrays at NPL, Teddington*, M. C. Hutley, ed., EOS **2**, 65–68 (1993).

[196] Z. D. Popovic, R. A. Sprague, and G. A. N. Connell, "Pedestral–type microlens fabrication process," Pat. US 4,689,291 (1987).

[197] M. C. Hutley, D. Daly, and R. F. Stevens, "The testing of microlens arrays," in *Digest of Short Meet. on Microlens Arrays at NPL, Teddington*, M. C. Hutley, ed., IOP **30**, 67–82 (1991).

[198] D. Daly and M. C. Hutley, "Microlens measurement at NPL," in *Digest of Top. Meet. on Microlens Arrays at NPL, Teddington*, M. C. Hutley, ed., EOS **2**, 50–54 (1993).

[199] J. Duparré, P. Schreiber, P. Dannberg, T. Scharf, P. Pelli, R. Völkel, H.-P. Herzig, and A. Bräuer, "Artifical compound eyes–different concepts and their application to ultra flat image acquisition sensors," in *Proc. of MOEMS and Miniaturized Systems IV*, A. El-Fatatry, ed., SPIE **5346**, 89–100 (2004).

[200] J. Duparré, P. Dannberg, P. Schreiber, A. Bräuer, and R. Völkel, "Bilderfassungssystem und dessen Verwendung," Pat. DE 10 2004 003 013.8 (2004).

[201] J. Duparré, P. Dannberg, P. Schreiber, A. Bräuer, and R. Völkel, "Bilderfassungssystem und dessen Verwendung," PCT Pat. Appl. 03F44093-IOF (2005).

[202] J. Duparré, P. Dannberg, P. Schreiber, A. Bräuer, and A. Tünnermann, "Artificial apposition compound eye fabricated by micro–optics technology," Appl. Opt. **43**(22), 4303–4310 (2004).

[203] J. Duparré, P. Dannberg, P. Schreiber, and A. Bräuer, "Micro–optically fabricated artificial apposition compound eye," in *Proc. of Sensors and Camera Systems for Scientific, Industrial, and Digital Photography Applications V*, M. M. Blouke, N. Sampat, and R. J. Motta, eds., IS&T/SPIE **5301**, 25–33 (2004).

[204] P.-F. Rüedi, P. Heim, F. Kaess, E. Grenet, F. Heitger, P.-Y. Burgi, S. Gyger, and P. Nussbaum, "A 128 x 128 Pixel 120–dB Dynamic–Range Vision–Sensor Chip for Image Contrast and Orientation Extraction," IEEE J. Solid–State Circ. **38**(12), 2325–2333 (2003).

[205] J. Duparré, P. Dannberg, P. Schreiber, A. Bräuer, P. Nussbaum, F. Heitger, and A. Tünnermann, "Ultra–Thin Camera Based on Artificial Apposition Compound Eyes," in *Proc. of 10th Microopt. Conf.*, W. Karthe, G. D. Khoe, and Y. Kokubun, eds., ISBN: 3-8274-1603-5, E–2 (Elsevier, 2004).

[206] J. Duparré, P. Dannberg, O. Mauroner, and A. Bräuer, "Mit den Augen einer Fliege," Design & Electronic **9**, 40–43 (2004).

[207] J. Duparré, P. Dannberg, P. Schreiber, A. Bräuer, and A. Tünnermann, "Thin compound eye camera," accepted for publ. in Appl. Opt. **44**(15), xx–xx (2005).

[208] R. F. Stevens, "Optical inspection of periodic structures using lens arrays and moiré magnification," Imaging Sci. J. **47**, 173–179 (1999).

[209] H. Kamal, R. Völkel, and J. Alda, "Properties of moiré magnifiers," Opt. Eng. **37**(11), 3007–3014 (1998).

[210] P. Dannberg, G. Mann, L. Wagner, and A. Bräuer, "Polymer UV-molding for micro-optical systems and O/E- integration," in *Proc. of Micromachining for Micro–Optics*, S. H. Lee and E. G. Johnson, eds., SPIE **4179**, 137–145 (2000).

[211] P. F. Rüedi, P. Heim, F. Kaess, E. Grenet, F. Heitger, P. Y. Burgi, S. Gyger, and P. Nussbaum, "A 128 x 128 Pixel 120dB Dynamic Range Vision Sensor Chip for Image Contrast and Orientation Extraction," in *Proc. of IEEE Int. Solid-State Circ. Conf.*, Paper 12.8 (2003).

[212] R. Rumpf and E. Johnson, "Micro–photonic systems utilizing SU–8," in *Proc. of MOEMS and Miniaturized Systems IV*, El-Fatatry, ed., SPIE **5346**, 64–72 (2004).

[213] M. Shaw, D. Nawrocki, R. Hurditch, and D. Johnson, "Improving the process capability of SU-8," Microsyst. Techn. **10**, 1–6 (2003).

[214] B. Kress and P. Meyrueis, *Digital Diffractive Optics* (Wiley, 2000).

[215] J. Duparré, P. Schreiber, and R. Völkel, "Theoretical analysis of an artificial superposition compound eye for application in ultra flat digital image acquisition devices," in *Proc. of Optical Design and Engineering*, L. Mazurany, P. J. Rogers, and R. Wartmann, eds., SPIE **5249**, 408–418 (2003).

[216] J. Duparré, P. Schreiber, A. Matthes, E. Pshenay-Severin, A. Bräuer, A. Tünnermann, R. Völkel, M. Eisner, and T. Scharf, "Microoptical telescope compound eye," Opt. Exp. **13**(3), 889–903 (2005).

[217] J. Duparré and R. Göring, "Numerical wave optical analysis of microlens array telescopes and comparison with experimental results," Appl. Opt. **42**(19), 3992–4001 (2003).

[218] J. Duparré, B. Götz, and R. Göring, "Micro–optical 1x4 fiber switch for multimode fibers with 600–μm core diameters," Appl. Opt. **42**(34), 6889–6896 (2003).

[219] J. Duparré, D. Radtke, and P. Dannberg, "Implementation of field lens arrays in beam–deflecting microlens array telescopes," Appl. Opt. **43**(25), 4854–4861 (2004).

[220] M. Eisner, S. Haselbeck, H. Schreiber, and J. Schwider, "Reactive ion etching of microlens arrays into fused silicia," in *Digest of Top. Meet. on Microlens Arrays at NPL, Teddington*, M. C. Hutley, ed., EOS **2**, 17–19 (1993).

[221] M. Eisner and J. Schwider, "Transferring resist microlenses into silicon by reactive ion etching," Opt. Eng. **35**(10), 2979–2982 (1996).

[222] L. C. Wittig and E. B. Kley, "Approximation of refractive micro optical profiles by minimal surfaces," in *Proc. of Micromachine Technology for Diffractive and Holographic Optics*, S. H. Lee and J. A. Cox, eds., SPIE **3879**, 32–38 (1999).

[223] E. D. Palik, *Handbook of optical constants (A)*, 1 (Academic Press, Orlando, 1985).

[224] M. Pitchumani, W. Mohammed, H. Hockel, and E. G. Johnson, "Presculpting of photoresist using additive lithography," in *Proc. of Micromachining Technology for Micro-Optics and Nano-Optics II*, E. G. Johnson and G. P. Nordin, eds., SPIE **5347**, 85–94 (2004).

[225] B. Berge and J. Peseux, "Variable focal lens controlled by an external voltage: an application of electrowetting," Eur. Phys. J. E **3**, 159–163 (2000).

[226] C. Gabay, B. Berge, G. Dovillaire, and S. Bucourt, "Dynamic study of a Varioptic variable focal lens," in *Proc. of Current Developments an Lens Design and Optical Engineering III*, R. E. Fischer, W. J. Smith, and R. B. Johnson, eds., SPIE **4767**, 159–165 (2002).

[227] L. Saurei, J. Peseux, F. Laune, and B. Berge, "Tunable liquid lens based on electrowetting technology: principle, properties and applications," in *Proc. of 10th Microopt. Conf.*, W. Karthe, G. D. Khoe, and Y. Kokubun, eds., ISBN: 3-8274-1603-5, E–1 (Elsevier, 2004).

Appendix

A Anamorphic Microlenses by Reflow on an Ellipsoidal Base

For the aberration correction purposes under oblique incidence a torus segment is needed as anamorphic optical surface. In the following is shown that a microlens, fabricated by reflow on an ellipsoidal base is a sufficiently good approximation of this required surface. Therefore, it is first demonstrated that an ellipsoid is a good approximation of the torus segment in the required parameters space. Furthermore it is shown that the reflow on an ellipsoidal base actually results in an ellipsoidal lens shape and that the radii of curvature of the lens can be separately tuned just by the size of the lens-base axes.

An ellipsoidal microlens is usually described in an cartesian coordinate system with the lateral coordinates x, y and z as the height by

$$z = z_0 + c_z \sqrt{1 - \frac{x^2}{c_x^2} - \frac{y^2}{c_y^2}}. \tag{A.1}$$

Here, c_x, c_y and c_z are the half-axes of the ellipsoid and z_0 is defined that $z = 0$ is valid at the resist-substrate boundary. The ellipsoidal lens-base is described by

$$\frac{x^2}{a_x^2} + \frac{y^2}{a_y^2} = 1, \tag{A.2}$$

where a_x and a_y are the half-axes of the ellipsoidal lens rim, coupled to the parameters of the ellipsoid by

$$a_{x,y} = c_{x,y} \sqrt{1 - \frac{z_0^2}{c_z^2}}. \tag{A.3}$$

Equivalently an ellipsoidal microlens can also be described as an anamorphic aspherical surface

$$z = h_L - \frac{\frac{x^2}{R_x^2} + \frac{y^2}{R_y^2}}{1 + \sqrt{1 - (1 + k_x)\frac{x^2}{R_x^2} - (1 + k_y)\frac{y^2}{R_y^2}}}. \tag{A.4}$$

Here, $R_{x,y}$ are the paraxial radii of curvature along the two main axes of the lens and $k_{x,y}$ are the conical constants. The transformation of the describing parameters is done via

$$R_{x,y} = \frac{c_{x,y}^2}{c_z} \quad \text{and} \quad k_{x,y} = -\frac{c_z^2 - c_{x,y}^2}{c_z^2} \quad \text{and} \quad h_L = z_0 + c_z. \tag{A.5}$$

In case of $k_x = k_y = 0$, Eq. (A.4) describes a torus segment, which is exactly the desired anamorphic lens shape.

In Fig. A.1 the surface deviation of an ellipsoidal lens from a torus segment having the same paraxial radii of curvature is plotted. The peak to valley (PV) deviation for the given values of radii of curvature, which are typical for the considered microlenses, are less than $\lambda/14$ (at $\lambda = 550$nm) and thus neglectable. Therefore ellipsoidal microlenses are an appropriate approach to model the desired anamorphic microlenses.
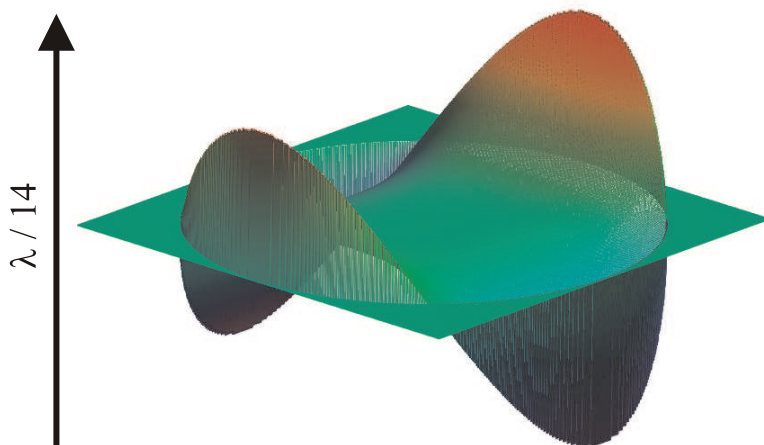

Figure A.1. Surface deviation between a torus segment and an ellipsoidal microlens with identical paraxial radii of curvature $R_x = 485.7\mu$m and $R_y = 609.6\mu$m. $h_L = 20.2\mu$m. Half-axes are $a_x = 138.6\mu$m and $a_y = 155.6\mu$m. Conical constants for representation of the ellipsoidal lens $k_x = -0.096$ and $k_y = 0.134$. For the representation of the torus segment $k_x = k_y = 0$ is set.

A surface, generated by numerical iterative surface minimization with the constraints of volume conservation and the conservation of the resist boundary [222] but free resulting surface profile, for the same starting parameters of the resist cylinder, was compared to the results of a numerical parametric model [193], where additionally an ellipsoidal shape is assumed for the resulting lens. Figure A.2 (c) shows the height difference between the expected ideal ellipsoidal microlens and the computer iterated surface. A good correspondence can be observed. The deviation along the rim of the microlens is the result of coarse sampling during simulation.

Consequently, the melting process on an ellipsoidal resist base can be modeled numerically parametric with sufficient accuracy. The model allows to determine the parameters of the ellipsoidal lens, such as the lens height and the major radii of curvatures as a function of the half-axes of the ellipsoidal base and the resist height and vice versa.

For constant resist cylinder height, the generation of the ellipsoidal microlenses by exposure through photo lithographic masks and subsequent reflow was experimentally explored [199]. The connection of the tangential and the sagittal radii of curvature and the lens height with the geometry of the ellipsoidal base was evaluated. From simple geometrical considerations on a circle follows Eq. (3.7). If h_L is constant with a sufficient accuracy, independently of the size of the microlens-base, the relationship between the major radii of curvature of the ellipsoidal microlens $R_t = R_x$ and $R_s = R_y$ and the major and the minor half-axes of the ellipsoidal lens-base $a_t = a_x$ and $a_s = a_y$ becomes especially simple and is represented by Eq. (3.8) [193].
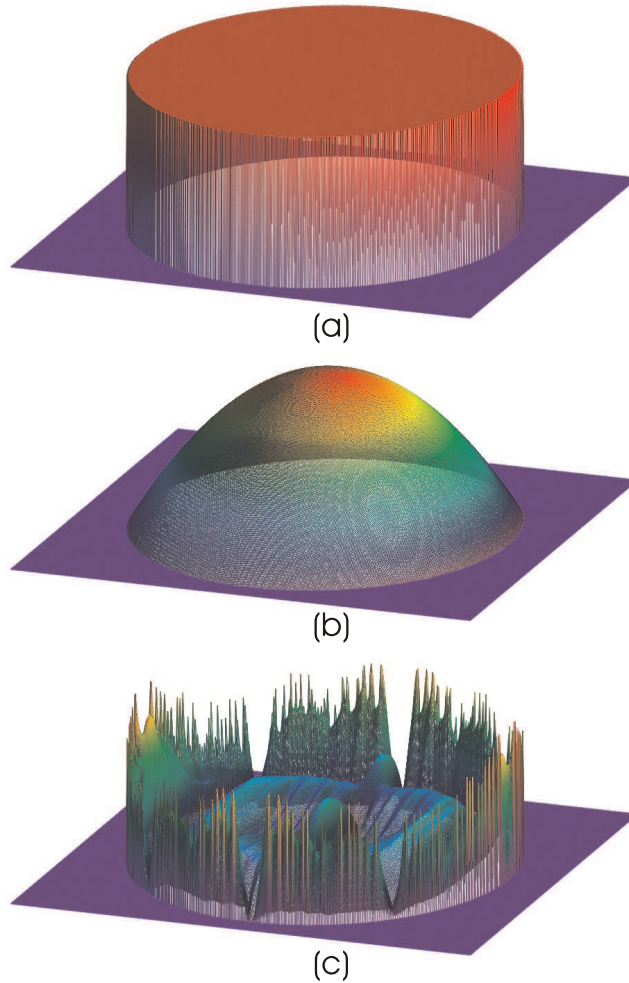
Figure A.2. Comparison of result of iterative melting simulation and numerical parametric model of ellipsoidal microlens formation. (a) Resist cylinder on an ellipsoidal base to be melted, height: 10.18μm, microlens-bases: $a_x = 138.9\mu$m, $a_y = 155.6\mu$m. (b) Computer simulated surface by iterative melting of the ellipsoidal resist cylinder, $h_L = 20.3\mu$m (field of 350x350 pixel with 1x1μm^2 size). (c) Surface deviation (PV) of numerically parametric determined ideal ellipsoidal microlens ($c_x = 512.26\mu$m, $c_y = 574.91\mu$m, $c_z = 539.23\mu$m and $h_L = 20.23\mu$m) and iterated surface is maximum $\lambda/7$ (at $\lambda = 550$nm) if the rim is cut (10% of diameter) and thus within the diffraction limit.

Herein h_L is assumed to be small with respect to a_t and a_s.

The assumption of an approximately constant microlens height was verified by measuring the height of circular microlenses with varying lens-base diameters (Fig. A.3).

At the first glance, the measured heights differ quite remarkable from the model calculation. In the numerical parametric model [193] the volume is supposed to be conserved, but in reality a volume loss occurs. There are at least two reasons which cause volume loss. One is material evaporation during melting and another is removing of unexposed resist during development. For spherical microlenses ($D = 250\mu$m) this loss was about 17% for the applied microlens fabrication technique. Because of this effect, one has to make a correction when approximating
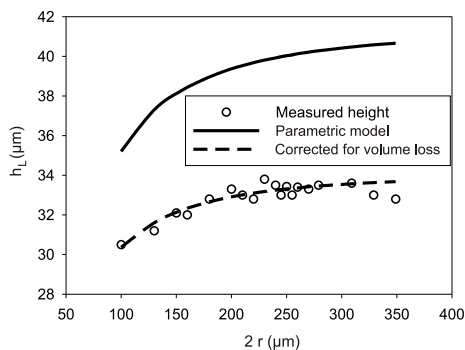
Figure A.3. Measured height of circular microlenses after reflow. Resist cylinder height is constant. Lens diameters range from 100μm to 349μm. After correction for volume loss, the numerical parametric model of the reflow process [193] fits well to the measured values. The microlens height is approximately constant.

absolut lens parameters by the numerical parametric model. However, the relative change is represented with sufficient accuracy, even without correction for volume loss. In Fig. A.3 the result of the model calculation with the corrected volume is plotted as dashed line. Good agreement for microlens diameters smaller than 300μm at 33μm lens height is achieved.

The validity of Eq. (3.8) was demonstrated explicitly for different parameter sets by measuring the radii of curvatures R_x and R_y of ellipsoidal microlenses as functions of the lens-base half-axes a_x and a_y. Figure A.4 shows measurements on microlenses fabricated with the same resist cylinder height as the microlenses of Fig. A.3 but with different amounts of ellipticity. The correspondence between Eq. (3.8) and the measured values is shown in Fig. A.4 (a). The
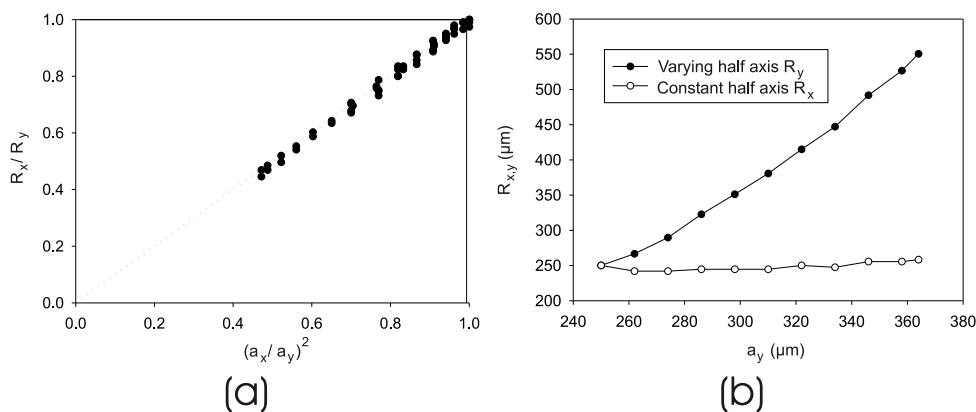

(a) (b)

Figure A.4. Radii of curvature of ellipsoidal microlens as a function of the lens-base dimensions. (a) The ratio of radii of curvature R_x/R_y as a function of the ratio of half-axes $(a_x/a_y)^2$. Black points are measured values for resist and quartz microlenses. Dotted line is after Eq. (3.8). (b) Measured radii of curvature in both axes directions. The radius of curvature of the long axis is tuned by the lens-base. The size of the short axis is held constant and so is the radius of curvature in this direction.

half-axes a_x and a_y are varying from 250μm to 350μm. The largest deviation of the measured

values from Eq. (3.8) is 3.8%. If one half-axis of a lens-base is varied and the other is fixed the lens height stays constant. Therefore the radius of curvature for the fixed axis is constant within the measurement errors, while the other axis can be tuned by changing the size of the lens-base (Fig. A.4 (b)).

For implementation into an artificial compound eye microoptical sensor (Chapter 5) MLAs with ellipsoidal microlenses of different ellipticity were fabricated by reflow and subsequently transferred into fused silica. In Fig. A.5 and Fig. A.6 the measured radii of curvatures (using a Rank Taylor Hobson profiling instrument FormTalysurf PGI+) of the large and the small axes of the ellipsoidal microlens, respectively, are compared to the required values. They are determined by Eq. (3.8) and the parameters of the circular microlens as the starting value. Each experimental data point for one ratio $a_{x,y}/r$ represents a different microlens. The radius
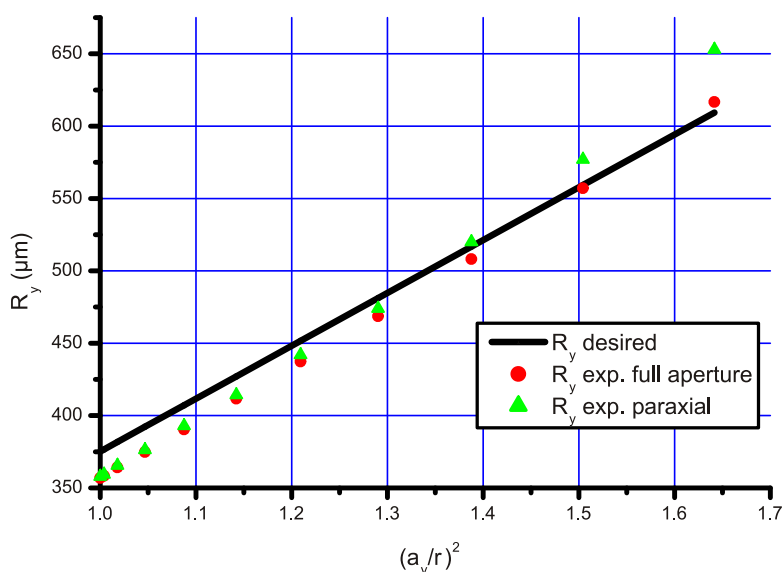

Figure A.5. Microlens radius of curvature R_y as a function of the size of the half-axis a_y, compared to Eq. (3.8).

of curvature of the circular microlens does not exactly match the desired one, mainly because of problems of the control of the RIE only having few trials. Furthermore, the steepnesses of the measured curves deviate from the theoretical ones. This can not be completely explained. For other trials of fabrication of this MLA the deviation between required and fabricated radii of curvature is constantly $+30\mu m$, independently from the ellipticity. Nevertheless, the quadratic relationship between change of lens-base and change of radius of curvature is demonstrated with sufficient accuracy. The difference between the paraxial radius of curvature and the radius of curvature fitted to the full microlens aperture grows with ellipticity, indicating increasing form deviation from a spherical profile.

Figure A.7 shows the form deviation of a circular microlens from a sphere and for the two major axes of the lens with highest ellipticity. Ripples are caused by oscillations of the profiling instrument while moving over the surface to be measured. The change of amount of form deviation with increasing ellipticity is presented in Fig. A.8. The form deviation from a sphere increases drastically with increasing ellipticity, for lenses where the form deviation of
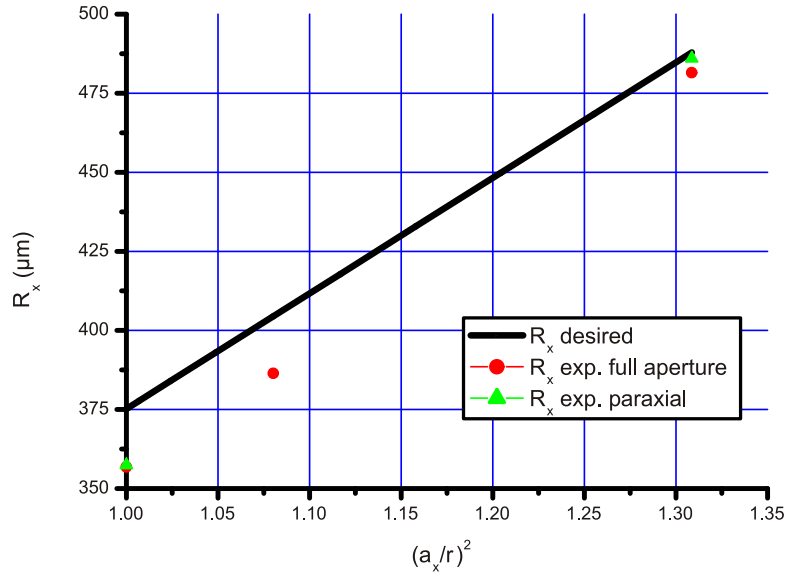
Figure A.6. Microlens radius of curvature R_x as a function of the size of the half-axis a_x, compared to Eq. (3.8).
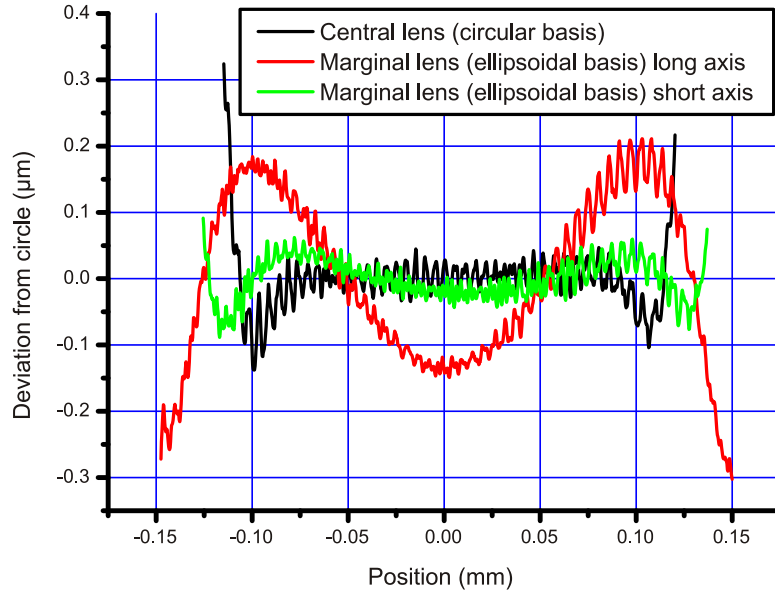

Figure A.7. Deviation of measured microlens profiles from a circle. Circular microlens: $R = 357\mu$m. Ellipsoidal microlens: Long axis: $R_y = 614\mu$m, short axis: $R_x = 482\mu$m.

the corresponding circular microlens is small.

Conclusion: In the analyzed parameter space of change of the size of the lens-bases the microlens height stays approximately constant over an MLA [199]. The major radii of curvature of the anamorphic microlens can thus be tuned by the size of the ellipsoidal lens-base using Eq. (3.8).
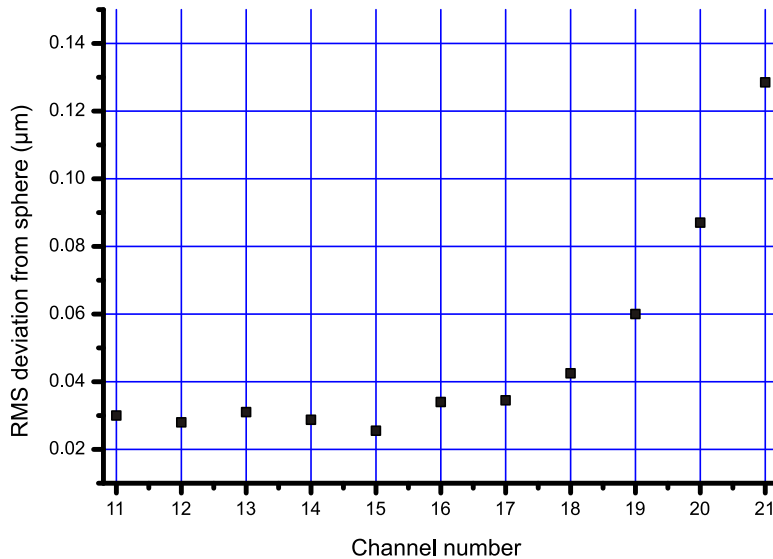
Figure A.8. Change of deviation from circle with increasing ellipticity.

B Further Simulation Methods of APCO

Multi-channel characterization. Figure B.1 presents the random raytracing simulation of an MLA on the front side of a glass substrate and a pinhole array in an absorbing layer on the backside of the substrate in the microlenses' focal plane.

Using this "image analysis" tool, different test patterns are generated which fill the FOV of the objective. Test patterns are objects with different numbers of LPs or an alphabet. The full micro-image in the focal plane of each microlens is generated by raytracing. The power of the considered channel is extracted by the pinhole at the corresponding position. The moiré-magnified images of the test patterns are examined at the position right after the pinhole array. The pixel size in the image plane for visualization, is set equal to the channel size. The presented value of efficiency is the ratio of the number of rays which hit all pinholes relative to the number of rays which started in the object going through the area of the APCOs front face. Aberration effects can be observed using this simulation method of image analysis but diffraction effects are not taken into account.

The glass plate thickness of the tested system is 300μm with a refractive index of 1.52. Pitch and diameter of the microlenses are 90μm and 85μm, respectively. This results in a NA of the microlenses of 0.21 and a FOV of each channel of 24°x24°. The diameter of the Airy disk at $\lambda = 500$nm is 3μm according to Eq. (2.16). As a result of sensitivity considerations the pinhole diameter should also be 3μm. However, to test the influence on resolution, not only different numbers of channels and pitch differences Δp are tested but also different pinhole diameters. The object distance is 500mm.

For the 3μm pinhole diameter, the Nyquist frequency can not be resolved if the channel number is larger than 20x20 because of the strong overlap of acceptance angles. In this simulation method $\Delta\varphi$ is only determined by the ratio of the pinhole diameter and the focal length. The ratio d/f is decreased so that the Nyquist frequency of a large number of channels actually
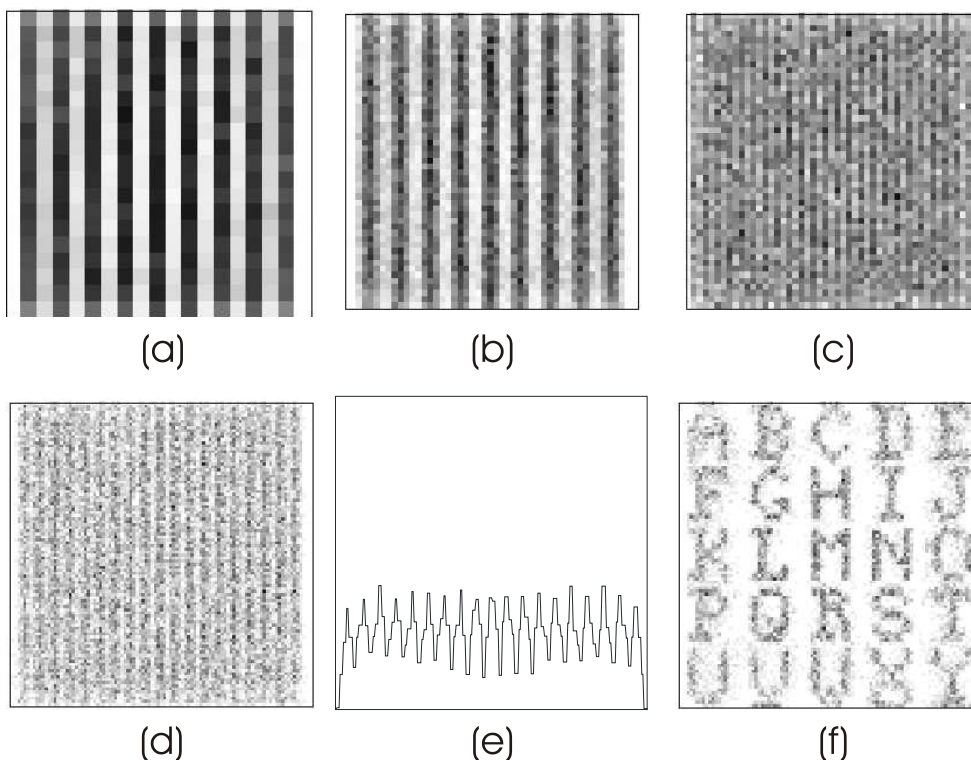
Figure B.1. Simulation of APCO in the array arrangement using the raytracing software ZEMAX$^{\text{TM}}$ and implementation of an MLA and a pinhole array (tool: Image analysis). The images are coarse due to the influence of shot noise even for a calculating time of one day (PC, 2GHz). (a) 20x20 channels, $d = 3\mu$m, $\Delta p = 5\mu$m, image of 10LP/FOV, efficiency 0.06%. Nyquist frequency is fully exploited. (b) 50x50 channels, $d = 3\mu$m, $\Delta p = 1.7\mu$m, image of 10LP/FOV, efficiency 0.06%. (c) Same system as in (b), image of 25LP/FOV can not be resolved. (d) 100x100 channels, $d = 1\mu$m, $\Delta p = 0.86\mu$m, image of 20LP/FOV, efficiency 0.007%. (e) Cross section of (d). (f) Same system as in (d), test object is alphabet filling the whole FOV, $d = 0.5\mu$m, efficiency 0.002%, off-axis aberrations can be observed for the outer channels.

can be exploited with a detectable amount of modulation. But then also the sensitivity is decreased.

Many rays have to be traced in this model to excel shot noise due to statistics but only a small number is actually valuable for analysis.

Diffraction effects can be modeled implicitly using this method by calculating the convolution of the actual pinhole and Airy disk and setting the size of the pinhole in the simulation to the size of the result of this convolution.

Modulation transfer function (MTF). If the pinholes are smaller than the PSF of the microlenses, the resolution of the APCO can be estimated by determining the optical cut-off resolution of a single microlens in LP/mm from an MTF plot as shown in Fig. B.2, obtained by a raytracing software. The number of image pixels is obtained by multiplying the optical cut-off resolution in LP/mm by two times the size of the sampled micro-image behind the mi-

crolenses in millimeters. In this model aberrations and diffraction have the full contribution but the influence of the pinhole is neglected. Even off-axis aberrations can be modeled by change of the field coordinates. For this example, the optical cut-off at 10% residual modulation oc-
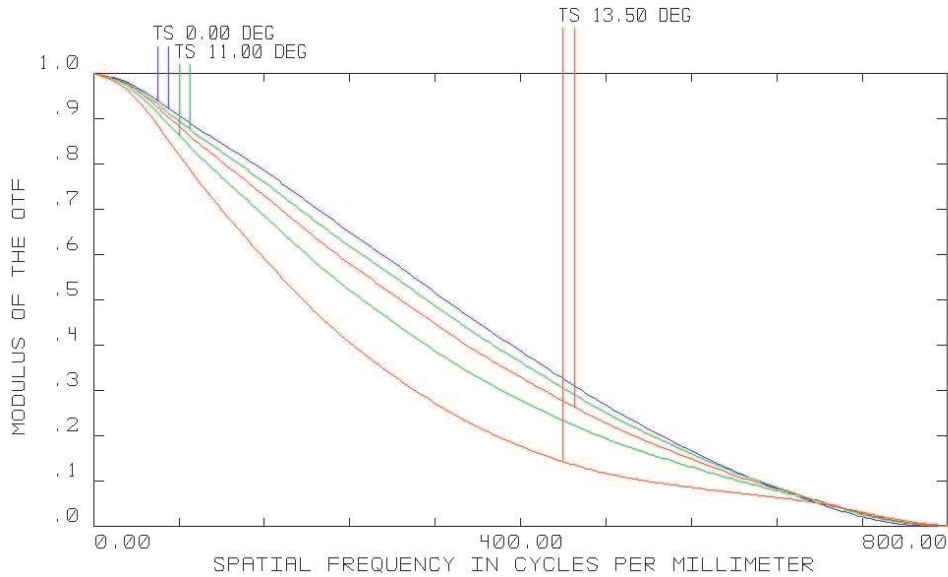

Figure B.2. Simulation of APCO using the single channel MTF. Parameters of channel: $R = 75\mu$m, $D = 68\mu$m, $n' = 1.52$, $\lambda = 0.587\mu$m, $f_{n'} = 216\mu$m. AOIs 0°, 11° and 13.5° are analyzed.

curs at approximately 600LP/mm. The image field size of a single channel is $D/\sqrt{2} = 48\mu$m. Consequently, approximately 30LPx30LP being equivalent to 60x60 pixels can be resolved by a single channel and thus by the overall APCO if the correct interommatidial angle and small pinholes are supplied.

The influence of the pinhole size can be estimated in this model by calculating the convolution of the actual pinhole and the Airy disk and by subsequent defocussing of the system or changing the $F/\#$ by the amount necessary to achieve a spot size similar to that of the result of the convolution.

Imaging of bar targets. Imaging bar targets using a single microlens provides valuable information about the change of resolution over the FOV of the single channel. If all channels possess equivalent microlenses this consequently determines the performance of the overall array. Diffraction effects and the influence of the pinhole aperture size are not included in this model. In Fig. B.3 (a) the geometric image analysis for a channel with the same properties as in the previous paragraph is presented for an object of 23LP filling the FOV of 20°. The image is sharp in the central region but gets heavily blurred with increasing field coordinate as a result of off-axis aberrations. By defocussing the system by -10μm (Fig. B.3 (b)) a more homogeneous resolution over the FOV results, being worse in the central region of the image but better at the rim, than for a system optimized for on-axis performance. The effect of field curvature is balanced.
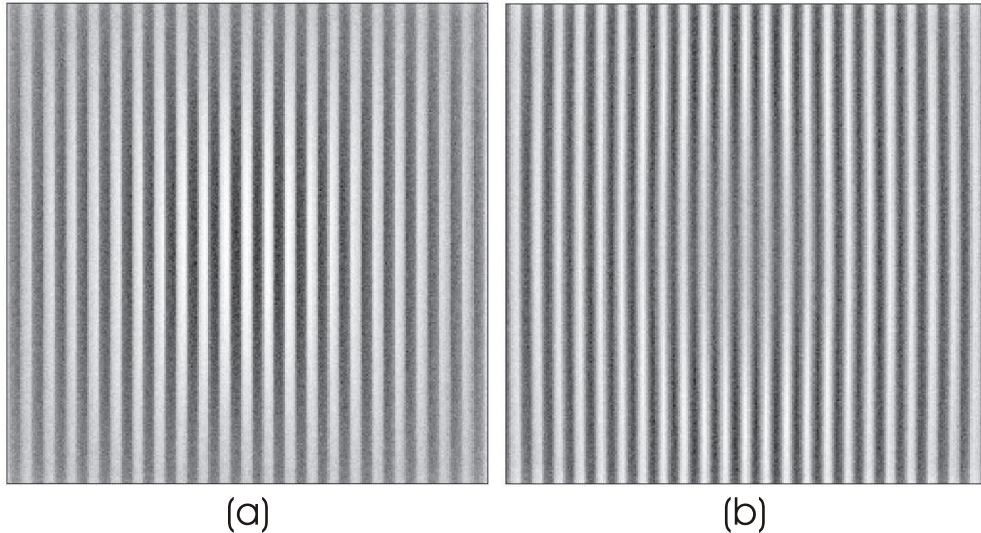
Figure B.3. Geometric image analysis of single channel. (a) Thickness 216μm. (b) Thickness 206μm.

Field curvature is a problem for large FOVs. The system thickness can be either tuned in order to have a sharp central region, or a sharp rim of the image. A sharp intermediate position is a compromise for all fields. Since human observers are used to a loss of resolution at the rim of field, having an acute zone is not a problem. It delivers, at least in a limited region, the highest resolution. Optimizing the system for on-axis performance thus seems most reasonable. However, care must be taken when considering fabrication tolerances. If the system gets longer than for optimum on-axis performance there is no effort for off-axis performance. Consequently, the design thickness should have a slight retardation to smaller thickness.

The effect of the pinhole size on resolution can be included in this model by moving a pinhole over the imaged bar target and measuring the coupled power as function of the lateral position of the pinhole in the image field. Figure B.4 shows results of moving pinholes with 5μm and 2μm diameters, respectively, over the imaged bar target in Fig. B.3 (b). For the pinhole with 5μm diameter a much higher sensitivity is achieved, however, the contrast, defined by

$$C = \frac{P_{max} - P_{min}}{P_{max} + P_{min}} \tag{B.1}$$

where P_{max} and P_{min} are the maximum and minimum coupled powers, respectively, is only 4%. Using the 2μm pinhole a contrast of 10.7% results, thus a much better resolution is achieved.

If diffraction effects shall be considered using this model, similar actions as in the paragraph about multichannel characterization to modify the pinhole size in simulation, have to be carried out.
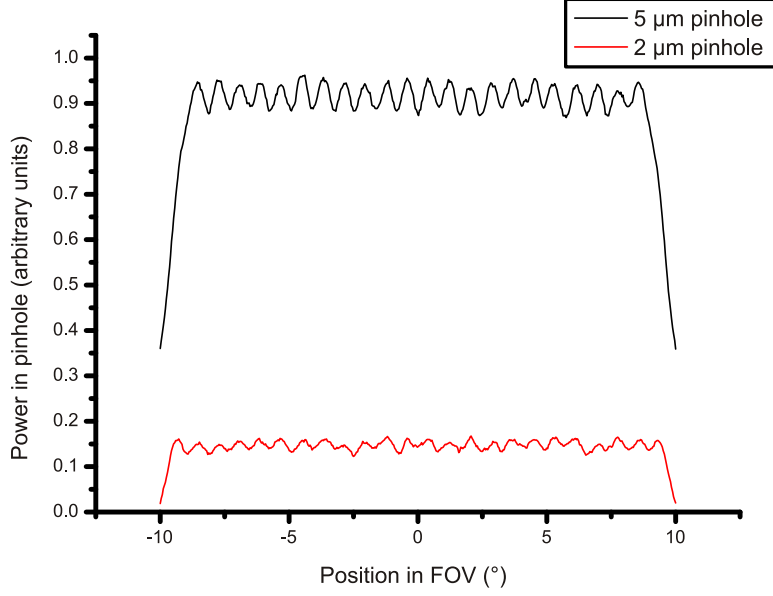
Figure B.4. Simulation of moving pinhole over bar target imaged by single channel.

C Elements of the CLEY Paraxial Transfer Matrix

$$M_{11} = \left(1 - \frac{F}{f_2}\right)\left[1 - \frac{(B - f_1)}{f_f}\right] - \frac{F}{f_f}\cdots$$
$$-\frac{\left[\left(1 - \frac{F}{f_2}\right)\left(1 - \frac{(B-f_1)}{f_f}\right) - \frac{F}{f_f}\right]f_1 + \left(1 - \frac{F}{f_2}\right)(B - f_1) + F}{f_1} \tag{C.1}$$

$$M_{12} = \left[\left(1 - \frac{F}{f_2}\right)\left[1 - \frac{(B - f_1)}{f_f}\right] - \frac{F}{f_f}\right]f_1 + \left(1 - \frac{F}{f_2}\right)(B - f_1) + F \tag{C.2}$$

$$M_{13} = \left(1 - \frac{F}{f_2}\right)(B - f_1)\frac{N}{f_f}(p_1 - p_f) + F\frac{N}{f_f}(p_1 - p_f) + F\frac{N}{f_2}(p_1 - p_2) - Np_1 \tag{C.3}$$

$$M_{21} = \frac{-1}{f_2}\left[1 - \frac{(B - f_1)}{f_f}\right] - \frac{1}{f_f} - \frac{\left[\frac{-1}{f_2}\left(1 - \frac{(B-f_1)}{f_f}\right) - \frac{1}{f_f}\right]f_1 - \frac{1}{f_2}(B - f_1) + 1}{f_1} \tag{C.4}$$

$$M_{22} = \left[-\frac{1}{f_2}\left(1 - \frac{(B - f_1)}{f_f}\right) - \frac{1}{f_f}\right]f_1 - \frac{1}{f_2}(B - f_1) + 1 \tag{C.5}$$

$$M_{23} = \frac{-1}{f_2}(B - f_1)\frac{N}{f_f}(p_1 - p_f) + \frac{N}{f_f}(p_1 - p_f) + \frac{N}{f_2}(p_1 - p_2) \tag{C.6}$$

D Further Conditions Determining the CLEY Performance

Segmentation of detector and FOV. The segmentation of the detector and the FOV are given by the total number of channels N_{tot}

$$N_{tot} = \frac{D_e}{a} \tag{D.1}$$

and

$$N_{tot} = \frac{\alpha_{in}^{max}}{\alpha_{in}^{ind}}. \tag{D.2}$$

F/# of image formation. For consideration of sensitivity and diffraction limited resolution of the image formation it is essential to determine the channel's $F/\#$. This is given by the half angle γ of the image forming light cone in the central channel for light incident parallel to the optical axis

$$\gamma = \alpha_{out} \left(\alpha_{in} = 0, N = 0, h_{in} = p_1/2 \right) = M_{21} \frac{p_1}{2}. \tag{D.3}$$

For a system without field lenses this can be simplified to

$$\gamma = \left(\frac{B - f_1 - f_2}{f_1 f_2} \right) \frac{p_1}{2}. \tag{D.4}$$

Tilted optical axes. The FOV of the overall arrangement shall be divided into the channel's FOVs. Each channel has to look in a different direction in object space. The optical axes of the telescopes have to have a certain amount of tilt which depends on the number of the considered channel. This is given by the condition $\alpha_{out} (h_{in} = 0) = \alpha_{in}$ for all angles of the optical axes $\alpha_{in} = 2N\alpha_{in}^{ind}$. It is found that

$$\alpha_{out} \left(h_{in} = 0, \alpha_{in} = 2N\alpha_{in}^{ind} \right) = 2N\alpha_{in}^{ind} = M_{22} 2N\alpha_{in}^{ind} + M_{23}. \tag{D.5}$$

This can be simplified to

$$0 = \frac{-1}{f_2} \left(p_2 - p_1 - \frac{B - f_1}{f_f} (p_f - p_1) \right) \dots$$

$$-\frac{(p_f - p_1)}{f_f} + \left[\frac{-1}{f_2} \left[f_1 + (B - f_1) \left(\frac{-f_1}{f_f} + 1 \right) \right] - \frac{f_1}{f_f} \right] 2\alpha_{in}^{ind}. \tag{D.6}$$

In case of telescopes without field lenses Eq. (D.6) becomes

$$2B\alpha_{in}^{ind} = p_1 - p_2. \tag{D.7}$$

System length. The total system length is given by

$$L = B + F. \tag{D.8}$$

Pitch and focal widths of field lens array. In a similar way conditions for the focal width and pitch of the field lenses are calculated. One paraxial ray matrix for the propagation into the plane of the field microlens and one for the propagation into the plane of the relaying microlens are established by truncation of Eq. (5.1) at the corresponding positions.

First, the field lenses shall be centered on the optical axes of the telescopes. This leads to $h_{out}^{field}(h_{in} = 0, \alpha_{in} = 2N\alpha_{in}^{ind}) = 0$. The condition for the pitch of the field lens follows:

$$p_f = p_1 - f_1 2\alpha_{in}^{ind}. \tag{D.9}$$

Second, all rays entering the focusing microlens at the center shall also propagate through the center of the relaying microlens, thus $h_{out}^{relay}(h_{in} = 0) = 0$ independently of the AOI α_{in} and the considered channel N. The required independence of α_{in} leads to

$$f_f = \frac{f_1}{B}(B - f_1). \tag{D.10}$$

The independence of N leads to

$$f_f = \frac{f_1 p_f - p_1 f_1 + p_1 B - B p_f}{p_1 - p_2}. \tag{D.11}$$

E Paraxial Conditional Equations of CLEY

$$p_1 = \frac{\gamma D_e}{\alpha_{in}^{max}} \tag{E.1}$$

$$p_f = \frac{\gamma D_e(-2\alpha_{in}^{max} f_1 + 2\alpha_{in}^{max} L + D_e)}{\alpha_{in}^{max}(2\alpha_{in}^{max} L + D_e)} \tag{E.2}$$

$$p_2 = \frac{\gamma D_e(2\alpha_{in}^{max} F + D_e)}{\alpha_{in}^{max}(2\alpha_{in}^{max} L + D_e)} \tag{E.3}$$

$$f_1 = \frac{D_e(L - F)}{2\alpha_{in}^{max} F + D_e} \tag{E.4}$$

$$f_f = \frac{2\alpha_{in}^{max} f_1(L - f_1)}{2\alpha_{in}^{max} L + D_e} \tag{E.5}$$

$$f_2 = \frac{2\alpha_{in}^{max} F(L - F)}{(2\alpha_{in}^{max} L + D_e)} \tag{E.6}$$

$$B = L - F \tag{E.7}$$

$$\alpha_{in}^{ind} = \frac{\gamma D_e}{2\alpha_{in}^{max} L + D_e} \tag{E.8}$$

$$N_{tot} = \frac{\alpha_{in}^{max}(2\alpha_{in}^{max} L + D_e)}{\gamma D_e} \tag{E.9}$$

$$a = \frac{\gamma D_e^2}{\alpha_{in}^{max}(2\alpha_{in}^{max} L + D_e)} \tag{E.10}$$

For simplification, the value of f_1 was substituted in the above equations for p_f and f_f.

The NAs of the microlenses of the central channel in air are calculated by Eq. (2.15). For the focusing microlens holds $D = p_1$ and thus

$$\text{NA}_1 = \sin\left(\arctan\left(\frac{p_1}{2f_1}\right)\right). \tag{E.11}$$

The minimum required size of the field lens is given by the double of the intermediate image height $f_1 \alpha_{in}^{ind}$. The NA of the field lens is given by

$$\text{NA}_f = \sin\left(\arctan\left(\frac{f_1 \alpha_{in}^{ind}}{f_f}\right)\right). \tag{E.12}$$

The minimum required free aperture of the relaying microlens is calculated by the demagnified aperture of the focusing microlens, given by $p_1(B - f_1)/f_1$. The NA of the relaying lens is represented by

$$\text{NA}_2 = \sin\left(\arctan\left(\frac{p_1(B - f_1)}{2f_1f_2}\right)\right). \tag{E.13}$$

F Paraxial Optical Input and Geometrical Output Parameters of Analyzed CLEYs

Table F.1. Paraxial optical input and geometrical output parameters of analyzed CLEY systems.

Paraxial input parameters	Paraxial example system	Circular arrangement of toroidal microlenses	Rectangular arrangement of toroidal microlenses. Starting system of CLEY fabricated by microoptics technology
Detector extension D_e (mm)	4.5	1.5	4.0
Half angle of overall FOV α_{in}^{max} (°)	35	13.5	45
Desired NA of focusing γ	0.2	0.03	0.05
Total system length L (mm)	2	1.2	1.5
Distance from relaying MLA to detector surface F (mm)	1	0.4	0.5
Paraxial output parameters	Paraxial lenses in air		
Pitch of focusing MLA p_1 (μm)	1475	199	255
Pitch of field MLA p_f (μm)	1271	167	202
Pitch of relaying MLA p_2 (μm)	1216	163	192
Focal width of microlenses in focusing lens array f_1 (μm)	787	711	836
Focal width of microlenses in field lens array f_f (μm)	168	79	137
Focal width of microlenses in relaying lens array f_2 (μm)	176	73	124
Half angle of individual FOV α_{in}^{ind} (°)	7.45	1.3	1.8
Number of channels N_{tot}	$4.7 \approx 5$	$10.3 \approx 11$	$24.94 \approx 25$
Detector segment width a (μm)	957	144	160
Distance from focusing MLA to relaying MLA B (mm)	1	0.8	1
NA of focusing lens NA_1	0.684	0.139	0.151
NA of field field NA_f	0.520	0.199	0.188
NA of relaying lens NA_2	0.751	0.169	0.198

G Concentrator- or Integrator Array

For the use of the array of microlens telescopes as a spatial integrator or concentrator all AOIs shall meet in one point in the focal plane of the overall system. This can be achieved for all angles which coincide with the angles of the optical axes of the different channels. These ray bundles meet in one point which is the point of intersection of all channel's optical axes. Now

the Gabor condition from Eq. (5.5) may not be applied anymore. The focusing condition of the telescopes is the same as in Eq. (5.3). The determination of the paraxial parameters is done without considering the field MLA.

A well known condition for an optical system to work as a spatial integrator array is that $\text{Det}(\tilde{M}) = 0$ [173, 176]. This shall not be used at this point. The required performance can be more easily achieved by setting the condition $h_{out}(\alpha_{in}) = 0$ for all angles of the optical axes $\alpha_{in} = 2N\alpha_{in}^{ind}$. The concentrating point is the point of intersection of the different channels' optical axes. This is achieved if

$$h_{out}\left(\alpha_{in} = 2N\alpha_{in}^{ind}\right) = 0 = M_{12}2N\alpha_{in}^{ind} + M_{13} \tag{G.1}$$

is valid. Eq. (G.1) can be simplified to

$$0 = -2\alpha_{in}^{ind}Bf_2 - 2\alpha_{in}^{ind}Ff_2 + 2\alpha_{in}^{ind}FB - Fp_1 + Fp_2 + p_1f_2. \tag{G.2}$$

Using Eq. (G.2) and Eqs. (5.3), (D.7), (D.4), (D.8) in a same way as for the CLEY in Section 5.2.2, the equation system of the paraxial parameters of the compound eye concentrator is calculated. There follows a system as presented in Fig. G.1. Each angle is transferred by a
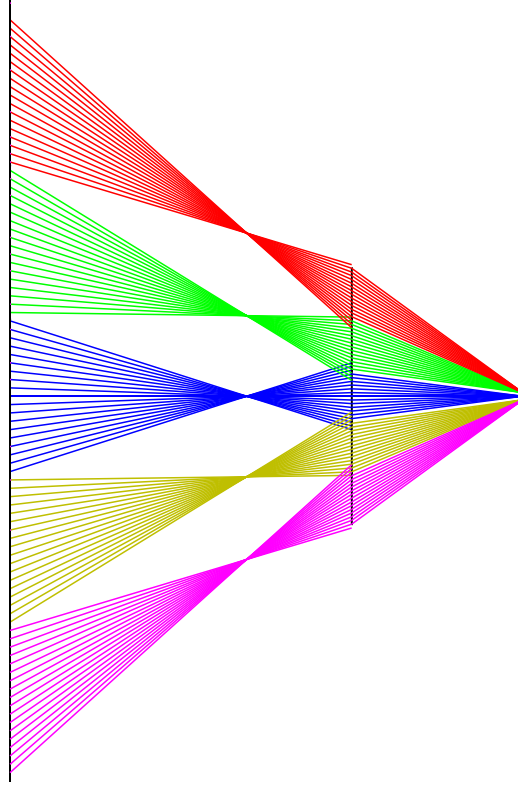

Figure G.1. Working principle of the microoptical telescope compound eye as a concentrator array, all AOI are matched to the angles of the optical axes. Used parameters: $p_1 = 2.25$mm, $p_2 = 0.75$mm, $f_1 = 3.462$mm, $f_2 = 0.952$mm, $B = 5$mm, $F = 2.5$mm, AOIs: $\kappa_0 = 0°$, $\kappa_1 = +/-17.19°$ and $\kappa_2 = +/-31.4°$.

separate channel, but rays of all field angles are focused into the same image point. The size of the concentrated spot is given by $2\Xi = 2h_{out}\left(\alpha_{in}^{ind}\right)$. It follows

$$2\Xi = 2h_{out}\left(\alpha_{in}^{ind}\right) = 2M_{12}\alpha_{in}^{ind} \tag{G.3}$$

which can be simplified to

$$2\Xi = 2\alpha_{in}^{ind}\left(-Bf_2 - Ff_2 + FB\right).$$ (G.4)

The smaller the angular segmentation is (the more channels are used) the smaller are the partial-images. Many channels mean many optical axes and thus many rays meeting in the central point. However with this approach it will definitely not be possible to use the full array to gather all the light into this small image but only small segments. Certain channels work for a certain angular region.

H Non-Sequential Raytracing Analysis of CLEY

The CLEY was simulated with non-sequential raytracing software (Fig. H.1). The metal layers are 200nm thick chromium modeled by a refractive index of 3.18 and extinction coefficient of 4.41 at $\lambda = 563$nm [223].

In Fig. H.2, exemplary detector images for different AOIs of a 2°x2° extended source are presented. The signal spot can be clearly resolved, as well as spurious light is observed in the image plane as a result of cross talk between channels in the imaging system.

The ratio of maximum signal intensity to maximum spurious intensity and the corresponding integrated signal power in the image spot and integrated spurious power, distributed over the image plane, are calculated. They are referred to as the signal to noise ratio (SNR) of useful and spurious light. A small SNR means a low image contrast.

Figure H.3 shows the corresponding diagram of the SNR of maximum intensity and integrated power vs. AOI. The observable oscillation of the signal to noise ratio in Fig. H.3 is a result of the overlap of marginal fields transmitted by two channels at the same time, thus delivering two times the power compared to the center field of a channel. As a function of AOI, the maximum intensity-SNR changes from 5 up to 300 and the integrated power-SNR from 2 up to 100.

In Fig. H.4 (a) a representation of the spatial distribution of image signal and spurious light in the image plane of the CLEY is given as a function of AOI in linear scale. Useful light can be distinguished from spurious light. Bar targets were also imaged in the non-sequential model in Fig. H.4 (b) and (c). It can be concluded that even if the effect of spurious light reduces the image contrast, images of a spatial frequency of at least 1LP/° can be resolved.

A further, very simple way to find ghosts as a result of channel cross talk, without complex non-sequential raytracing, can be performed by simply searching for rays which at the same time pass through the focusing and relaying microlenses of different channels. In contrast to highly symmetric relaying array optics [151,157] such instances occur very rarely in the CLEY, because the pitches of the different microlens- and aperture arrays have no rational relation. However, the lateral repeating of the superstructure of the Gabor superlens and consequently spurious light are a natural property of this arrangement of MLAs (see Section 2.2).
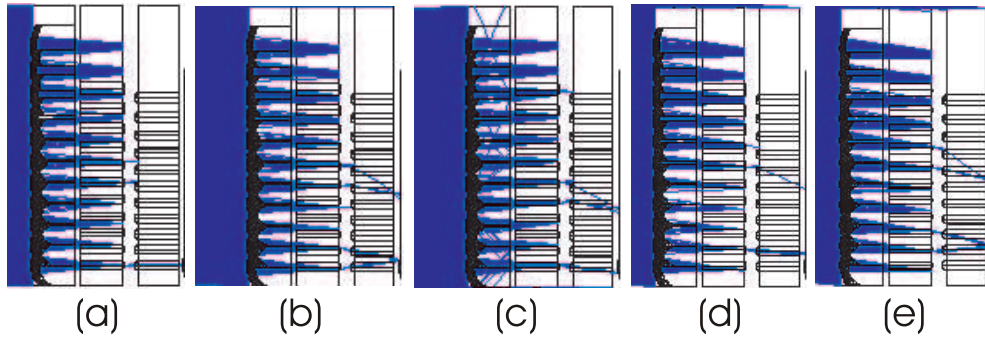
Figure H.1. Side view of non-sequential raytracing implementation of CLEY (upper part) showing the desired light paths and the cross talk under different AOIs. (a) 0°. (b) 1.8°. (c) -1.8°. (d) 3.6°. (e) 5.4°.
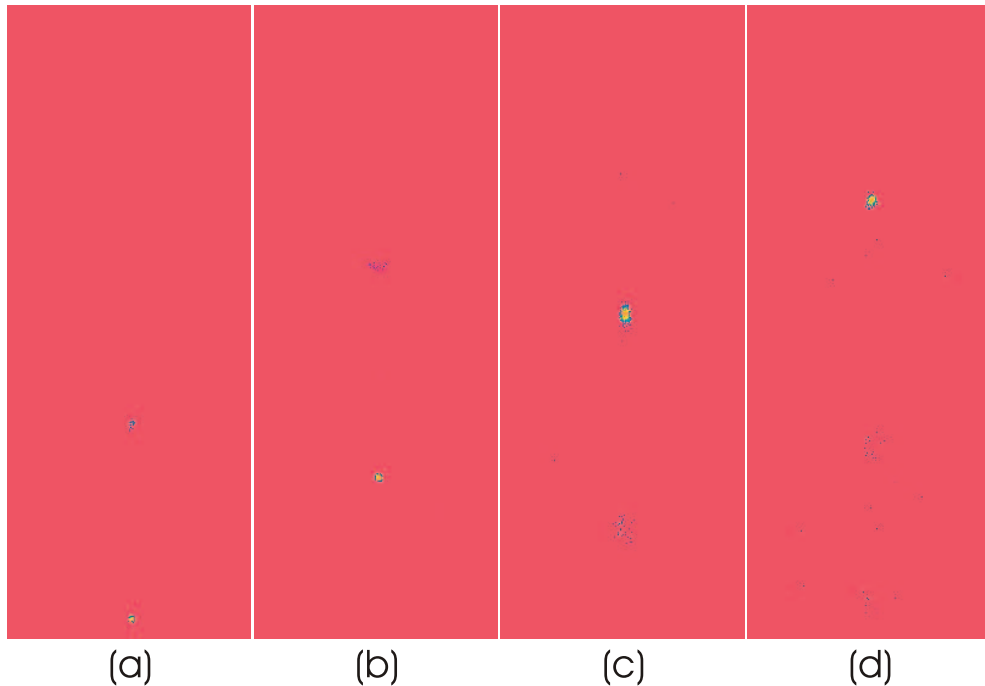

Figure H.2. Images of a 2°x2° extended source moving through the upper half of FOV of the CLEY, logarithmic scale. The cross talk of the imaging system's channels is visible in the ghost spots. AOIs: (a) 0°, (b) 12.6°, (c) 27.0°, (d) 36.0°.

I Future Working Tasks

The following future working tasks with respect to design, adaption to applications and technology were derived in order to develop bioinspired microoptical vision from the proof of principle to commercial applications:

APCO.

1. Correction of distortion by adequate position of pinholes / photo detectors.

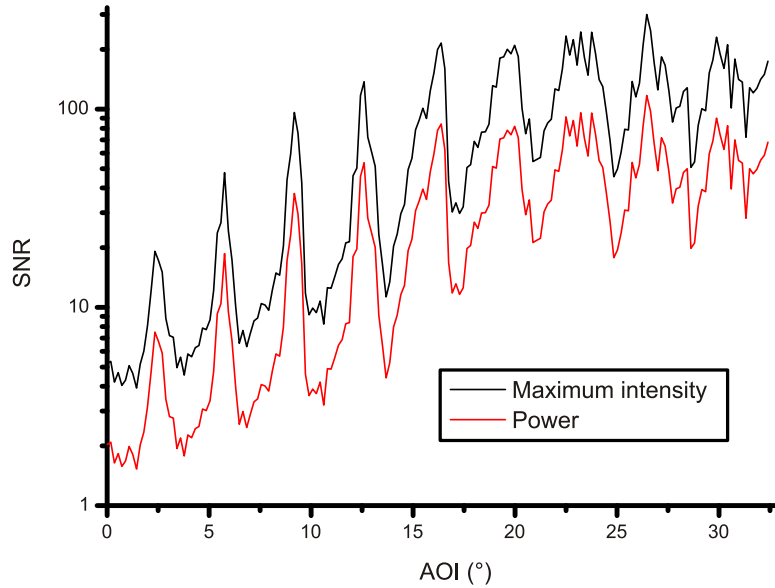2. Opaque walls for channel separation:

Figure H.3. SNR of maximum intensity in image plane and integrated power as a function of AOI.

Polishing of spacing structure after filling grooves within the structured SU8 columns with black matrix polymer in order to achieve a flat surface prior to MLA replication.

Embossing of cones in the substrates backside where the MLA is replicated on the front side, possibly in the same process. Subsequent filling of grooves with absorbing polymer.

Fabrication of master structures for replication of grooves using high-aspect-ratio processes such as the Bosch process (silicon deep etching, DRIE), precision diamond turning or milling, wafer saw, laser cutting, ultrasonic milling or the LIGA process.

Exposure of the polymer or glass substrate with a high power (excimer) laser through a photo mask with the effect of the material blackening in the form of opaque walls.

3. Replacement of the pinhole mask in titanium with some material which is more absorbing than reflecting (black polymer - problems with fine structuring, dark silicon or dark chromium mask material from semiconductor industry.

4. Arrays of off-axis aspherical microlens segments with varying microlens decentration and arrays of microprisms with varying orientation and prism angle:

If necessary to match to fabrication technologies, microlens structures can also be transfered to Fresnel- or diffractive implementations. Efficiency will suffer and strong dispersion could avoid the use for the full visible spectrum.

Technologies to evaluate: Laser beam writing, laser ablation, single point precision diamond turning (fast tool servo) or milling or presculpting of photo resist using additive lithography [224] and subsequent reflow with adapted time schedule. Subsequent polishing by a CO_2 laser or application of a smooth layer by spray coating might be necessary for technologies which produce rough surfaces to avoid strong scattering.
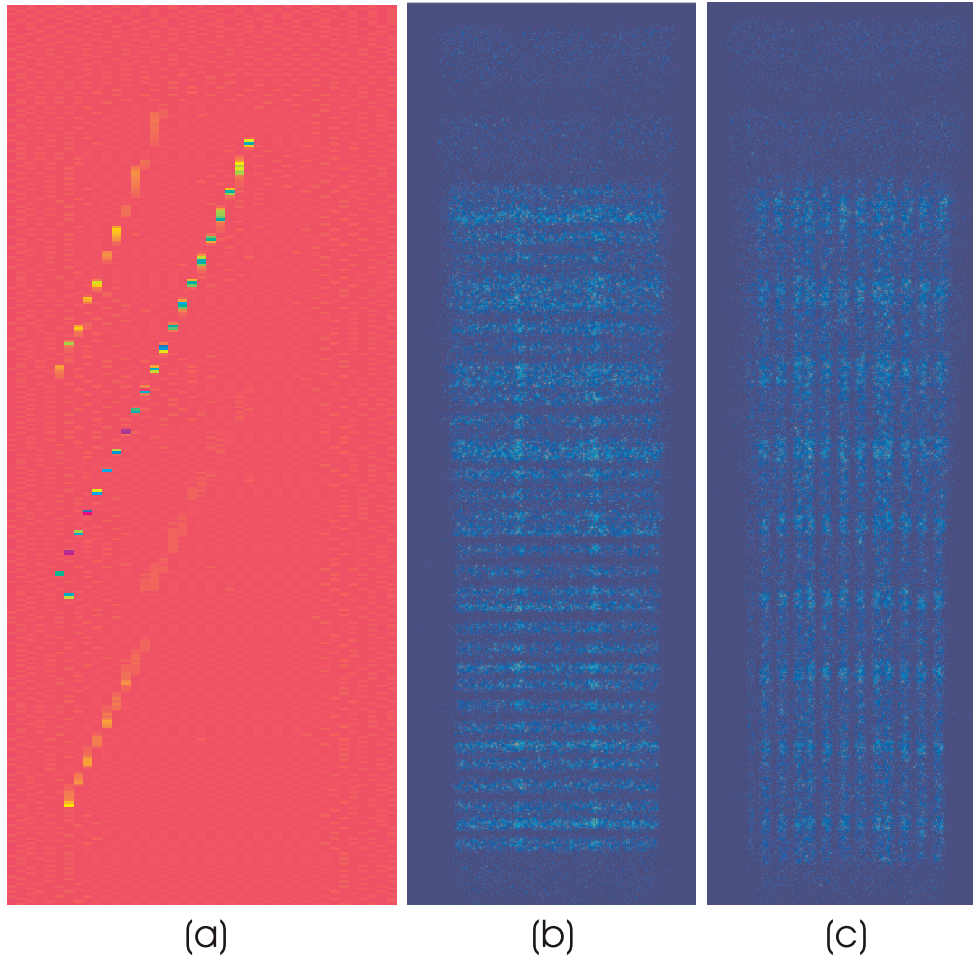
Figure H.4. Results of non-sequential raytracing analysis of the CLEY. (a) Representation of spurious light in full CLEY (channels -10..0..10) in linear scale for all AOIs at the same time. Detector images such as in Fig. H.2 but in linear scale are horizontally summed over all columns. For each AOI consequently only one column represents the intensity distribution on the detector in the direction of increasing AOI. For increasing AOI from 0° to 36°, the corresponding columns are then attached from left to right forming the presented figure. The central bright spots represent the image spots shifting with the change of AOI. The upper and lower sets of spots correspond to the spurious images which occur because of cross talk of different channels. (b) Non-sequentially imaged horizontal bar target (only upper half of FOV shown, due to symmetry). (c) Non-sequentially imaged vertical bar target.

Crossing of one-dimensional prism arrays with varying prism angle, if easier to fabricate (precision diamond milling).

5. Adoption of the focal lengths of the lenses in the MLA in order to compensate for the defocussing an additional diverging (Fresnel-) lens for FOV-enlargement introduces. Anamorphic lenses might be necessary.

6. Correction of chromatic aberrations in case of color imaging by the use of one channel for each color and viewing direction, also as ellipsoidal lenses. Radii of curvatures of the

lenses are individually tuned to allow a perfect focusing on the photo sensitive pixels for each color and viewing direction. Color filters can be applied on the microlenses or on the photo sensitive pixels.

7. Reflow on pedestals [196]. There results one more degree of freedom for fabrication of chirped MLAs. Lens volume determination is decoupled from size of lens-base.

8. Sub-ASF resolution for point sources by differential measurement of signals of adjacent channels and calculation of the center of gravity with respect to the contributing channels.

9. Combination of the APCO with a tunable liquid lens, based on electrowetting technology [225–227]. This allows a zoom function (variable FOV) without moving parts.

   Furthermore the resolution can be increased by taking of pictures with different magnification and subsequent calculation to one overall image.

10. Examination of use of several photo sensitive pixels per channel. Expected effects: Resolution enhancement (small pixels), sensitivity enhancement by several channels effectively starring into the same direction and use of neural superposition principle, obtaining of angular information by application of several pixels axially displaced behind the pinhole, decreasing of number of channels and resulting decreasing of lateral objective size, zoom, polarization detection, enhanced color resolution (spectrometer).

11. Examination of adaption of shape of pinhole to shape of spots under off-axis aberrations. Effects on resolution and sensitivity?

12. Replacement of microlenses by liquid crystal microlenses or combination of APCO with tunable liquid crystal apertures in the image plane, both resulting in complete new functionalities.

13. Microlens and receptor arrays on a curved basis: Fabrication of MLAs on a curved basis is realistic (laser beam writer, modified DWL 400, Heidelberg Instruments), but the fabrication of the corresponding photo detector array appears to be difficult. Alternatively the planar fabrication of microlens and receptor arrays on a thin flexible sheet and subsequent application to a curved basis can be thought of. Thinned (CMOS) photo detectors are currently under development. For cylindrical curvatures the bowing seems promising, for spherical curvatures stress will cause problems. The idea of the flexible sheet has the further advantage that the FOV could be decoupled from fabrication issues and determined in the application just by the deformation of the camera (acceptance angle of ommatidia must still match to interommatidial angle).

CLEY.

1. In contrast to the here analyzed arrangement where each object point is transmitted by only one channel, a more superposition like system should be analyzed. The contribution of several channels to the image formation of one object point will increase the sensitivity drastically. The partial-images transferred by adjacent channels shall not only be in annexation anymore but have strong overlap. The geometrical arrangement of the MLAs will stay the same. The relative size of the field apertures has to be increased. In the paraxial design the size of the intermediate image must be minimized. The segmentation of the system in more channels would be advantageous. Effects of strong off-axis aberrations and also coherence have to be analyzed.

2. Extension of the CLEY to a telescopic arrangement of at least four microlenses for achieving telecentricity or at least to reduce the chief ray angles in image space. Accordingly, the applied paraxial 3x3 matrix formalism has to be modified.

3. Examination of soft field apertures to relax fabrication tolerances in terms of image stitching.

4. Additional aperture layers for blocking of light which passes through microlenses and apertures of different channels (cross talk).

5. Fabrication of a circular symmetric objective producing a two-dimensional image. The necessary geometry of the field apertures in the field aperture array as well as the MLA arrangement in the two-dimensional case has to be established to guarantee image annexation and optimum fill factor.

6. Examination of reflective superposition compound eyes on curved surfaces (laser beam writer) for use as X-ray objective.

Identified fields of future application of APCO and CLEY.

1. Besides the here demonstrated gray scale, contrast and edge orientation detection, furthermore, movement analysis, color vision and polarization sensitivity are of interest.

2. In medical technology e.g. as a camera on a cylindrical shell for endoscopy.

3. Application of a one-dimensional artificial compound eye on a fast rotating stage for the generation of a two-dimensional panoramic image almost free of distortion. This could allow to cover the full visual surrounding of the objective by scanning in the direction perpendicular to the artificial compound eye's one-dimensional FOV.

4. 3D vision or stereoscopic vision, distance measurement (triangulation): Different channels with large distance (basis) view the same object point under different viewing directions.

5. IR-vision: A lot of material volume and material processing for the standard IR-materials silicon and germanium can be saved using MLAs. Problems occur as a result of the scaling laws of APCOs with the large wavelength and the comparatively large detectors. However, low fill factor of conventional detector arrays and the small number of pixels suit well. Silicon could be sawed from the substrate backside for construction of grooves for opaque walls. Alternatively, polymer materials such as polyethylene or polystyrene with sufficient transparency at near IR, and suitability for microoptical fabrication processes have to be examined for application in artificial compound eyes.

   Artificial compound eye night vision could be within reach applying arrays of residual-light-amplifiers.

   An eye safe but bright illumination at $\lambda = 950$nm (NIR), where silicon has a very good response, could provide additional light for the image capturing. Persons under surveillance would not recognize the illumination.

6. Iris- and fingerprint recognition.

7. Integration of illumination (LEDs, OLEDs) into the array of light sensitive channels – there is no need to introduce a further light source into a very tight working space.

8. Combination of light sensitive and light emitting pixels distributed within one array. The resulting device is camera and display at the same time. Two of those devices on two sides of an opaque object, if correctly connected, can make this object transparent (wearable displays, camouflage, transparent walls...). Large sheets of those systems could have a unity magnification resulting in equal pitches of microlens- and pinhole arrays.

9. Encoding and decoding: There is no simple pitch difference between microlens- and pinhole arrays, which allows a direct moiré-magnification, but a variable arrangement of pinholes in channels. The knowledge of the position of the pinhole in each channel is the key information to extract encoded images.

10. General surveillance, the camera will not be recognized as such but will fit to the texture of the surrounding material.

11. Automotive engineering and machine vision. Artificial compound eyes open completely new working spaces for optical inspection because of their small system length.

12. Imaging Microspectrometer. Gratings are applied onto the microlenses. Several identical detectors within one channel determine the amount of differently dispersed light.

13. In general this means the development from "imaging", where only intensity distributions, in best case with color information, are extracted from an object to "arrayed optical sensors", where additional optical information such as temperature (bolometer arrays), polarization, exact wavelength, distance, speed, ... are extracted. This could replace the

combination of a complex optical instrument with an optical scanner to achieve laterally resolved optical information which is more than an intensity image.

Symbols and Abbreviations

α	Half angle of field of view
α_e	Half angle of field of view enlargement
α_{in}	Paraxial input ray angle
α_{in}^{ind}	Half angle of the individual channel's field of view (cluster eye)
α_{in}^{max}	Half angle of the maximum field of view (cluster eye)
α_{out}	Paraxial output ray angle
a_D	Size of detector diagonal = image circle diameter
a_{ideal}	Ideal image size (free of distortion)
a_{real}	Pinhole position within the considered channel
a	Size of a square micro-image or partial-image
a'	Size of square partial-image of relaying lens
A_c	Area surrounded by curve on a spherical surface
A_I	Area of image
A_O	Area of object
AOI	Angle of incidence
APCO	Artificial aPposition Compound eye Objective
ASF, ASF(ϕ)	Angular sensitivity function
a_x, a_y	Major and minor half-axes of ellipsoidal lens-base
a_t, a_s	Tangential and sagittal half-axes of anamorphic lens-base
β	Angle, with respect to optical axis, where no modulation can be observed anymore in a radial star pattern
B	Distance between focusing and relaying microlens array
χ_{LP}	Number of observed line pairs
$\chi_{LP/deg}$	Number of line pairs per degree
$\chi_{LP/FOV}$	Number of line pairs over field of view
χ_{P/A_I}	Number of pixels in image area of objective
c	Radius of spherical surface
C	Contrast
CCD	Charge coupled device

Symbols and Abbreviations

CLEY	CLuster EYe
CMOS	Complementary metal oxide semiconductor
CO_2	Carbon dioxide
c_x, c_y, c_z	Half-axes of ellipsoidal lens
ϵ	Chief ray angle in object space
ϵ'	Chief ray angle in image space
$\epsilon_{i,j}$	Chief ray angle as a function of the considered channel's coordinate
ϵ_{ideal}	Ideal chief ray angle in object space (free of distortion)
ϵ_{real}	Real chief ray angle in object space (including distortion)
$\not{A}$	Picht's operator
$\Delta\beta$	Tilt in paraxial formalism
Δp	Pitch difference between microlens- and pinhole- or detector array
$\Delta\varphi$	Acceptance angle
$\Delta\varphi_1$, $\Delta\varphi_2$	Acceptance angle of large and small lens
$\Delta\Phi$	Interommatidial angle
$\Delta\rho$	Geometrical contribution to acceptance angle
Δx	Decentration of optical surface in paraxial formalism
Δz	Propagation distance in paraxial formalism
d	Diameter of circular photo receptor, detector or pinhole; Size of square detector pixel
$\hat{d}$	Transmittance distribution of circular pinhole
d_F	Lateral focus dimension (diameter of Airy disk)
d_{F_1}, d_{F_2}	Lateral focus dimension of large and small lens
D	Diameter of circular lens or stop
D'	Diameter of circular relaying lens
D_1, D_2	Diameter of circular large and small lens
D_e	Detector extension in image space of cluster eye
DC	Direct current
ϕ	Angular distance of source point from optical axis of ommatidium
f	Focal length of lens
$f_{n'}$	Focal length in substrate material
F	Focal length of Gabor superlens
f_1, f_f, f_2	Focal length of first (focusing), field and second (relaying) lens
F_F	Focal length of Fresnel lens
$F/\#$	Stop number
$F/\#_1$, $F/\#_2$	Stop number of large and small lens

Symbols and Abbreviations

FOV	Field of view
FFT	Fast fourier transformation
FWHM	Full width half maximum
Γ	Distortion
γ	Half angle of image forming light cone behind telescope (cluster eye)
$G(x)$	Fourier sum of bar target
G_0	Coefficient of the DC peak
G_1	Coefficient the first harmonic
η	Relative pupil coordinate
h_L	Lens height (sag)
h_{in}	Paraxial input ray height
h_{out}	Paraxial output ray height in image plane
h_{out}^{field}	Paraxial output ray height in plane of field lens
h_{out}^{relay}	Paraxial output ray height in plane of relaying lens
i, j	Coordinates of considered channel with respect to central channel in array origin
I_I	Irradiance of image
I_I'	Irradiance of image of relaying lens
I_O	Irradiance of object
IR	Infrared
$\kappa_0, \kappa_1, \kappa_2$	Angles of incidence for demonstration of concentrator array
k	Extinction coefficient of photo pigments in receptor
k_x, k_y	Conical constants for major and minor axes of ellipsoidal lens
K	Absorption of photo receptor
λ	Wavelength of light
l	Photo receptor length
l_F	Axial focus dimension
L	Length of optical system
LIGA	Lithographie Galvanik
LP	Line pair
m	Transverse magnification
$\hat{m}$	Axial magnification
$\tilde{M}$	Paraxial transfer matrix
$\tilde{M}_{prop(\Delta z)}$	Paraxial transfer matrix for propagation of distance Δz
$\tilde{M}_{refr(f)}$	Paraxial transfer matrix for refraction at lens with focal length f
M_{11}, M_{12}, M_{13}	Elements of paraxial transfer matrix

M_{21}, M_{22}, M_{23}	Elements of paraxial transfer matrix
MA6 / MA8	Mask aligner for 6" / 8" wafers by SUSS Microtec
MEMS	Micro electro mechanical systems
MLA	Microlens array
MTF	Modulation transfer function
$\text{MTF}_{ASF}(\nu)$	Modulation transfer function by Fourier transformation of the angular sensitivity function
ν	Angular frequency
ν_{CO}	Optical cut-off frequency
ν_s	Nyquist- or sampling frequency
N	Number of considered channel in artificial compound eye along one dimension
N_{tot}	Total number of channels in artificial compound eye along one dimension
n	Refractive index of incident medium (object side)
n'	Refractive index of image side medium (substrate)
NA	Numerical aperture
NA_1, NA_f, NA_2	Numerical aperture of focusing, field and relaying lens (cluster eye)
Ω	Solid angle
OPD	Optical path difference from the perfect sphere
$\text{OPD}_{spherical}(\eta)$	Optical path difference due to spherical aberrations of spherical surface
OTF	Optical transfer function
p	Period of bar target
p_L	Pitch of microlens array
p_P	Pitch of pinhole- or detector array
p_1, p_f, p_2	Pitch of first (focusing), field and second (relaying) lens
P	Eye parameter
P_{max}, P_{min}	Maximum and Minimum coupled powers in pinhole
P_D	Power (light flux) in in circular curve with diameter D
P_I	Power (light flux) in considered image portion
P_S	Power (light flux) of source point
PC	Personal computer
PMMA	Polymethyl methacrylate
PSF	Point spread function
PV	Peak to valley

Symbols and Abbreviations

r	Radius of spherical surface (lens)
R	Radius of curvature of spherical surface (lens)
R_{EYE}	Eye radius
RIE	Reactive ion etching
RMS	Root mean square
R_x, R_y	Major and minor paraxial radii of curvature of ellipsoidal lens
R_t, R_s	Tangential and sagittal radii of curvature of anamorphic lens
$R_t(\epsilon)$, $R_s(\epsilon)$	Tangential and sagittal radii of curvature of anamorphic lens as a function of chief ray angle
σ	Decentration of optical element in paraxial formalism
s	Object distance
s'	Image distance (back focal length)
s'_t	Tangential back focal length
s'_s	Sagittal back focal length
s'_0	Paraxial back focal length
S	Sensitivity of ommatidium to extended source; ratio of irradiance in object plane and flux in photo sensitive pixel in image plane
S1, S2, S3	Substrate layers of cluster eye
S_F	Size of Fresnel lens
SFR	Signal frequency response
SNR	Signal to noise ratio
SU8	High aspect ratio photo polymer (EPOXY NOVOLAK EPON SU8))
$\vartheta_{i,j}$	Orientation of main axes of ellipsoidal lens with respect to array origin
θ	tilt of the optical axis of the considered channel
τ	Transmission of optical system
Ti	Titanium
TOMBO	Thin observation module by bound optics
u	Object side solid cone half angle
u'	Image side solid cone half angle
UV	Ultraviolet
V	Volume
VGA	Video graphics array, commonly referred to the format of 640x480 pixels
ω	Field angle, angle of incidence
x, y, z	Cartesian coordinates
$x+$, $y+$, $y-$	Tangential and sagittal directions for determination of the angular sensitivity function

Symbols and Abbreviations

$-x, +x, -y, +y$	Marginal field coordinates of one channel of cluster eye
ξ	Root mean square geometrical spot radius
Ξ	Radius of concentrated spot of integrator array
z_0	Normalization term in equation of ellipsoidal lens
ZEMAX^{TM}	Commercial raytracing program

Acknowledgements

Kurzfassung

In der vorliegenden Arbeit wurden künstliche Facettenaugenprinzipien und deren experimentelle Umsetzbarkeit mittels Herstellungstechnologien der Mikrooptik untersucht.

Seit Jahrmillionen ist das Facettenauge der Insekten in der Natur ein Erfolgsmodell. Ihr Volumen ist sehr viel kleiner als das eines klassischen Ein-Linsen-Systems, das z.B. wir Menschen als Auge besitzen und sie haben ein viel größeres Gesichtsfeld, das bis zur Rundumsicht reichen kann. Ein Insektenauge besteht aus einer Anordnung von Hunderten bis Zehntausenden sehr kleiner Linsen, angeordnet auf einer gekrümmten Oberfläche. Die zugehörigen Photorezeptoren befinden sich in der Bildebene der Mikrolinsen ebenfalls auf einer gekrümmten Oberfläche. Durch diese Anordnung nimmt die gesamte abbildende Optik nur das Volumen einer Kugelschale ein und lässt damit, im Gegensatz zu Einzelkammer Augen, Raum für das Gehirn, welches die visuellen Informationen verarbeitet. Besonders hoch aufgelöst sehen können die meisten Insekten allerdings nicht. Die Menge der Informationen die Facettenaugen anbieten, ist jedoch an die Möglichkeiten der Bildverarbeitung in einem kleinen Insektengehirn sowie den Lebensumständen (Umgebungsbeleuchtung, Geschwindigkeit der Fortbewegung, Jäger/Beute-Verhalten) perfekt angepasst.

Es gibt in der Natur zwei verschiedene Arten von Facettenaugen: Appositionsaugen, welche sich vor allem bei tagaktiven Insekten entwickelt haben und Superpositionsaugen, welche bei nachtaktiven Insekten und in der Tiefsee lebenden Wirbellosen zu finden sind.

In Appositionsaugen ist jeder Mikrolinse eine kleine Gruppe zugehöriger Photorezeptoren zugeordnet. Jede Mikrolinse fokussiert nur Licht, welches aus einer bestimmten Richtung des Objektes kommt auf seine zugehörigen Rezeptoren. Damit erzeugt jeder optische Kanal nur einen Bildpunkt. Die Gesamtheit der Signale aller Kanäle liefert dann das komplette Bild. Die verschiedenen optischen Kanäle sind durch absorbierende Pigmente voneinander isoliert, so dass kein Übersprechen stattfinden kann.

Bei Superpositionsaugen ist dieses Zusammenwirken der verschiedenen Kanäle gerade erwünscht, da dadurch die Lichtstärke des Auges deutlich erhöht werden kann. Das Objektiv funktioniert ähnlich wie eine Gabor Superlinse. Allerdings bewirken die aus der gleichzeitigen Übertragung durch verschiedene Kanäle resultierenden Aberrationen eine Verringerung der Auflösung.

Ein weiteres, sehr interessantes natürliches Sehsystem ist das der Springspinne. Obwohl es sich hier um ein kleines Tier handelt, haben sich keine Facettenaugen ausgebildet, da deren mögliches Auflösungsvermögen den Lebensumständen der Springspinne nicht genügt. Stattdessen nutzt die Springspinne mehrere Einzelkammeraugen verschiedener Auflösungsver-

mögen und Gesichtsfelder.

Natürliches Sehen ist im letzten Jahrhundert eingehend untersucht worden. Trotzdem ist bisher nur wenig Aufwand betrieben worden, um Facettenaugen als Vorbild für abbildende Systeme zu nutzen. Das Vorbild für klassische Objektive sind stets Einzelkammeraugen.

Der Bedarf nach kompakten bilderzeugenden Systemen für vielfältigste Anwendungen ist eine allgemein anerkannte Tatsache. Die Miniaturisierung optoelektronischer Bildsensoren schreitet durch Weiterentwicklungen der Halbleitertechnologie stetig voran. Die gesamte Kamera stösst in ihrer Verkleinerung allerdings an Grenzen, da die Baulänge eines klassischen Objektives an die Vergrösserung gekoppelt ist. Eine grosse Bildfläche ist auf der anderen Seite unbedingt nötig, da die einzelnen Pixel, aus Gründen der beugungsbegrenzten Auflösung und der Lichtstärke, eine gewisse Grösse benötigen und zudem für eine gute Bildauflösung auch viele Pixel gefordert werden. Diese Schere zwischen Mikrolektronik und abbildender Optik zu schliessen, ist die Motivation der Suche nach alternativen Abbildungskonzepten. Bisherige Ansätze der technologischen Umsetzung künstlicher Facettenaugenkonzepte scheiterten allerdings an der Nutzung makroskopischer Technologien zur Erzeugung mikroskopischer Strukturen. Es war eine anerkannte Annahme, dass es technisch nicht möglich sein wird, eine Vielzahl von Kanälen, wie in der Natur üblich, zu realisieren.

Es ist das Ziel dieser Arbeit zu zeigen, dass diese Limitation durch die Nutzung von in der Mikrooptik etablierten Herstellungsmethoden, wie dem Schmelzprozeß und der UV-Replikation, aufgehoben werden. Der geringe Abstand zwischen Linse und Photorezeptoren und die geringen Linsenhöhen und Durchmesser machen Facettenaugen zu einem perfekten Vorbild für kompakte, mittels Mikrooptiktechnologie erzeugte, abbildende Systeme. Es können eine Vielzahl von Mikrolinsen in hoher Präzision und Uniformität hergestellt und im Wafermaßstab sehr genau zu nachfolgenden Abstands- und Optoelektronikstrukturen justiert werden. Es resultieren dünne, einfache und monolithische abbildende Systeme, mit der Genauigkeit der Photolithographie. Natürlich ist man bei Nutzung von Technologien, die dem momentanen Stand der Technik entsprechen, im Gegensatz zu den natürlichen Vorbildern, auf planare Anordnungen begrenzt.

Bei der Untersuchung der Skalierungsgesetze abbildender Systeme stellt man fest, dass in der Mikrooptik Aberrationen nur eine untergeordnete Rolle spielen. Vielmehr wird die Menge der Bildinformationen durch Beugung an den Linsenaperturen und die Grösse der Bildfläche begrenzt. Die Winkelauflöung verringert sich mit zunehmender Miniaturisierung. Eine hohe Bildauflösung erfordert deswegen ein grosses Gesichtsfeld der Optik. Weiterhin ist die Lichtstärke eines Objektives für eine ausgedehnte Lichtquelle unabhängig von der Linsengrösse. Die Blendenzahl $F/\#$ ist bei konstanter Photorezeptorgrösse das alleinige Maß für die Lichtstärke.

Die getrennte Übertragung unterschiedlicher Objektbereiche durch verschiedene Kanäle erlaubt die individuelle Korrektur jedes Kanals für seine Blickrichtung hinsichtlich feldabhängiger Bildfehler. Es resultiert eine homogene Auflösung über das gesamte Gesichtsfeld, analog der

auf der optischen Achse. Die zur Korrektur von Astigmatismus und Bildfeldwölbung notwendigen angepassten anamorphotischen Mikrolinsen lassen sich ausgezeichnet durch die Nutzung des Schmelzprozesses auf einer elliptischen Linsenbasis erzeugen. Der Effekt der Aberrationskorrektur für schiefen Einfall wurde durch Messungen der Fokusbilder und der Abbildung von Teststrukturen belegt.

Im Rahmen dieser Arbeit wurden zwei Konzepte künstlicher Facettenaugen verifiziert – das künstliche Appositionsauge und das Cluster Auge.

Das künstliche Appositionsauge besteht aus einem Linsenarray auf der Vorderseite eines Substrates und einem Detektor- oder Lochblendenarray unterschiedlichen Pitches in dessen Bildebene auf der Substratrückseite. Das Substrat enthält idealerweise die verschiedenen Kanäle optisch isolierende Wände, um Geisterbilder durch Übersprechen zwischen benachbarten Kanälen zu verhindern. Ein Kanal erzeugt nur ein Signal, wenn sich ein Objektpunkt auf oder nahe seiner optischen Achse, welche durch Linsenzentrum und Detektor- oder Lochblendenposition vorgegeben ist, befindet. Die Bildentstehung kann als moiré-Vergrösserung erklärt werden.

Das Cluster Auge kann auf eine Mischung aus natürlichem Superpositionsauge und dem Sehsystem der Springspinne zurückgeführt werden und erzeugt ein geschlossenes Bild. Es besteht aus drei Linsenarrays unterschiedlichen Pitches, welche ein Array von Kepler-Teleskopen mit geneigten optischen Achsen und Feldlinse darstellen. Jeder Kanal überträgt nur einen geringen Teil des Objektes. Feldblenden in der Zwischenbildebene, auf den Feldlinsen, bestimmen die Blickrichtung und die Grösse des Gesichtfeldes eines jeden Kanals und daraus resultierend den Bildanschluß bzw. -überlapp in der gemeinsamen Bildebene.

Beide künstlichen Facettenaugenkonzepte erlauben eine starke Vergrösserung bei geringer Baulänge und damit ein grosses Telephotoverhältnis, deutlich grösser als das von klassischen Ein-Kanal-Objektiven.

Es mit den Mitteln der Mikrooptiktechnologie gelungen, mehrere Generationen von Demonstratoren von planaren künstlichen Facettenaugenobjektiven, basierend auf dem Appositionsaugenprinzip, zu entwickeln. Die Ur-Strukturen der Mikrolinsen wurden dabei durch den Schmelzprozess erzeugt. Diese wurden danach mittels UV-Replikation in definierter axialer und lateraler Ausrichtung zu den nachfolgenden Wand- und Lochblendenstrukturen im 4" Wafermassstab abgeformt. Die Lochblenden wurden, unabhängig davon, vorher ebenfalls mittels Photolithographie, auf der Rückseite der Abstandstruktur in Titan realisiert. Absorbierende Wände zwischen den Kanälen sind durch Lithograhie in mit hohem Aspektverhältnis strukturierbarem Photolack und nachfolgendem Verguß mit absorbierendem Polymer, erzeugt worden. Ein monolithisches Objektiv mit 128x128 Kanälen, 69μm Kanalpitch und 0.2mm Baulänge wurde direkt an einen entsprechenden CMOS-Sensor angeschlossen. Die resultierende dünne Kamera besitzt über ein Gesichtsfeld von 20°x20° eine Auflösung von 60x60 Pixeln. Die limitierte Auflösung ist nicht das Ergebnis einer zu geringen Kanalzahl, sondern der Überlappung der Gesichtsfelder benachbarter Kanäle geschuldet.

Kurzfassung

Verschiedene Möglichkeiten zur Gesichtsfelderweiterung und einer daraus resultierenden zusätzlichen Trennung der Blickrichtungen der Kanäle wurden in dieser Arbeit vorgeschlagen. Mit einer vorgeschalteten Fresnel-Zerstreuungslinse wurde das Gesichtsfeld auf 42°x42° aufgeweitet. Als am vielversprechendsten erscheinen aber arrays von gegenüber dem jeweiligen Kanalzentrum dezentrierten Linsensegmenten.

Mit seiner geringer Dicke passt dieses Objektiv beispielsweise in Kreditkarten, Folien oder Displays. Anwendungen im automobilen Bereich und in der Überwachungstechnik sind denkbar, da das Objektiv sehr flachbauend und nicht als ein solches zu erkennen ist. Die experimentell demonstrierte Abbildungsqualität ist zur Personen-, Objekt- und Bewegungserkennung ausreichend.

Basierend auf dem Cluster Augen Konzept konnte ebenfalls ein Demonstrator entwickelt werden. Das abbildende System besteht aus 21x3 optischen Kanälen, hat ein Design-Gesichtsfeld von 70°x10° und ist 2mm dick. Es wurde unter der Nutzung eines paraxialen 3x3 Matrix Formalismus entworfen und mit Hilfe kommerzieller Raytracing Software optimiert. Die drei Linsenarrayschichten wurden nach Erstellung der Linsen im Schmelzprozess mittels reaktivem Ionenätzen in die Quarzglassubstrate übertragen. Danach erfolgte die Applikation der Blenden (in Chrom) auf jeder Linsenarrayschicht mittels Lift-off oder Chrom Ätzen. Die axiale und laterale Justage der Linsenarrays im Wafermaßstab mittels Justiermarken und Haidenhein-Tastern und die Fixierung der drei Wafer stellen die letzten Arbeitsschritte dar. Auch in diesem System besitzen die Linsen des ersten Arrays eine kanalabhängige elliptische Form, zur Korrektur von ausseraxialen Bildfehlern.

Durch die Abbildung von Teststrukturen ist die Funktionstüchtigkeit von 16x3 Kanälen mit einem horizontalen Gesichtsfeld von 63° und einem Auflösungsvermögen der zentralen Kanäle von 3.3LP/° nachgewiesen worden. Die Übereinstimung der Zwischenbildebene und der Ebene der Feldblenden erscheint im Experiment besonders wichtig, da die Teleskope sonst in axial unterschiedlichen Bereichen das Gebiet der höchsten Bildschärfe und das Gebiet des besten Bildanschlusses aufweisen. Es gibt im Nachhinein keine Kompensationsmöglichkeiten, ohne entweder die Bildschärfe zu verringern oder den Bildanschluß zu verschlechtern. Trotzdem konnte mit diesem System erstmals experimentell die Erzeugung eines regulären Bildes mittels Übertragung unterschiedlicher Bildsegmente durch getrennte Kanäle mit starker Verkleinerung nachgewiesen werden. Dadurch hat dieser Ansatz das Potenzial, ähnliche Auflösungen zu ermöglichen, wie klassische Ein-Kanal-Objektive.

Die Menge der übertragbaren Informationen mit dem Cluster Auge ist deutlich höher als experimentell für das Appositionauge demonstriert. Dies folgt aus dem gleichzeitig höheren Gesichtsfeld und der besseren Winkelauflösung des Cluster Auges. Dafür ist andererseits das Clusterauge deutlich komplexer in der Herstellung und ebenfalls eine Größenordnung dicker als das Appositionsauge.

Die Abbildung durch Linsenarrays hat hinsichtlich des Orts-Bandbreite-Produktes, also bezüglich der Kapazität an Bildinformationen, gegenüber der Abbildung durch eine einzelne

miniaturisierte Linse nur dann wesentliche Vorteile, wenn jeder Kanal des Arrays einen anderen Teil der Bildinformation überträgt. Bei dem realisierten Appositionsauge mit gleichartigen Linsen ist das nicht der Fall. Durch das Vorschalten der Fresnellinse konnte das Auflösungsvermögen auch nicht verbessert werden. Hier wurden gleichzeitig zur Erweiterung des Gesichtfeldes, durch die Krümmung der Fresnelzonen und den Überlapp der Gräben mit den kartesisch angeordneten Kanälen, auch die Akzeptanzwinkel der einzelnen Kanäle vergrössert. Eine zusätzliche reine Prismenfunktion auf jedem Kanal würde das gewünschte Resultat der Auflösungserhöhung zur Folge haben. Diese Funktion kann auch direkt in die Linsenform integriert werden. Bei dem realisierten Ansatz des Cluster Auges ist aufgrund der geneigten optischen Achsen der Teleskope und daraus resultierenden unterschiedlichen Blickrichtungen der Informationsgehalt des gesamten Arrays deutlich grösser, als der des einzelnen Kanals.

In dieser Arbeit konnte gezeigt werden, dass die Methoden der Mikrooptik eine präzise Realisierung von potenziell kostengünstigen und extrem flachbauenden abbildenden Optiken, basierend auf künstlichen Facettenaugen, erlauben. Die experimentell realisierten Auflösungsvermögen von 1.5LP/° für das Appositionsauge, bzw. 3.3LP/° für das Cluster Auge erscheinen als sehr vielversprechend, verglichen mit heutigen konventionellen Optiken (Bsp.: Weitwinkelobjektiv mit 70° Gesichtsfeld mit "1 Megapixel" Sensor, Annahme der homogenen Auflösung über das Gesichtsfeld: 7.1LP/° Auflösungsvermögen) wenn man die Unterschiede in der Baulänge von ca. einer Grössenordnung berücksichtigt. Diese Auflösungen sind weiterhin mit denen der Wirbellosen wie Bienen oder Spinnen vergleichbar. Das Vorbild Natur lehrt, dass nicht die höchste Auflösung, sondern das best angepasste System das Überleben des Lebewesens bzw. den Erfolg der Optik ausmacht. Die bisher ungeahnten Einsatzmöglichkeiten der hier präsentierten Objektive sprechen für sich.

Damit wurden in dieser Arbeit die Fundamente für die zukünftige Forschung an flachbauenden und sehr flexibel einsetzbaren bildgebenden optischen Sensoren gelegt. Deren Entwicklung bis zur Produktreife steht noch aus. Weiterführende, resultierende Aufgabengebiete sind beispielsweise die Überwindung der Limitierung auf planare Technologien. Hierbei könnte z.B. die Lithographie auf gekrümmten Oberflächen mittels Laserschreiber eine große Rolle spielen.

Ehrenwörtliche Erklärung

Ich erkläre hiermit ehrenwörtlich, dass ich die vorliegende Arbeit selbständig, ohne unzulässige Hilfe Dritter und ohne Benutzung anderer als der angegebenen Hilfsmittel und Literatur angefertigt habe. Die aus anderen Quellen direkt oder indirekt übernommenen Daten und Konzepte sind unter Angabe der Quelle gekennzeichnet.

Bei der Auswahl und Auswertung folgenden Materials haben mir die nachstehend aufgeführten Personen in der jeweils beschriebenen Weise entgeltlich/unentgeltlich geholfen: Erzeugung mikrooptischer Strukturen nach von mir vorgegebenen Parametern – Dr. P. Dannberg, A. Matthes und Techniker, Fraunhofer Institut Angewandte Optik und Feinmechanik, Jena; Dr. E. B. Kley und Techniker, Institut für Angewandte Physik, Jena; Dr. T. Scharf und Techniker, Institut für Mikrotechnologie, Neuchâtel, Schweiz; Dr. M. Eisner, SUSS MicroOptics SA, Neuchâtel, Schweiz.

Weitere Personen waren an der inhaltlich-materiellen Erstellung der vorliegenden Arbeit nicht beteiligt. Insbesondere habe ich hierfür nicht die entgeltliche Hilfe von Vermittlungs- bzw. Beratungsdiensten (Promotionsberater oder andere Personen) in Anspruch genommen. Niemand hat von mir unmittelbar oder mittelbar geldwerte Leistungen für die Arbeiten erhalten, die im Zusammenhang mit dem Inhalt der vorgelegten Dissertation stehen.

Die Arbeit wurde bisher weder im In- noch im Ausland in gleicher oder ähnlicher Form einer anderen Prüfungsbehörde vorgelegt.

Die geltende Promotionsordnung der Physikalisch-Astronomischen Fakultät ist mir bekannt.

Ich versichere ehrenwörtlich, dass ich nach bestem Wissen die reine Wahrheit gesagt und nichts verschwiegen habe.

Jena, den 26. Juli 2005

Jacques Duparré

Lebenslauf

Persönliche Daten

Name:	Jacques W. Duparré
Geburtsdatum:	23. März 1977
Geburtsort:	Zwickau

Ausbildung

1983 - 1992	Polytechnische Oberschule Jena
1992 - 1995	"Carl Zeiss"-Gymnasium, mathematisch-naturwissenschaftlicher Spezialschulteil, Jena; Abschluss: Abitur
1995 - 1996	Zivildienst bei der Pflegestation des Arbeiter-Samariter-Bundes Jena
1996 - 1998	Grundstudium Physik an der Universität Bayreuth
1998 - 2002	Studium der Physik an der Friedrich-Schiller-Universität, Jena Abschluss: Diplomphysiker Thema der Diplomarbeit: "Theoretische und experimentelle Untersuchungen zu Mikrolinsenarray-Teleskopanordnungen für variable Strahlablenkung" (durchgeführt bei *piezosystem jena* GmbH)
seit 2002	Wissenschaftlicher Mitarbeiter am Fraunhofer-Institut Angewandte Optik und Feinmechanik, Jena

Auszeichnung

2004	Thüringer Forschungspreis für angewandte Forschung

Jena, den 26. Juli 2005

Jacques Duparré